School of Science
Department of Physics and Astronomy
Master Degree in Physics

Characterisation of photomultiplier tubes for the PLUME detector of the LHCb experiment

Supervisor:
Prof. Angelo Carbone

Co-supervisor:
Dr. Fabio Ferrari

Submitted by:
Luca Toscano

Academic Year 2020/2021

*"The main stumbling block in the way of any progress
is and always has been unimpeachable tradition"*
— *C.S. Wu*

Abstract

The Probe for LUminosity MEasurement (PLUME) detector is a luminometer capable of measuring the luminosity and beam conditions of the Large Hadron Collider (LHC), at the interaction point of the LHCb. The core of the luminometer is an hodoscope composed by 48 HAMAMATSU R760 photomultiplier tubes (PMT).

In the first part of this document, the characterization of 29 PMTs of the PLUME detector is presented. It was performed together with the LHCb group of the INFN section of Bologna. For each PMT the gain, the transit time drift, the linearity and the dark current are measured and studied. All the PMTs didn't report any issue. The mean of the gain values at 1250 V is measured to be $(1.493 \pm 0.003) \times 10^7$. The variation of the transit time depending on the supply voltage is quantified by looking at the transit time drift, which does not exceed the 6 ns between 650 V and 1250 V, the maximum possible voltage range. The PMTs show a non-linearity behaviour of about $30 - 40\%$ in the working regime of 1.5×10^5 gain. The dark current is lower than 10 nA at the maximum allowed voltage value (1250 V). Thanks these information, the monitoring systemof PLUME will be able to correct variations in PMTs performances, during the data taking.

The second part of the work was done at the "Laboratoire de Physique des 2 Infinis Irène Joliot-Curie" (IJCLab) of Orsay. The PLUME modules were tested in a dark box of the laboratory with and without the passage of the light through the optic fiber of the monitoring system, and in the PLUME structure, after the installation.

Contents

List of Figures

List of Tables

Introduction

The Large Hadron Collider beauty (LHCb) experiment is one of eight particle physics detector experiments situated at the Large Hadron Collider (LHC) at CERN. The research field of the LHCb collaboration is the flavour particle physics and the violation of the CP symmetry in the interaction between hadrons. During the first two operation periods of the LHC, Run 1 and Run 2, the LHCb collaboration made a great contribution to the research in particle physics.

In 2022, after three years of shut down, the new operation period, Run 3, is going to start. The LHC beam, in Run 1 and Run 2, was composed of a maximum of 2556 proton bunches, each with a population of 1.12×10^{11} protons [1, 2]. Over the three years of Run 3, the new beam will be composed of 2746 bunches [3]. Such bunches will collided at four beam interaction points (IPs) every 25 ns.

The upgraded LHCb detector will experience, during Run 3, a five-fold increase of luminosity and number of visible interactions per bunch crossing. For particle colliders, the luminosity is a fundamental parameter to be monitored. Because of his design as a single arm forward spectrometer, the LHCb detector is not able to operate at the same luminosity as ATLAS and CMS. Indeed, high occupancy can degrade the tracking performance of forward detectors and for this reason the instantaneous luminosity is maintained stable with the luminosity levelling technique. Therefore, the measure of the instantaneous luminosity in real time is essential for the operation of the LHCb experiment. This is the purpose of the Probe for LUminosity MEasurement (PLUME), the new luminometer of the LHCb upgraded detector.

PLUME is built as an hodoscope of 48 photomultiplier tubes R760 from HAMAMATSU. In this thesis, the characteristics of all the photomultiplier tubes are studied in detail.

Chapter 1 describes in detail the new PLUME detector. The purpose, the operations and components are addressed in this chapter, with a particular interest for the elementary detection modules composing the hodoscope.

Chapter 2 is intended as an introduction to general photomultiplier tubes components and characteristics that will be presented in the following chapters.

In Chapter 3, the characterization of the 29 photomultipliers tubes performed at the INFN laboratory of Bologna is presented. For each characteristic analyzed, the procedure

and the final results are presented.

The Chapter 4 covers the work done for the installation and commissioning of the PLUME detector, Phase II, at IJCLab of Orsay. During this phase, a modification of the elementary detection modules of PLUME has been implemented.

Chapter 1

PLUME detector

The Probe for LUminosity MEasurement (PLUME) detector is presented in this Chapter. Firstly a brief overview and an explanation of the purpose of the new detector for the operation of LHCb, is done. Then all the components of PLUME are described in detail. Finally the luminosity measurements through the logZero method is explained.

1.1   Overwiev

The Probe for LUminosity MEasurement (PLUME) detector is the new luminometer of the LHCb experiment at CERN [4]. PLUME will play an important role in LHCb operation during Run 3. It will deliver measurements of online luminosity using the logZero method.

The detector is based on registering Cherenkov light produced in quartz material by particles coming from the collision region. The elementary detectors composing the two-layer hodoscope of PLUME are photomultiplier tubes with quartz entrance windows and an additional optically connected quartz tablets. The photomultiplier tubes have a small size (the diameter of the window of the photomultiplier is 10 mm) with a typical expected occupancy of around 1% and a negligible probability to receive a contribution from two particles within one bunch crossing sampling. Therefore a yes/no counting will provide a reliable input to the logZero method of luminosity determination.

Following the experience of ATLAS LUCID detector [5], an alternative charge integration measurement is also implemented. Two sets of elementary detectors form cross-like structures surrounding the beam pipe on the two planes of the hodoscope. The presented design is based on a number of studies, in particular on those outlined in Ref. [6]. PLUME will be positioned upstream from the collision region between the VELO and BCM detectors. The PLUME information will be available both online, for fast online luminosity determination, and offline together with the rest of the LHCb data. Both functions are realized by the same readout system, connected to the LHCb ECS and
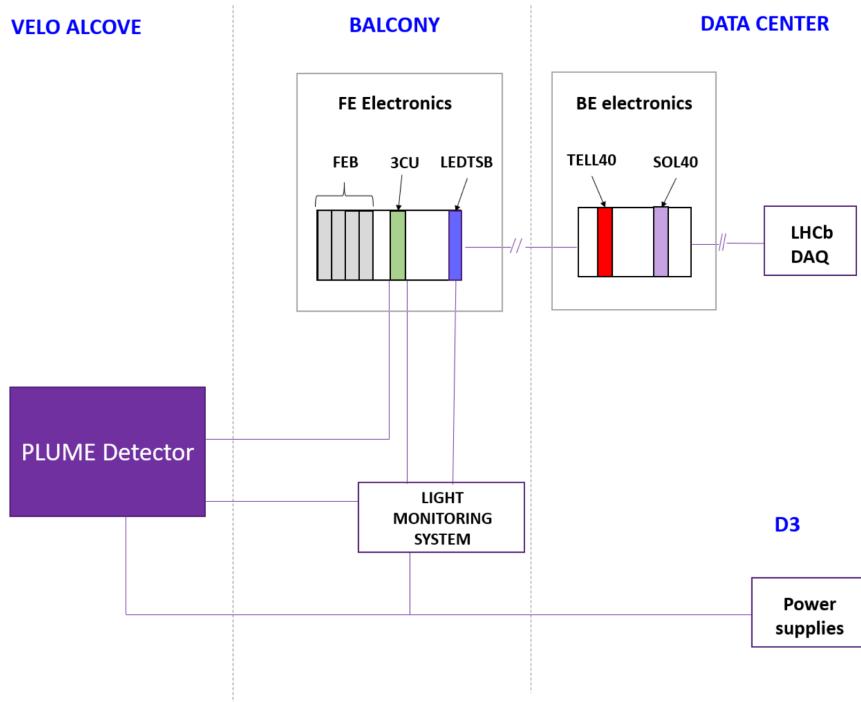
Figure 1.1: Schematic view of PLUME systems and their locations.

DAQ systems. The electronics chain is based on reusing the components developed for the LHCb calorimeters.

Calibration and monitoring of PLUME rely on LED light delivered to the front side of each elementary detector via long quartz fibers and on the tracks reconstructed in VELO stations and traversing PLUME elementary detectors. The gain of photomultipliers, which can drift due to temperature, occupancy, extracted charge, radiation conditions and other factors, and hit efficiency will be monitored. The approach to monitoring largely inherits from the experience of LHCb calorimeters and ATLAS LUCID. Using in addition tracks reconstructed in upstream VELO stations and passing through PLUME detector further improves the reliability of calibration and monitoring system. The schematic view of PLUME systems is illustrated in Fig. 1.1.

1.2   Purpose of PLUME

During the operation in Run 1 and 2, from 2010 to 2018, the LHC beam was composed of a maximum of 2556 proton bunches with a population of 1.12×10^{11} protons. Such bunches collided at four beam interaction points (IPs) every 50 ns in 2015, and every 25 ns until the end of Run 2. Starting in 2022, LHCb in Run 3 will see up to a 5-fold

increase ofthe number of visible interactions per bunch crossing, denoted μ.

As the production of heavy quarks takes predominantly place at low angle from the beam axis, LHCb has been designed as a single arm forward spectrometer. High occupancy can degrade the tracking performance of forward detectors like LHCb, which was designed to work at a lower luminosity with respect to the general purpose detectors ATLAS and CMS. Hence, the instantaneous luminosity at the LHCb interaction point is reduced by increasing the transversal distance between the two beams. While collisions decrease the beam intensity during an LHC fill, the transverse distance between the beams in LHCb is reduced, keeping the instantaneous luminosity stable within a $\pm 5\%$ range. This technique, named "luminosity levelling", minimises the effects of luminosity decay, allowing to maintain the same trigger configuration during a fill and to reduce systematic uncertainties due to changes in the detector occupancy [7, 8].

With the start of the Run 3, strong variations of luminosity, beam size, machine-induced background, ghost charge, satellites and beams crossing angle are expected. Measuring the instantaneous luminosity in real time is essential for the operation of the LHC machine, in particular to guide the levelling procedure at LHCb. A dedicated detector should also be able to provide a real-time feedback to the LHC. During the LHC Runs 1 and 2 online operation, the calorimeter activity was used to infer the average μ at the LHCb IP, using the information from the hardware-implemented L0 trigger, which will not exist anymore starting from Run 3.

Owing to the planned LHC luminosity increase, the LHCb detector is being upgraded to be able to cope with the new beam conditions [9]. The upgraded detector will start taking data in 2022 at luminosity values up to five times those experienced during Runs 1 and 2. The experiment will switch to a new triggering scheme based on Real Time Analysis (RTA), relying on the entirely software trigger with significantly more flexibility in terms of physics output. For such a scheme to work, it is mandatory to maintain stable running conditions of the experiment. One important parameter determining the running conditions is the instantaneous luminosity at the LHCb IP. In order to maintain the instantaneous luminosity averaged over beam crossings constant over an LHC fill and to measure the instantaneous luminosity for individual bunch crossings, a new dedicated detector has to be built. This will allow operating the LHCb detector in stable conditions while measuring the luminosity in real-time. It has been estimated that for the online operation the resolution of about 5% is required on the particle multiplicity. During Run 3, the monitoring of the radiation level and of the beam induced backgrounds will become even more crucial for maintaining reliable data quality and for extending the detector lifetime. Understanding of the background structure, the online monitoring and feeding back this information to the LHC are, therefore, essential features of the proposed new detector. Beam-induced background conditions should receive more careful monitoring at higher luminosity, with the goal of monitoring precisely the occurrence of bad quality vacuum and of undefined falling objects (UFOs) inside the beam pipe. Unstable machine conditions as well as issues during beam injection, should trigger real-time response from
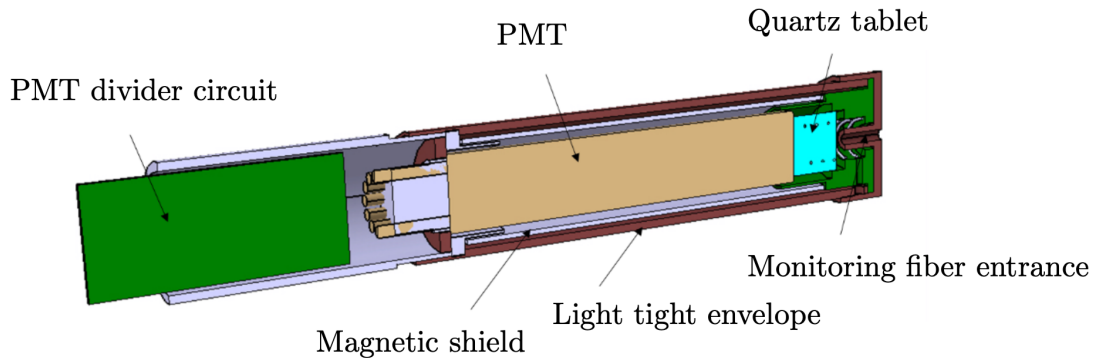
Figure 1.2: Schematic view of the PLUME elementary detection module. The module is 153 mm long with a diameter of 24 mm.

both LHCb and the LHC itself. The new detector should fulfill the following tasks

- deliver the online luminosity and μ measurements for the luminosity levelling;

- perform these measurements per bunch;

- measure the radiation background induced by the accelerator or bad vacuum, produce alarms, measure the level of the ghost charges;

- cross-check the LHC filling scheme in real time;

- contribute to the centrality determination in the fixed-target program;

- provide accurate offline luminosity determination.

The purpose of the new dedicated luminosity meter (luminometer) PLUME is to satisfy all the above requirements. It will be based on photomultipliers placed around the beam pipe and detecting Cherenkov light emitted by particles traversing fused silica radiators (quartz radiators). The Cherenkov light technology allows the signal to be produced and collected within a short time (~ 10 ps).

1.3 Elementary detection module

The hodoscope of PLUME is composed by 48 elementary detection modules. The layout of one module is illustrated in Fig. 1.2. The PMT and the divider circuit are fitted inside an aluminium cylindrical shield that protrudes 20 mm beyond the window in order to also host the quartz tablet. The structure allows the well centering of the quartz tablet respect to the PMT window as well as leaves the entrance space for the quartz fibre that brings the light to the front surface of the quartz tablet for the monitoring purposes. In
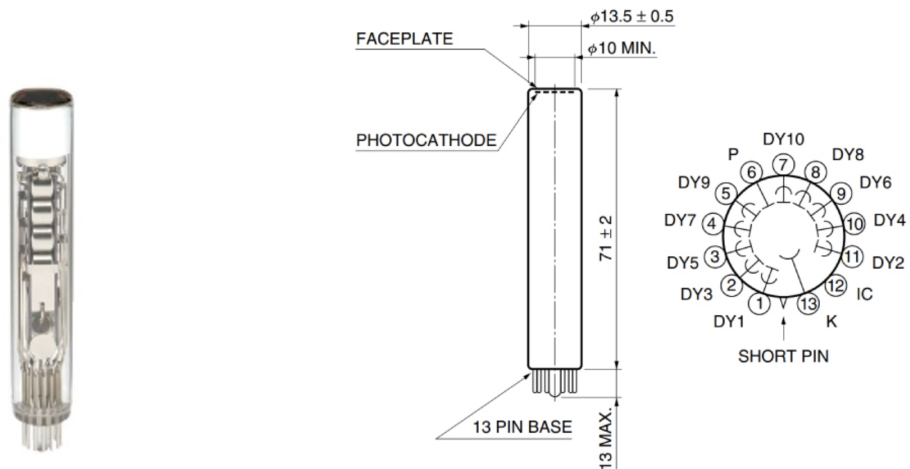
(a) *Picture of HAMAMATSU PMT R760.*   (b) *Scheme of HAMAMATSU PMT R760.*

Figure 1.3: Picture of HAMAMATSU PMT R760 model (a) and dimensional scheme of the HAMAMATSU PMT R760 (b).

order to eliminate a potential effect from the remaining magnetic field at the PLUME position, a magnetic shield screen surrounds the whole PMT. The screen extends the PMT by about 10 mm.

In total, the elementary detection module is 153 mm long with a diameter of 24 mm. In order to lighten the structure, polyetheretherketone (PEEK) material will be used to encapsulate the module components. This material is a semi-crystalline thermoplastic, which is resistant to radiation.

1.3.1   The R760 photomultipliers

The choice of detector is crucial for the correct operation of the detector. A set of technological requirements and exploitation considerations must be taken into account. First of all a fast signal is required to be well within the minimum distance of 25 ns between two sequential beam crossings in order to avoid spillover and to ensure an efficient readout. The amount of signal from a traversing particle should be significant, so that a potential threshold drift does affect the precision of the luminosity measurement, and well above the instrumental noise. The use of radiation-resistant materials is imposed by the harsh environment. A target occupancy per detector element of about 1% or more provides sufficient amount of data for accurate luminosity determination. Another constraint comes from the possibility to calibrate the detector using the tracks reconstructed in the VELO upstream stations. According to the VELO geometry and to the simulation, the preferred position of the elementary detectors is close to the beam pipe. The elementary detectors will detect particles coming from the interaction point at angles

ranging approximately between 5° and 10° with respect to the beam axis. Therefore, radiation resistance is a crucial requirement as the dose values in the considered area range between 80 and kGy and the neutron fluence is around 1×10^{14} neutrons/cm². The PLUME elementary detector is based on a photon detector registering the Cherenkov light emitted by particles traversing the quartz radiator. As the number of produced Cherenkov photons is limited, the use of SiPMs is disfavoured. Their performance for low light level detection under high radiation would be significantly altered or would require an expensive radiation-resistant cooling system in order to ensure their operation at temperatures down to $-40°C$. Therefore, in the light of all the above consideration, classical PMTs made with radiation hard materials like metal and quartz have been chosen for PLUME.

The selected photomultiplier tube model for PLUME is the R760 PMT produced by HAMAMATSU [11], Fig. 1.3a. R760 is a Head-on type photomultiplier tube with linear-focused dynodes structure composed by 10 steps.

The quartz window of this PMT is flat, has a thickness of 1.2 mm and a photocathode with a diameter of 10 mm. The responding wavelength range is between between 160 nm and 650 nm. Its quantum efficiency reaches its maximum for incoming light wavelength around 400 nm and exceeds 15% for wavelengths between 200 nm (about 6.7 photons produced per 10 nm spectrum bin in 1 mm thick pure fused silica) and 500 nm (about 1 photon per 10 nm bin per 1 mm thickness). The dimension of the PMT are illustrated in Fig. 1.3b.

The R760 had been tested under irradiation [12] with gamma rays up to 2×10^5 Gy dose and neutrons up to 2.7×10^{14} neutrons/cm² fluence and showed no variation of its spectral response and gain. The only observed effect to be taken into account is an increase of about one order of magnitude of the PMT dark current.

In order to determine the working point of the R760 PMTs, the characterization of all the photomultipliers tube used in PLUME will be performed and described in the Chapter 3.

1.3.2   Divider circuit

A standard resistive voltage divider is provided by HAMAMATSU. However, when the R760 PMT operated with this divider, a limited linearity for short pulses is observed. Because of this limitation, if the standard divider is used, all the gain measurements have to be performed with an incident light flux corresponding to an output charge smaller than 5 pC. The problem was overcome by developing an enhanced resistive voltage divider which delivers a maximum current of 1 mA for a bias voltage of 1000 V. The schematic view of the custom divider, built at IJCLab is shown in Fig. 1.4.

The circuit is in anode grounding, and the resistor between all the dynodes steps have the same values in order to obtain the same voltage differance. This divider stabilized the gain of the PMT up to an average anode current of about 100 μA compared to the

Photomultiplier base for R760 HAMAMATSU
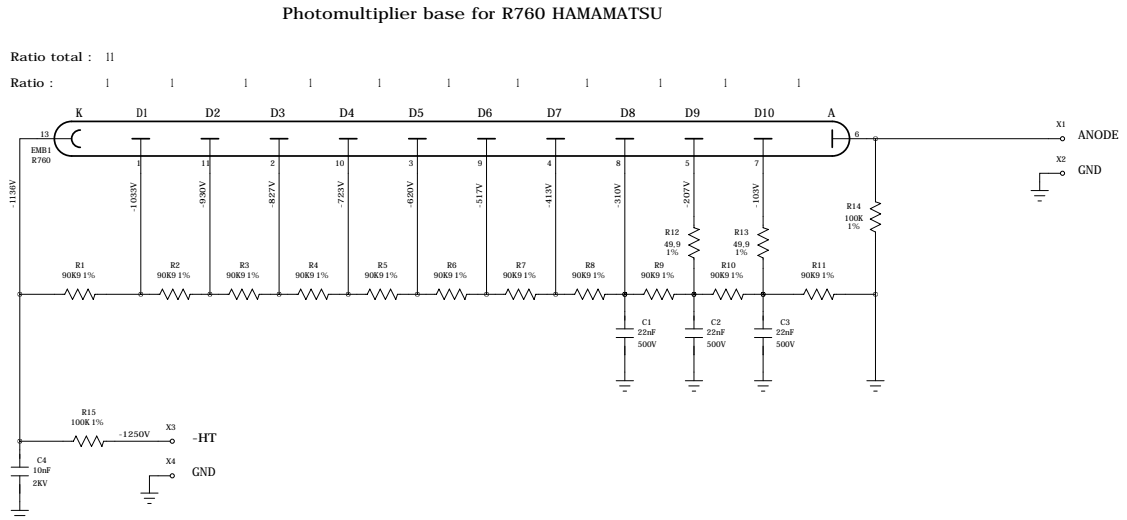
Figure 1.4: Scheme of the divider circuit built at IJCLab for the R760 HAMAMATSU PMT.

standard HAMAMATSU divider that can deliver an average current up to about 10μA before non-linearity appears. According to HAMAMATSU, the pulse current should not exceed 5 mA to guarantee a linearity better than a few percent. Taking into account this requirement, the pulsed linearity we measured that limits the output charge to 5 pC and the ageing effect for input signal corresponding to about 120 photoelectrons at the photocathode output, the gain of the PMTs should be set to 10^5, which corresponds to an average high voltage of approximately 700 V. The exact value of the linearity, the dark curent and the operating voltage are presented in Chapter 3.

1.3.3 Quartz radiator

The quartz radiator is fixed in front of the PMT window in order to increase the amount of produced Cherenkov light from the traversing particle. A 5 mm thick quartz tablet is positioned in front of the 1.2 mm thick quartz PMT window. The gain in light yield due to the addition of the tablet was simulated with Geant4 by [13]. The simulation was performed assuming an ideal optical coupling between the quartz window and the quartz tablet and so a transmission factor of 100%. According to simulation, Fig. 1.5, the addition of the quartz tablet increases the light yield about a factor 5.

The quartz type for the radiator is chosed in order to have a good transmittance for the Cherenkov light spectrum range and to be resistant enough to stand the expected level of radiation in PLUME. The two candidates were the Corning HPFS 7980 and the
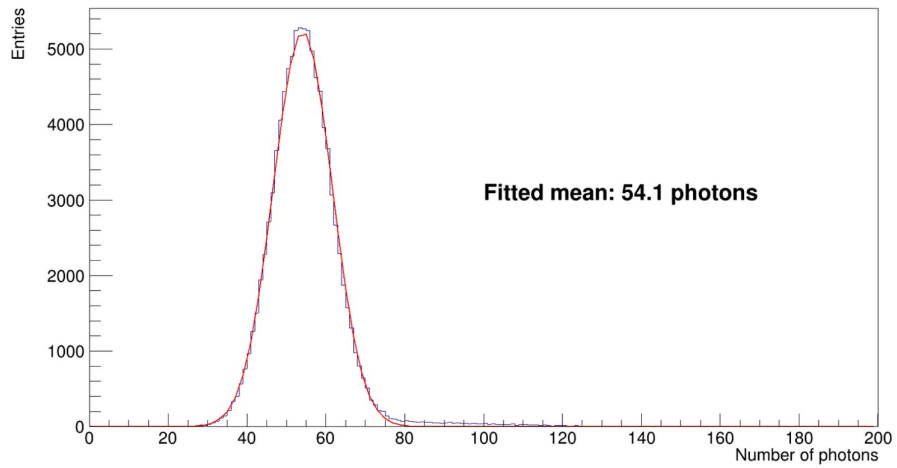
(a) *Photons emitted inside the PMT window.*
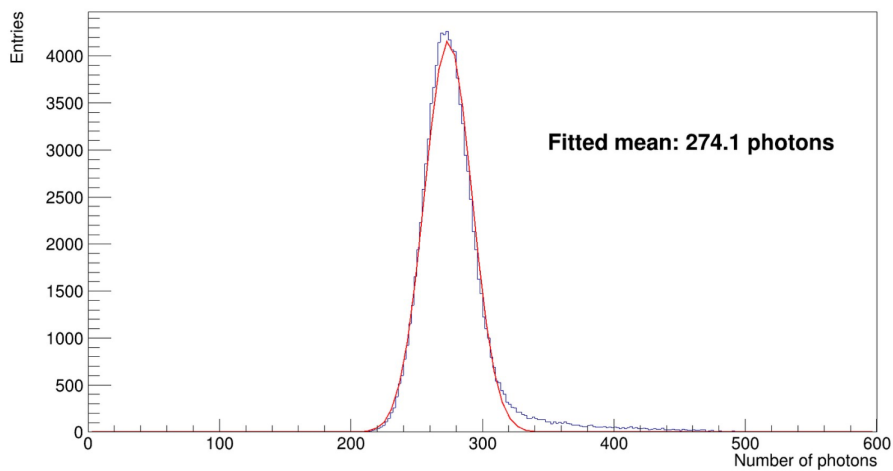
(b) *Photons emitted inside the quartz tablet.*

Figure 1.5: Geant4 simulation of the distributions of the expected number of photons produced inside the PMT window (a) and inside the quartz tablet coupled to the PMT window (b). The distributions are fitted with a Gaussian function.

10
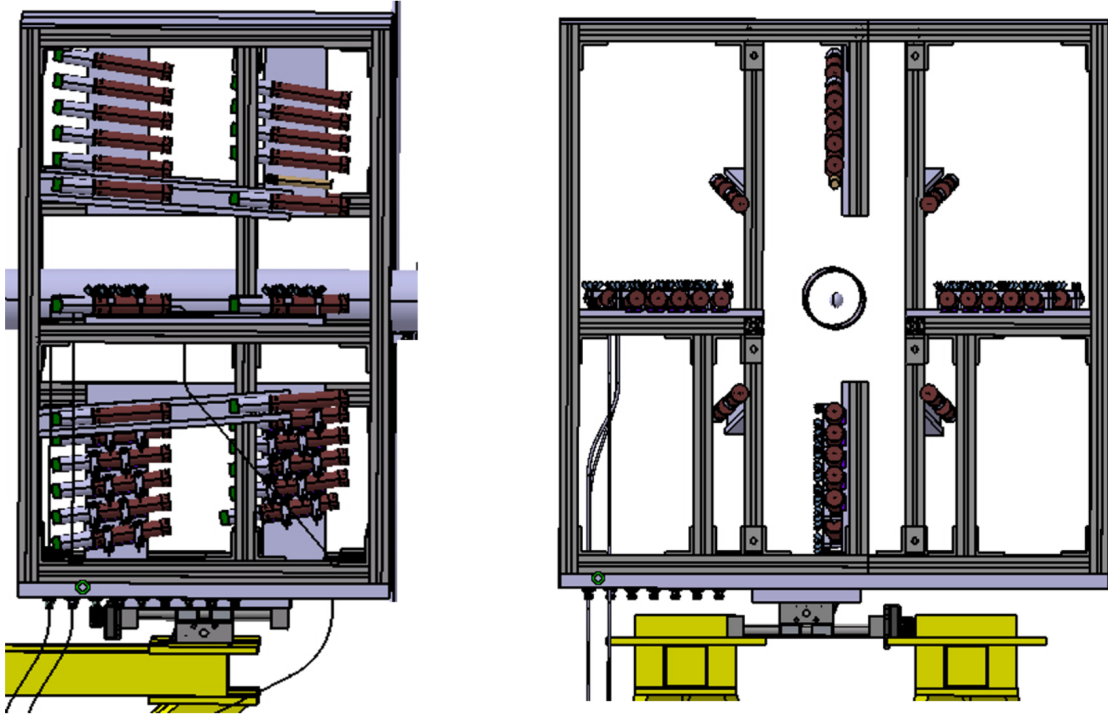
Figure 1.6: PLUME detector arrangement view in the *y-z* plan (left) and *x-y* plan (right)of the beam. Cable and fiber routing for one elementary detector module is shown.

SPECTROSIL 2000.

For transmittance, the results of a test performed at DESY [4] with 5.4 GeV electrons, were used. At DESY, the best amount of photoelectrons per incident particle was obtained with polished quartz tablet.

The radiant resistance was tested at NSC KIPT in February 2021. In order to study the transmission loss caused by neutrons, an irradiation test with a fluence of 9×10^{14} neutrons/cm^2 was performed. As the Cherenkov radiation is more intense in the short wavelengths range (below 350 nm) and the fused silica transparency in UV suffers from radiation, the effect on radiator and grease transparency was studied at these wavelengths. After irradiation, a transmittance of 42% at 200 nm, 37% at 250 nm and 88% at 300 nm was measured. After the tests, the best type of quartz turned out to be SPECTROSIL 2000.

The grease used for fixing the quartz radiator with the PMT window is Seiko-Silicone Grease TSF451-50M [14].

A dark absorbing ring is placed on the surface of the quartz radiator opposite to the PMT window in order to reduce the secondaries events in the hodoscope. In section 4.1, the study and the realization of the absorbing ring is described in detail.
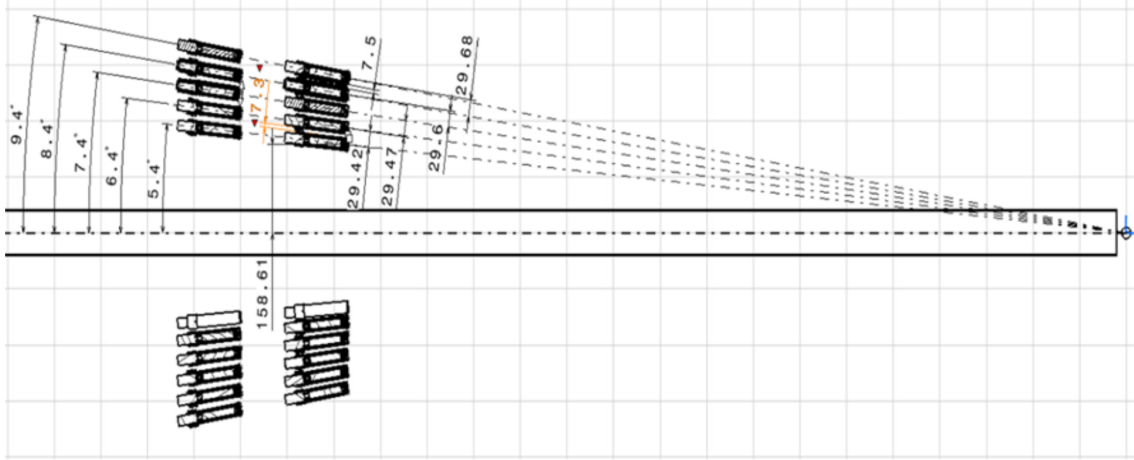
Figure 1.7: Angular positions of PLUME elementary detectors in the plan y-z with respect to the nominal primary pp collision vertex.

1.4 PLUME detector layout

The PLUME detector is composed by 48 elementary detection modules, described in the previous section. The 48 modules are arranged projective geometry and form a two-layer hodoscope with a cross shape around the beam tube. The detector arrangement in the mechanical supporting aluminium structure is illustrated in Fig. 1.6. The detector box is divided into A and C side parts and is mechanically protected from outside by a grid, which is common to VELO, SMOG2 and PLUME detectors. The geometrical envelope of the PLUME detector ranges between $z = -1485$ mm and $z = -2085$ mm along the beam axis. The inners elementary detection modules of the cross are placed at an angle of 5° respect to the beam axis, while the outers modules are placed at an angle of 10°, Fig. 1.7. This layout cover a pseudorapidity range of $2.4 < \eta < 3.1$. More technical detail in Ref. [15].

The two layers of the hodoscope are necessary for detecting the coincidence signal. The first layer of PMT is positioned at 1680 mm from the nominal interaction point, the second at 1900 mm. The two layers of the hodoscope are necessary for clean the sample of primary tracks. Only particles coming from the interaction point have the right direction to emit signal in two elementary elementary detectors and produces the signal in coincidence. An even cleaner sample can be obtained using track segments reconstructed in the VELO upstream stations and passing through the hodoscope acceptance.

The accuracy of the alignment in X and Y will be less than 1 mm. The alignment in Z is less constraining due to the significant extension of luminous region along the beam direction.

1.5 Electronics and readout

It is important to have PLUME information both online, for fast online luminosity determination, and offline to be available with the rest of the LHCb data. The same readout system is used for both these functions. It is connected to the LHCb Experiment Control (ECS) and Data Acquisition (DAQ) systems. The electronics chain largely reuses the components developed for the LHCb calorimeters and it's composed by a front-end (FE) part located close to the detector in the LHCb cavern and a back-end (BE) part. The PLUME readout elements are included in a dedicated partition inside the LHCb readout framework for ECS and DAQ.

One particularity of the PLUME readout is that it should be running even if the other detectors in LHCb are not running. This because during the adjustment phase of the LHC cycle, the value of the instantaneous luminosity at the LHCb IP is necessary for the LHC operator to prepare and optimize LHCb collisions.

1.5.1 Front-end electronics

The front-end has the scope to digitalize the signal coming from the detector and send it to the back-end system. Its components consist of 4 front-end boards (FEB) and 1 control unit board (3CU) installed in a crate in the balcony

- the role of the 4 front-end boards is to amplify, shape and integrate the signal from the detector PMTs, using a custom chip, ICECAL. The digitization of the signal is done by an ADC chip. The digital output is then processed in FPGAs. After formatting, the data are sent to the back-end electronics via optical fibers. For the PLUME front-end board, that one of the calorimeter is reused, only with firmware modification [16];

- the control board (3CU) [17] transmits the clock, commands and configuration from the global LHCb systems to the front-end boards inside the same crate. For the PLUME setup, one 3CU board is needed. The same board as built for the calorimeter is used.

Electronics boards are also used for the PLUME calibration system and will be hosted in the same crate as the front-end electronics.

1.5.2 Back-end electronics

The back-end electronics is implemented in the common LHCb readout board for the LHCb upgrade, the PCIe40 board GAs. The board TELL40 is dedicated to data processing. One TELL40 board is enough to process the data from the PLUME front-end electronics. Two main functions are realized by the TELL40 board: the computation of

the online instantaneous luminosity and the formatting of the data sent to the high level trigger and to offline storage. These two functionalities are implemented in the firmware of the TELL40 board, inside the framework available within LHCb.

One other PCIe40 board, dedicated to handling configuration, timing and control commands (called SOL40 board) is also required for the functioning of the system, with no specific modification needed for PLUME.

Online luminosity

The basic principle of the online luminosity determination is to count the number of bunch crossings without any visible interaction in the PLUME detector. The value of the luminosity is directly linked to the fraction of this number compared to the total number of bunch crossings. This is the basis of the logZero method (see Section 1.7.1).

In order to reduce the effect of the noise, it is advantageous to combine the measurements from the two hodoscopes and to require time and space coincidence between the hits, as said in Section 1.4 The firmware in the TELL40 will consist in producing a histogram with the number of hits in coincidence observed in PLUME. The fraction of events with no hits over the total of events is a measurement of the instantaneous luminosity. Such histograms are also built as a function of the beam crossing identifier (BCId) [19] in order to determine the luminosity per bunch crossing.

Data formatting

The second function of the TELL40 board is to assemble the data received from the front-end electronics according to a well defined format. These formatted data will be sent to the high level trigger and be part of the global LHCb RAW event. Since the input data are almost identical, the formatting firmware of the PLUME TELL40 follows closely the calorimeter TELL40 firmware [20]. The only difference being that the calorimeter LLT information is replaced by the per-channel over-threshold information.

1.5.3   DAQ and ECS

Software tools are developed to completely integrate the PLUME data in the global LHCb DAQ and Real Time Analysis (RTA) frameworks. The main item is the PLUME RAW event decoder, which will read the data out of the PCIe40 and transform them into objects usable by the LHCb analysis software, either in the high level trigger computations or for offline analysis.

The PLUME detector is connected to the central ECS similarly to other LHCb detectors. The PLUME control system is implemented in the global ECS of the LHCb experiment and complies with its requirements, implementing the proper finite state

machine (FSM) elements and using the global ECS database to archive important quantities [21].

1.6 Calibration and monitoring

The performances of a photomultipliers change during time. In particular gain and hit efficiency for constant hit counting, which are fundamental quantity, can be greatly affected to the current or detection occupancy, temperature and radiation dose. These two quantity of each PMTs inside the hodoscope of PLUME required a continuous monitoring. Therefore, the calibration and monitoring system is a crucial component for the well operation of the PLUME detector.

The monitoring system comprises two independent solutions: a LED calibration system and a calibration algorithm using upstream VELO tracks, like tracks travelling away from the LHCb spectrometer. By using these two approaches, the monitoring system has the possibility to continuously monitor PMT stability, and to provide the precise calibration of the PLUME for the luminosity determination.

Both the solutions implemented and tested in LUCID [5] and in the monitoring system of the LHCb calorimeters [22] are used for the design of the monitoring system of PLUME.

1.6.1 LED calibration system operation

The PMT response to the LED light pulses delivered to the PLUME PMTs through the quartz fibres is monitored at regular time intervals using suitable gaps in the LHC filling scheme. Even the stability of the light pulses must be checked in turn. In order to do that, a PIN photodiode is placed next to each LED at the balcony, where the radiation load is reduced. The quartz fibers transparency can be subject to degradation due to the radiation damage too. The transparency of the fibers is monitored with dedicated fibres looped back to the LED position and read out by the PMTs placed next to them.

The PMT response to the injected light changes depending on all the components described above. Based on the increase or decrease of the each PMT response, the supply voltage of the corresponding PMT is adjusted. The Power supply system allows steps of $\Delta V = 0.5$ V, which corresponds approximately to a 2% gain variation. The precise behaviours of the gain and the other characteristics of all the R760 PMTs depending on the voltage are studied in Section 3. The LED calibration system controls used for PLUME are the same as those for the LHCb calorimeter monitoring system, and therefore are fully compatible with the LHCb detector.
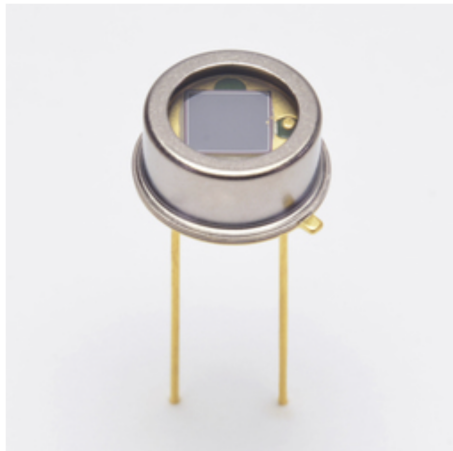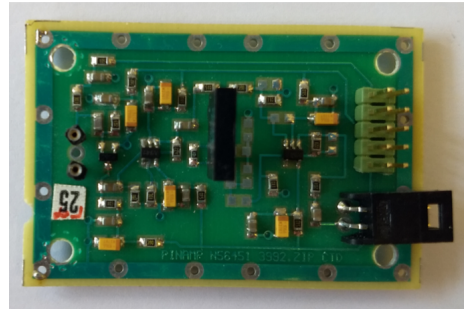
(a) *Photodiode Hamamatsu S1223-01.*   (b) *PIN amplifier.*

Figure 1.8: The photodiode Hamamatsu S1223-01 used to correct the LED instability of monitoring system (a) and its amplifier (b)

1.6.2   Components of the LED calibration system

Eight LEDs are flashed producing short pulses (< 15 ns FWHM) by eight driver boards. The LED driver uses the Cree LC503 (blue, wavelength 460 ± 25 nm). Its wavelength is chosen to match a transmission maximum typical for quartz fibres as they age under the influence of radiation. After the irradiation tests performed in the LUE40 accelerator [23], the fiber type chosen for the monitoring system is the $100\mu m$ core diameter quartz fiber FBP100 fibre from Polymicro. The LED signal illuminates a bundle of eight quartz fibres each. Then the fibres deliver the light to the PLUME PMTs.

In addition, one plastic fibre per LED sends the light to the corresponding PIN photodiode in order to correct the LED instability. PIN used is the photodiode Hamamatsu S1223-01 [24]. If the LED amplitude changes, this effect will be corrected according to the ratio between the PMT and the PIN photodiode readings. The LED light is delivered to the PIN diode through a clear plastic fibre Eska CK–40, a 1 mm diameter PMMA fibre produced by the Mitsubishi Chemical Corporation. The PIN diode and its amplifier are displaced and individually shielded, minimizing electromagnetic pickup of the LED driver board by the PIN amplifier. The PIN photodiode and the PIN amplifier circuit are shown in Fig. 1.8 The PIN photodiode signal is extracted through an amplifier board. Both signals are read out using the front-end boards, Section 1.5.

The full system comprises the following hardware components

- a LED timing unit, the LEDTSB [25]. This is a 9U electronic board installed at the readout crate;

16
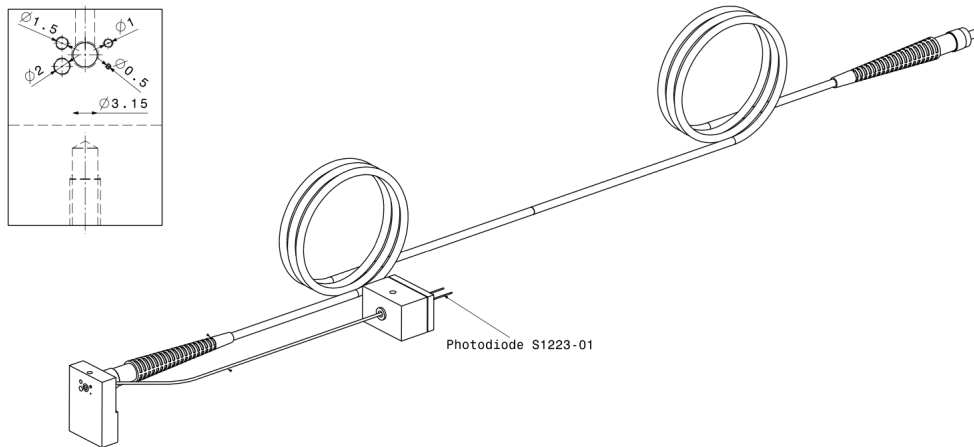
Figure 1.9: Scheme of the prototype for the elementary module of the monitoring system

- an E-Link Distribution Module (ELDM) [26];

- the "light box" containing the eight LEDs with their individual driver boards and eight PIN photodiodes with amplifiers. It takes LVDS trigger pulses, and provides light flashes to the PMTs and amplified PIN photodiode pulses to the readout crate;

- quartz fibre bundles delivering light to the PLUME PMTs;

- four R760 PMTs for monitoring quartz fibre transparency;

- a dedicated FEB for reading out the eight PIN diodes and four fibre radiation monitoring PMTs.

For most of these components, already existing calorimeter spares are used. The quartz fibre bundles will be produced, as well as the mechanics of the "light box". A modular design is developed to house an individual LED driver, PIN diode and amplifier, and their connections. This simplifies installation and eventual replacement of the components. The scheme of the prototype of an elementary module of the monitoring system is drawn in Fig. 1.9.

1.6.3 VELO calibration algorithm

The second solution of the monitoring system is the calibration algorithm using upstream VELO tracks. The PLUME geometry is also dictated to the request of the ability to calibrate PLUME response with VELO tracks. The rapidity coverage of PLUME is chosen to overlap with that of the upstream VELO stations in LHCb, so that upstream

17

VELO tracks are in the PLUME acceptance. Not all the events detected by the VELO can be used in the PLUME calibration system. The calibration sample events should satisfy the following criteria

- have an associated track reconstructed in 4-5 upstream VELO stations and pointing to a given PMT;

- have a coinciding signal in the matching PMT of the second hodoscope plane.

The coincidence between matching PMTs of the hodoscope substantially has the goal to suppresses secondaries. At $\mu = 8$ a coincidence between two PMTs is detected in 1.5% of the cases, with a primary to secondary particle ratio of $\approx 1 : 2$ to $1 : 1$ depending on the relative position of the two layers. An effective acceptance of VELO tracks that are useful for PLUME calibration is enlarged by reconstructing tracks both in the VELO closed and open position. In addition, a spread of the vertex positions across the collision region will produce tracks reliably reconstructed in VELO, which will cross PLUME hodoscope in a larger angular range. Corrections to account for the vertex position are discussed in Section 1.7.

1.6.4 Integration of the calibrations

The LED calibration continuously monitors the PMT responses to a fixed and known amount of light, as said in the section above. It will be accurate at least during short periods of the order of fills. By adjusting the high voltage and the timing, the response in the number of photons per track from IP of the gain and efficiency of the PMTs is kept approximately constant.

Because of possible slow ageing of the LED light transportation system or any other relevant deterioration, the LED calibration alone is not enough in the longer term. Then, the stability will be ensured using one-track peaks visible in the events with a VELO-reconstructed track passing through a PMT or in a standalone mode using the events with two projective PMTs in the hodoscope above threshold. According to the simulation, one-track peaks will also be visible in this case.

Such VELO calibration requires more time and data and can be performed only quasi-online or offline. Both LED and VELO based calibrations are be performed by automatic scripts running e.g. between fills. Sometimes the calibration can be performed twice (as is done in LUCID). The first one compensates the ageing while the second one (in ~ 0.5 hour) verifies that the HV adjustment returns the PMT right response for the specified constant number of photons per track from IP.

In addition, a cross-calibrations respect to other LHCb detectors that are able to measure luminosity is possible. In particular, with those detectors that are based on the number of tracks and vertices reconstructed by the VELO detector.

1.7 Luminosity measurements

In particle collider physic, the luminosity is the quantity which defines the ability of the collider to produce functional events. From a physical point of view, the instantaneous luminosity is defined as [27]

$$\mathcal{L} = \frac{R}{\sigma},\tag{1.1}$$

where R is the rate of a generic physical process while σ is the cross-section of this process. The unit of the luminosity is the $\mathrm{cm}^{-2}\mathrm{s}^{-1}$ or equivalently $b^{-1}\mathrm{s}^{-1}$. One micro-barn μb corresponds to $10^{30}\mathrm{cm}^2$. The instantaneous luminosity $\mathcal{L}$, measures the instantaneous number of interactions per second.

In particle physics can be useful also to know the number of interactions over a certain time. The relevant parameter describing the number of events collected over certain time interval of a machine is the so-called integrated luminosity, defined as the time integral of the instantaneous luminosity

$$\mathcal{L}_{int} = \int_0^T \mathcal{L}(t')dt'.\tag{1.2}$$

The integral is taken over the time the machine is filled or in other words excluding dead time. The integrated luminosity is measured in cm^{-2} or equivalently in inverse barns $b-1$.

Although linearity has a simple and intuitive definition, in the practice the measurement of the luminosity is quite more complex. In the next section the logZero method used by PLUME is explained.

1.7.1 Online luminosity measurements

In the Section 1.5.2 the functions of the board TELL40 are briefly explained. In particular, the main goal of the back-end electronic of PLUME is the measurement of the online liminosity. In order to perform a fast and accurate measurements, for every PMT and for every bunch-crossing the TELL40 accumulates a histogram with two bins. The bins of the histograms are filled respectively with the number of events below and above a defined threshold. The histograms are reset every ~ 3 seconds but even the bunch-crossings arriving during the reset are counted. A better accuracy is obtained by measuring the events leaving a signal in coincidences of projective PMTs. In this way the backgrounds is reduced while the contribution from the tracks originating from the interaction region is enhanced

Due to the PMT ageing and the background below one-track signal, a special care is required in setting the thresholds. It will be defined with respect to the signal from the IP tracks. Thanks to the monitoring and calibrating system, the threshold can be

kept constant by adjusting the PMT gain and timing, so setting the threshold to a constant value in the electronics will be sufficient. However, a programmable threshold method is preferred and so different threshold values can be implemented in the front-end electronics.

The actual measurement of the luminosity at LHC is done by counting the visible mean number of inelastic interactions per bunch-crossing μ The particular method to determine μ used at LHCb, even in Run 2, is the aforementioned logZero method. Assuming Poisson statistics, μ can be expressed as [28]

$$\mu = -\ln P_0 = -\ln \frac{N_0}{N} - \frac{1}{2}\left(\frac{1}{N_0} + \frac{1}{N}\right), \tag{1.3}$$

where N_0, N are the number of empty and all events, respectively, and P_0 is the fraction of empty events. The definition of the "empty" event depends on the luminometer and correspond to detected an event with a signal compatible with zero. For one PLUME PMT N_0 is the number of events with a signal below the threshold out of N in total. The second term in 1.3 comess from the non-linearity of the algorithm,

$$\mu = -\ln \frac{\langle n_0 \rangle}{N} \neq -\langle \ln \frac{n_0}{N} \rangle, \tag{1.4}$$

where n_0 is the number of empty events which follow a Binomial distribution, and $\langle n_0 \rangle = N_0$ is the average value of the distribution. The average bias is calculated as

$$\begin{aligned}
\mu - \langle -\ln \frac{n_0}{N} \rangle = \langle \ln \frac{n_0}{N} \rangle &= \langle \ln\left(1 + \frac{n_0 - N_0}{N}\right) \rangle \\
&\approx \langle \ln \frac{n_0 - N_0}{N_0} \rangle - \langle \ln \frac{(n_0 - N_0)^2}{2N_0^2} \rangle.
\end{aligned} \tag{1.5}$$

The mean of the Binomial distribution of n_0 is N_0, so the first term vanishes. The numerator of the second term is the variance of the Binomial distribution $NP_0(1-P_0) = N_0(1 - N_0/N)$, so the bias becomes

$$\mu - \langle -\ln \frac{n_0}{N} \rangle = -\frac{N_0(1 - N_0/N)}{2N_0^2} = \frac{1}{2}\left(\frac{1}{N_0} + \frac{1}{N}\right), \tag{1.6}$$

which is equal to the second term in 1.3.

From the value of μ it's then possible to compute the instantaneous luminosity $\mathcal{L}$, by the relation [27]

$$\mathcal{L} = \frac{\mu n_b f_r}{\sigma_{inel}} \tag{1.7}$$

In the Eq. 1.7, n_b is number of bunches, and f_r is the bunch revolution frequency. The σ_{intel} is the inelastic cross-section which can be measured as visible cross section by the Van der Meer Scan method [29].

The histograms and luminosity values per bunch will be archived by the LHCb control system and stored in the online configuration and condition database of the experiment. The advantage of the online measurement is that it is performed with the full available statistics. These histograms will also be used offline after applying efficiency and time drift corrections.

1.7.2 Offline luminosity measurements

The offline measurement will depend on the HLT and RTA capabilities. Minimally, the PLUME data will be stored in nano-events taken with random triggers. The analysis then proceeds in the same way as outlined above online analysis with, however, significantly reduced event samples. However, the offline analysis has several advantages.

First of all the offline measurements allows the analysis of coincidences not only between matching PLUME hodoscope channels but also with other luminometers.

Another advantage is that in addition to the logZero method described in Eq. 1.3, one can use the signal amplitudes and the average method. This is possible only with small occupancies, at the level of a few percent. At this condition the pile-up probability is small and the analog spectrum above pedestal of the PMTs is dominated by the one-interaction spectrum. The contribution of two interactions is suppressed as $\frac{\mu^2/2}{\mu}$ i.e. as "occupancy"/2. The one-track PMT signal can be kept approximately constant by adjusting the PMT gain and timing with the calibration system (Section 1.6). After that the reconstructed one-interaction spectrum should be constant. This will allow performing a powerful cross-check. Any deviation might reveal some hidden detector effects and systematic uncertainties. In general, measurements with any single PMT or any pair of projective PMTs are sufficient to measure the luminosity, if free from background and systematic effects. This gives a large redundancy and a possibility of numerous cross-checks.

Moreover, if the HLT allows to store not only per-event information, but also the histograms, the same two bin histogram used in the online measurement can be used. In addition to two-bin counters used for the logZero method, the analog spectra of the events can be analyzed too. In this case, the full PLUME information are exploited. This might be useful, in particular, for debugging the TELL40 firmware and the implementation of the online luminosity determination.

Chapter 2

Photomultiplier tubes

The most commonly used instrument for the detection of light signals is the photo-multiplier tube (PMT). The core of the PLUME detector, as said in Section 1.3, is an hodoscope formed by two-planes of R760 PMTs produced by HAMAMATSU. In this Chapter an overview of all the aspects of a photomultiplier tube is done. In the first part, a brief description of the the photoelectric effect, the physic process behind the operation of a PMT, is done. Then, the fundamental elements composing a PMT will be listed and their description will be given. Finally, the main operational characteristics of a PMT will be discussed.

2.1 Physics of a PMT

2.1.1 Photon interaction with matter

Photons are neutral massless particles so their behavior in matter is drastically different from that of charged particles. The lack of an electric charge makes impossible the inelastic collisions with the electric field of atomic electrons, that is the main interaction process of charged particles. The three main interaction of x-rays and γ-rays in matter are

- photoelectric effect;

- compton scattering (including Thomson and Rayleigh scattering);

- pair production.

A photon that interacts with matter by one of these processes is entirely removed, either by absorption or scattering from the incident beam, while a photon which doesn't suffer any interaction retains its original energy. Therefore a beam of photons crossing a material undergoes an attenuation in intensity, not a decrease in energy. The law

describing the attenuation suffered by a photon beam is exponential with the thickness of the absorbing medium and can be written as [30]

$$I(x) = I_0 e^{-x\mu_l}, \tag{2.1}$$

where I_0 is the intensity of the incident beam, x is the thickness of the medium and μ_l is its mass absorption coefficient. The mass absorption coefficient is a quantity characteristic of the absorbing material which is directly related to the total interaction cross-section of the photon per atom (σ) and the density of atoms (N),

$$\mu_l = N\sigma = \left(\frac{N_a \rho}{A}\right)\sigma, \tag{2.2}$$

where N_a is the Avogadro's Number, ρ is the density of the material, and A is the molecular weight. Due to the small cross section of all this kind of reactions, x-ray or γ-ray are many times more penetrating than charged particles. The contribution of each processes to the total cross section depends a lot on the energy of the initial photon. The plot of the mass absorption coefficient for iron, and so the cross section with respect to the energy is shown in Fig. 2.1 [31]. It's clear from the graph that the main contribution at energies below 10^{-1} MeV is due to the photoelectric effect, while for higher energies the predominant contributions come from the coherent and incoherent scattering, or Compton and Rayleigh, and then from the pair production. Photomultiplier detectors exploit the photoelectric effect, described in more detail in the next section.

2.1.2 Photoelectric effect

The photoelectric effect involves the absorption of an impinging photon by an atomic electron, with the subsequent ejection of the electron from the atom. The process is also referred as photoemission, and the ejected electron is called photoelectron. The first study on the photoemission of electrons was done by Heinrich Hertz in 1887. The initial approach to explain this new phenomenon was based on the assumption that light traveled purely as a wave through space, but this was at odds with the data. In order to explain the experimental data, Albert Einstein, in 1905, published a paper in which he advanced a hypothesis based on the quantum theory of Max Planck [32]. Einstein theorized that the light energy is carried in discrete quantized packets, the photons, equal to the frequency of light ν multiplied by a constant h, later called Planck's constant

$$E_\gamma = \nu h. \tag{2.3}$$

During the photoemission, the entire energy of a photon is absorbed by an electron bounded in an atomic shell. If the energy of the initial photon is sufficient to allow the
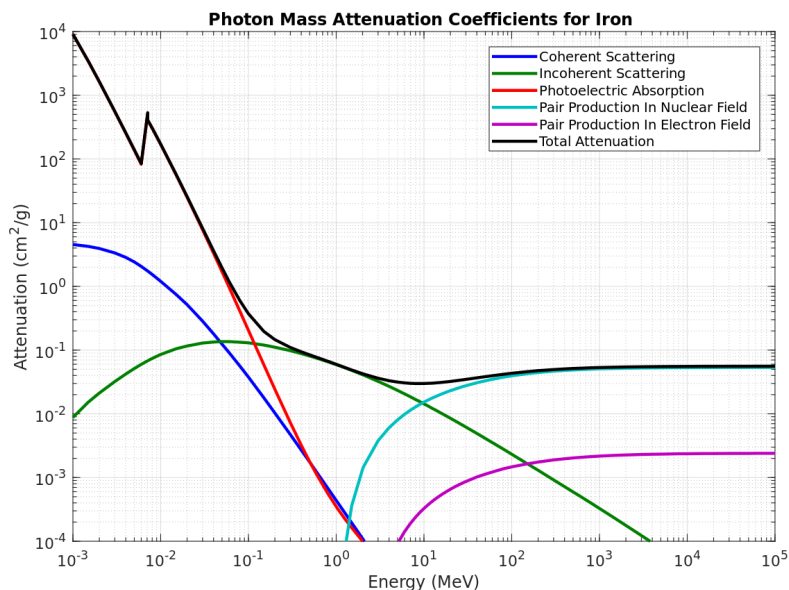
Figure 2.1: Mass attenuation coefficient of iron with contributing sources of attenuation: coherent scattering, incoherent scattering, photoelectric absorption, and two types of pair production. The discontinuity of photoelectric absorption values are due to K-edge.

electron to overcome his binding energy (BE) and to ionize, the maximum kinetic energy of the ejected electrons will be

$$K_{max} = E_\gamma - BE = \nu h - BE. \tag{2.4}$$

Therefore there is a minimum frequency, called threshold frequency, ν_0 under which there is no emission.

The Photoelectric effect, due to momentum conservation, always requires a third collision partner which in this case is the atomic nucleus. Therefore this kind of process only occurs on bound electrons with the nucleus absorbing the recoil momentum. The typical photoelectric atomic cross-section σ_{photo} will depend on the energy of the atomic shell. In Fig 2.2 the cross-section as a function of the incident photon energy, in the case of lead, is shown. As it can be seen, the photoelectric atomic cross-section is very low for energy above the highest electron binding energy of the atom, the K shell, but it increases rapidly as this energy is approached. When the photon energy is exactly equal to the one of the electron binding energy of the shells (K, L, M), the cross-section produces a peak and after this point, it drops drastically. These drops are called K, L and M absorption edge. Below each absorption edge the cross-section increases once again, creating a sawtooth shape.

Due to the complexity of the Dirac wavefunction for the atomic electrons, the photoelectric effect is difficult to treat rigorously. A possible way to compute the cross-section
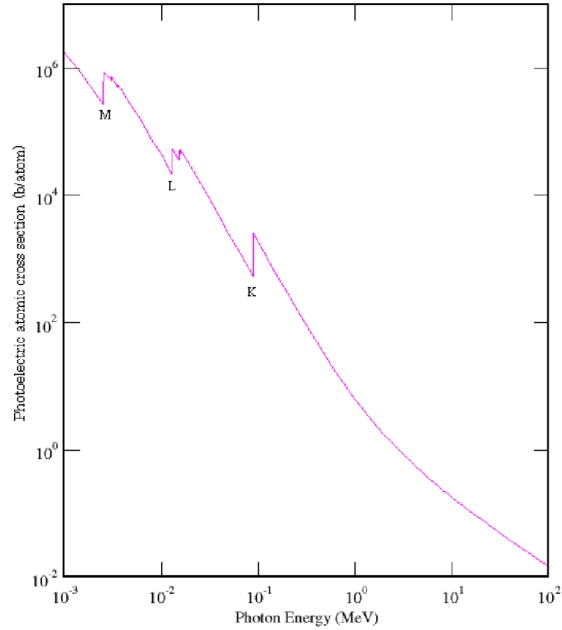
Figure 2.2: Photoelectric atomic cross section σ_{photo} of lead. The absorption edges of shells K, L and M can be observed. The K absorption edge is at 88 keV. Data from NIST [31]

is to consider only the situation in which photons have an energy above the K absorption edge. In this case the cross-section for absorption of a photon of energy E_γ in the K shell is approximately the 80% of the total cross-section, even because the third collision partner, the atomic nucleus, is closer to the process. Assuming the non-relativistic condition, $h\nu \ll m_e c^2$, for the energy of the photon and to be far from the K absorption edge, the cross-section can be calculated using the non-relativistic Born approximation [33] and becomes

$$\sigma_{photo}^K = \left(\frac{32}{\epsilon^7}\right)^{1/2} \alpha^4 \cdot Z^5 \cdot \sigma_{Th}^e \ \{\text{cm}^2/\text{atom}\}. \tag{2.5}$$

In the expression above $\epsilon = E_\gamma/m_e c^2 = h\nu/m_e c^2$ is the reduced photon energy, $\alpha = \frac{1}{4\pi\epsilon_0}\frac{e^2}{\hbar c} = \frac{1}{137}$ is the fine-structure constant, Z is the atomic number of the material and $\sigma_{Th}^e = \frac{8}{3}\pi r_e^2 = 6.65 \cdot 10^{-25} cm^2$ is the Thompson cross section for the elastic scattering of photons on electrons.

2.2   Structure of PMT

A photomultiplier tube is a vacuum tube consisting of an input window photocathode, focusing electrodes, an electron multiplier, or dynodes system, and an anode usually

25
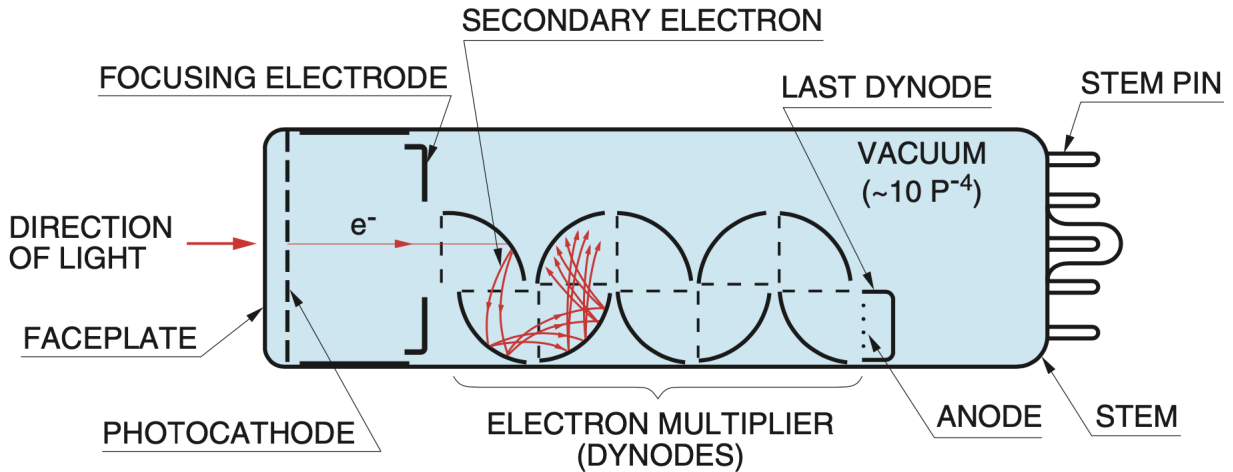
Figure 2.3: Scheme of the basic elements of a photomultiplier tube [34].

sealed into an evacuated glass tube.

The outer envelope (usually glass) serves as a pressure boundary to sustain vacuum conditions inside the tube that are required so that low-energy electrons can be accelerated efficiently by internal electric fields. The first component just after the window is the photocathode. Here, the impinging photons are converted into electrons by the photoelectric effect.

Since only a few hundred photoelectrons may be involved in a light pulse, their charge is too small at this point to serve as a convenient electrical signal. In order to overcome this problem, the output signal is amplified by the dynode system. The photoelectron generated in the photocathode goes through several steps of electrodes, called dynodes, which increase the number of electrons through secondary emissions. After amplification, the generated electrons produce sufficient charge signal to be detected. The charge is collected at the anode or output stage of the multiplier structure. The scheme of a typical photomultiplier tube is shown in Fig. 2.3. Depending on the structure of the dynode system, different types of PMT exist. The R760 PMT model from HAMAMATSU, used in PLUME, has a linear-focused dynodes system type.

The electrons are accelerated and focused by electric fields, generated by a potential difference between each dynode. The required potential gradients are usually obtained from a voltage divider powered by a high voltage supply.

2.2.1 Window

Most of the photocathodes have high sensitivity down to the ultraviolet region. This happens because the material of the input window limits the spectral sensitivity in the
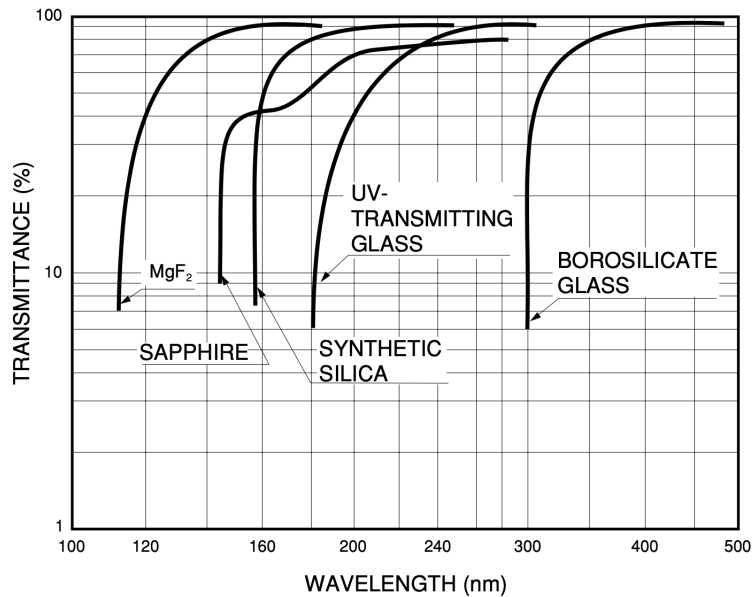
Figure 2.4: Transmission (%) as a function of wavelength λ for various glasses used in photomultiplier input windows [34].

short wavelength region. The transmittance of the light for different materials is shown in the graph of Fig. 2.4 [34]. For materials as borosilicate glass (hard glass) and lime glass (soft glass), the transmittance is cut-off between 250 and 300 nm. Even with LiF or MgF2, UV-radiation of less than 180 nm can be investigated only in vacuum because of the absorption of the air. For lower wavelengths, other devices as single-channel electron multipliers or microchannel plates may be used.

The window of the R760 PMTs is a head-on type (sensitive area is only the top of the device) with a fused silica window. It can detect light with wavelength above 160 nm.

2.2.2 Photocathode

The photons transmitted through the window, reach the photocathode, where they are converted into electrons. The incident photon transfers energy to an electron of the material, which starts to migrate until it escapes from the surface of the photocatode.

Since a photocathode is a semiconductor, it can be described by using band models, as shown in Fig. 2.5. In this model, before the conductive band, there exist a forbidden band gap, EG, that cannot be occupied by electrons. The interval of energy between the conduction band and the vacuum level barrier is called electron affinity (EA). As shown in the Fig 2.5, the electrons in the valence band absorbs the energy of the photon, given by Eq. 2.3. For blue light typical of that emitted by many scintillators, the quantum

27
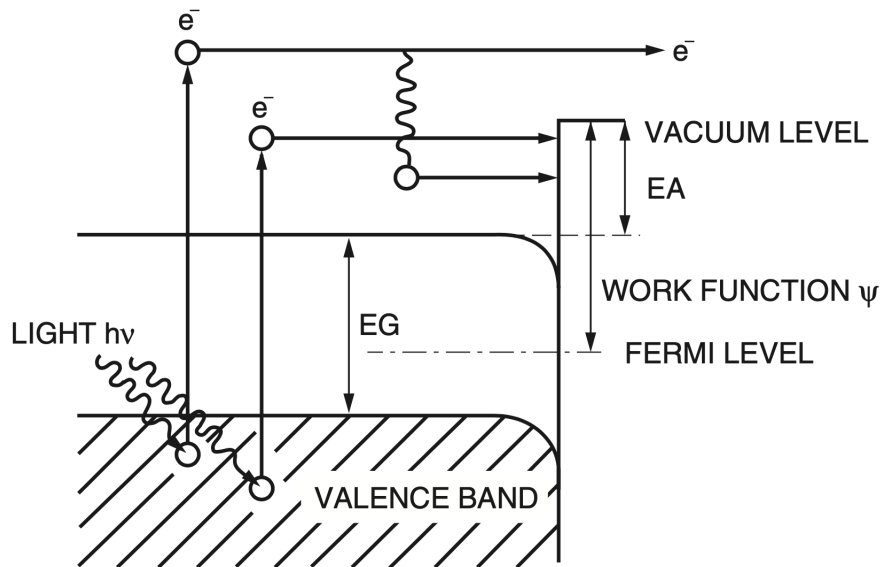
Figure 2.5: Photocathode band model [34]. EG is the energy gap between valence band and conductive band; EA is the electron affinity corresponds to interval of energy between the conduction band and the vacuum level; Ψ is the energy difference between Fermi level and the vacuum level, called work function.

energy is about 3 eV. If this energy is high enough, the diffused electrons acquires sufficient energy to overcome the vacuum level barrier (typicaly 1.5-2 eV for suitably prepared semiconductors) and they are emitted in the vacuum as photoelectrons. All photocathodes therefore have a long-wavelength (small ν) cut-off that is usually in the red or near-infrared portion of the spectrum.

The rate of energy loss as the electron migrates to the surface should be kept small in order to allowed as much electron as possible to be emitted. Semiconductors has a very low rate of energy loss so the escape depth can extend to about 25 nm. However, the thickness of the photocathode can not be too thin, otherwise it becomes semitransparent and less than half the visible light to interact within the photosensitive layer.

The R760 PMT has a bialkali photocathode, which is sensitive in the ultraviolet to visible light range. Bialkali photocathodes have higer sensitivity and lower dark current (see Section 2.3.5) than alkali ones.

The conversion efficiency of the photocathode and the wavelength response range are described by the quantity called quantum efficiency (QE), described later.

28
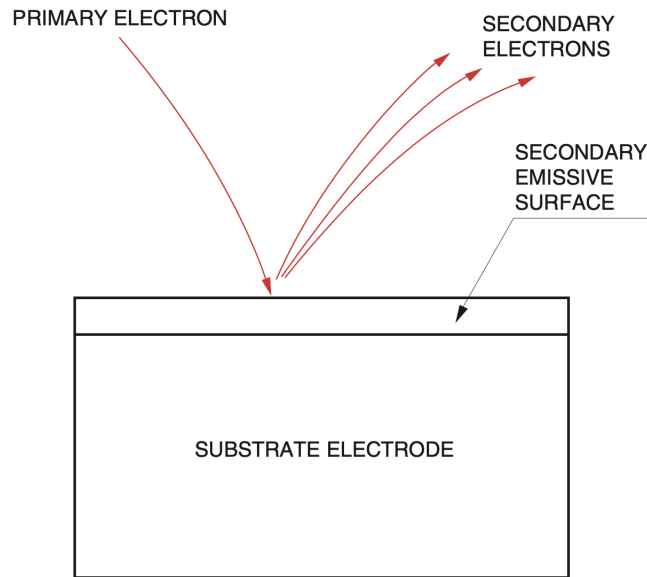
Figure 2.6: Secondary emission model of electron multiplication on the dynode surface [34].

2.2.3 Electron multipliers (dynodes)

The multiplier portion of a PM tube is based on the phenomenon of secondary electron emission . Electrons from the photocathode are accelerated and sent to the electrodes, called a dynodes. The surface of each dynodes is covered with a thin layer of secondary emissive material. The most common materials are alkali antimonide (Sb), beryllium oxide (BeO) and magnesium oxide (MgO). These material are coated onto a substrate electrode made of nikel, stainless steel or copper-beryllium alloy.

The primary electrons deposits energy in the in the dynode material, producing the re-emission of secondary electrons by excitation. Fig 2.6 shows a model of the secondary emission multiplication of an electron multiplier. Electrons leaving the photocathode have a kinetic energy on the order of 1 eV or less. The creation of an excited electron within the dynode material requires an energy at least equal to the bandgap, which typically may be of the order of 2-3 eV. Therefore, the the kinetic energy of electrons is increased by the accelerating voltage from the cathode to the anode. However only a small fraction of the excited electrons has the right direction and enough energy to reach the next dynode and contribute to the secondary electron yield.

The secondary electron yield is a sensitive function of incident electron energy. Finding the energy value which maximizes this function is not easy. On the one hand, low-energy electrons provide little energy for the secondary emission. However, because the penetration depth is not large, most of these excited electrons will be formed near

29

the surface. On the other hand high energy electrons excite more electrons but at greater average depth. Therefore they have less probability to escape from the dynode

As said before, there are various types of dynodes system and each one exhibits differents characteristics. The R760 PMT model from HAMAMATSU, used in PLUME, has a linear-focused dynodes system type, which is used in head-on photomultiplier tubes.

2.2.4 Anode

The anode of a PMT is the last electrode. It is placed at the end of the dynodes chain and has the purpose to collect secondary. It also outputs the electron current to an external circuit for the signal acquisition.

Anodes are carefully designed to have a structure optimized to intercept the electron trajectories. They are generally fabbricated in the form of a rod, plate or mesh electrode. In order to minimize space charge effects, anode is arranged so that an adequate potential difference can be established between the last dynode and the anode to obtain the largest possible current.

2.3 Characteristics of PMT

The output signal of a PMT is the product of all the processes which occur in the different components of the device. The performances of a PMT can be evaluated by studying various characteristics depending on the physics of these processes. Here the the most significant characteristics are described in detail.

2.3.1 Quantum efficiency

The photoemission process that occurs in the photocathode is a statistical process which can be quantified in several ways. One of the most important characteristics for a PMT is the quantum efficiency (QE). The quantum efficiency is theoretically defined as

$$QE = \frac{number\ of\ photoelectrons\ emitted}{number\ of\ incident\ photons}. \tag{2.6}$$

The Eq. of the QE of a given PMT can be written, in a more practical way, as function of the light wavelenght λ

$$QE(\lambda) = (1 - R)\frac{P_\nu}{k} \cdot \left(\frac{1}{1 + \frac{1}{kL}}\right) \cdot P_s, \tag{2.7}$$

where R is the reflection coefficient, k is the full absorption coefficient of photons and P_ν is the probability that light absorption may excite electrons to a level greater than the vacuum level barrier (see Section 2.2.2). For a chosen material, these three factors
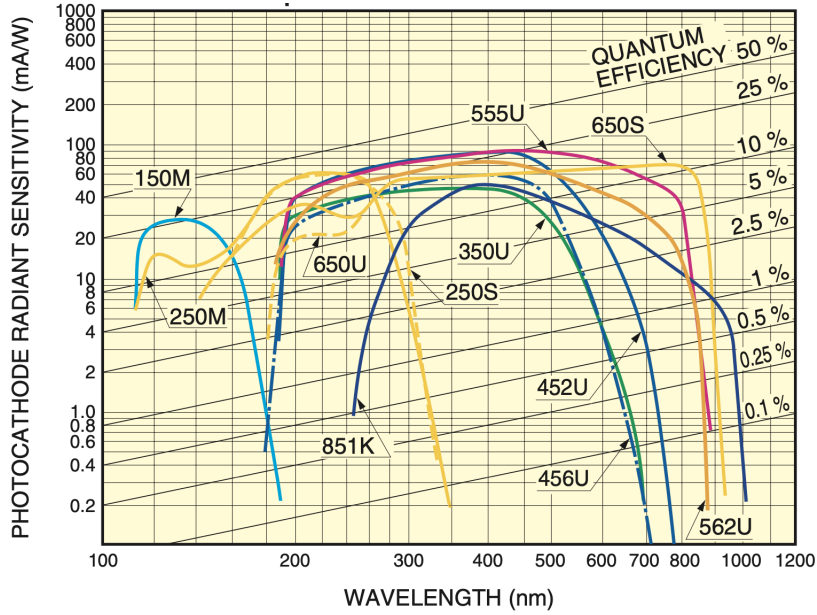
Figure 2.7: Typical spectral response characteristics [34]. Different coloured curves corresponds to different photocathode materials. The abbreviations corresponds to those used in Ref. [34].

are constant. Therefore, the two factors that dominate the QE behaviour, besides λ, are the mean escape lenght of the excited electrons L and the probability that electrons reaching the photocathode surface may be released into the vacuum P_s.

The measurement of the spectral response characteristic, and therefore of QE is usually performed through another quantity: the radiant sensitivity S_k. It is defined as the ratio between the photoelectric current generated by the photocathode and the incident radiant flux. The relation between the QE and the S_k becomes

$$QE(\lambda) = \frac{hc}{\lambda e} \cdot S_k. \tag{2.8}$$

The typical S_k (QE) characteristic for the major photocathodes is illustrated in Fig. 2.7. From the Fig. 2.7, it's evident the strong dependance of the quantum efficiency on the wavelength of the incident light. The sensitivity at large values of λ is largely limited by the reduced absorption of light in the photocathode. The electrons no longer have sufficient energy to escape the surface of the photocathode and the response drops to zero. The response at the opposite end of the scale does not depend on the photocathode itself but rather of the window. The maximum value of the QE is usually below 30%.

31

2.3.2   Gain

Another important characteristic describing a PMT is the so-called gain. It measures the efficiency of the electron multiplications performed in the dynodes system. The gain can be defined as the number of electrons which reach the anode, generated by the chain multiplication of a single photoelectron emitted from the photocathode.

Once an electron reach a dynodes, emits a number of secondaries in a statistical way. The overall multiplication factor for a single dynode is given by

$$\delta = \frac{number\ of\ secondary\ electrons\ emitted}{primary\ incident\ electron}. \tag{2.9}$$

The quantity δ is a function of the interstage voltage of dynodes ΔV, and can be written as

$$\delta = A \cdot \Delta V^k, \tag{2.10}$$

where A is a constant and k depend on the structure and material composing the dynodes. The photoelectron current I_k generated in the cathode strike the first dynode and generate a current composed by secondary electrons I_{d1}. The multiplication factor at the first step, is

$$\delta_1 = \frac{I_{d1}}{I_k}. \tag{2.11}$$

The secondaries produced at the surface of the first dynode have very low energies, typically a few eV. Thus, they are quite easily guided by another electrostatic field established between the first dynode and a second similar dynode.

The process is repeated as many times as the number of dynodes in the PMT. At each step, the multiplication factor is

$$\delta_n = \frac{I_{dn}}{I_{n-1}}. \tag{2.12}$$

Therefore, assuming the PMT has a N stage dynodes system, the anode current is given by

$$I_a = I_k \cdot \eta_{eff} \prod_{n=1}^{N} \delta_n, \tag{2.13}$$

where η_{eff} is the collection efficiency, defined as the ratio of the number of pulses output from the anode to the number of photoelectrons emitted from the photocathode.

The gain of the PMT is by definition the ratio of I_a to I_k

$$G = \frac{I_a}{I_k} = \eta_{eff} \prod_{n=1}^{N} \delta_n. \tag{2.14}$$

DELTA FUNCTION LIGHT
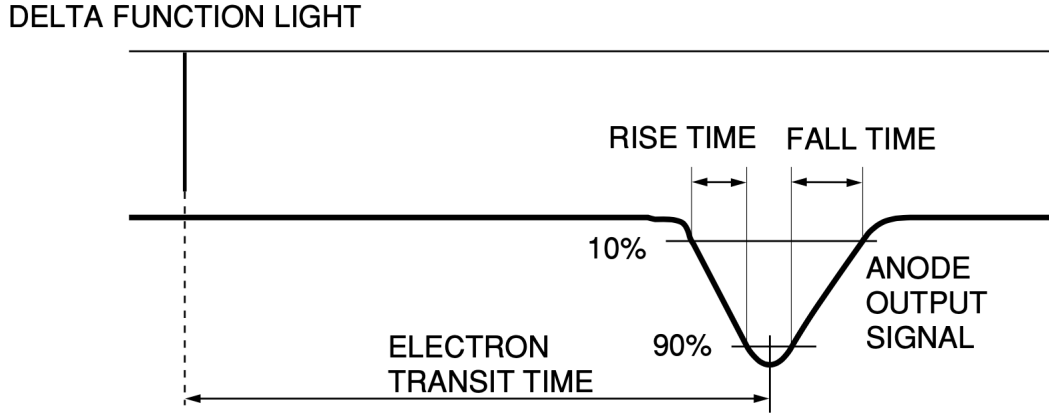
Figure 2.8: Example of a typical anode output signal of a PMT device illuminated by a delta function light [34].

Assuming the case of a PMT with $\eta_{eff} = 1$ and an equally-distributed voltage divider, the relation between the gain and the interstage voltage of dynodes becomes

$$G = \delta^n = (A \cdot \Delta V^k)^n. \tag{2.15}$$

From the Eq. 2.15 the dependence of the gain on the supply voltage can be studied. In the computation above, δ is assumed being a constant. Therefore under fixed operating conditions, all output pulses that originate from a single photoelectron would then have the same amplitude. In practice, the emission of secondary electrons is a statistical process and the value of δ at a given dynode will fluctuate from event to event about its mean value.

2.3.3 Time characteristics

Knowing the time response of a PMT is crucial in many particle physic applications. Photomultipliers tube are devices with a fast time response. The time required for photoemission in the photocathode or secondary emission from dynodes is very short (0.1 ns or less). Therefore, the time characteristics of the PMT are determined exclusively by the electron trajectories.

The response time of an anode output signal is illustrated in Fig. 2.8. Assuming the emission light as a delta-function, the response time is defined as the sum of the electron transit time, the rise time and the fall time. The rise time is defined as the time for the output pulse to increase from 10% to 90% of the peak pulse height. Conversely, the fall time is defined as the time required to decrease from 90% to 10% of the peak output pulse height. The electron transit time of a PMT is defined as the average of the time

33

difference between the arrival of a photon at the photocathode and the collection of the subsequent electron shower at the anode. In PMT of various designs, electron transit times range between 20 and 80 ns.

If the pulse signal is sharp enough, the rise and fall time are well defined and much smaller than the transit time. In this case the time width of the pulse of electrons arriving at the anode is small and the PMT has a good time resolution. The width of the time signal is called transit time spread.

In order to have a small transit time spread, all the electrons emitted over the large photocathodes must be collected at the same time. The region between the photocathode and first dynode is critical for this purpose. To allow uniform collection over large photocathodes, this distance is kept fairly large compared with interdynode distances. The difference in paths between a photoelectron leaving the center of the photocathode and one at the edge is often a dominant factor in the observed spread in transit time.The photocathode is often curved to minimize the transit time spread across its diameter. Another source of transit time spread is the distribution in initial velocities of photoelectrons leaving the photocathode. This effect can be minimized by using a large voltage difference between the photocathode and first dynode.

The amount of transit time spread observed for a specific pulse also depends on the number of initial photoelectrons per pulse. In the present analysis the time measurements are performed in single photoelectron condition, explained later, so this contribution to the resolution is minimized.

The time spread attributable to the multiplier section also decreases with increasing interdynode voltage, and the best timing performance is normally obtained by operating the tube at maximum voltage permitted by the factory ratings.

2.3.4   Linearity

The gain factor in nearly all PM tubes remains constant for pulses that range in size from a single photoelectron to many thousands. Under this condition, a linear relation exists between the amplitude of the signal collected at the anode and the the number of photoelectrons emitted. The number of photoelectrons is directly proportional to the mean number of photon impinging the PMT window. Therefore, the linear relation can be extended to the intensity of the light reaching the PMT. This characteristics of the PMT can be referred to as linearity.

The photomultiplier tube exhibits good linearity in anode output current over a wide range of light levels. However, if the intensity of the incident light increase too much, the signal current begins to deviate from the ideal linearity. The primarily cause of a non-linearity response of the device at this condition is the linearity characteristics near the anode. The anode linearity is limited by two factor, the space charge effects between the last dynode and anode, and the change in the voltage-divider voltage.

When the incident light is pulsed, and the PMT works in pulsed mode, as happen for

the R760 PMT in PLUME, the mainly effect is the space charge effects. In this case, if the light pulse entering a photomultiplier tube has an high intensity, the electron density between the last dynodes and anode increases too much. The buildup of space charge affects the trajectories of electrons in this region and causes current saturation. the space charge effects is heavily dependent on the electric field distribution and intensity between each dynode. Therefore, the structure of the dynodes systems plays an important role in the conservation of the linearity of a PMT. In general, any dynode type provides better pulse linearity when the supply voltage is increased, or in other words, when the electric field strength between each dynode is enhanced. In Section 3.4, the dependence of the linearity on the intensity of impinging light will be studied for all the R760 PMT in pulse mode.

When a PMT device is illuminated with a continuous light input, the change in the voltage-divider voltage is the primarily cause of linearity deviation. The cause of this effect are related to the currents flowing in the divider circuit coupled with the PMT. By looking at a divider circuit, as that one used in the elementary modules of PLUME, Fig. 1.4, the current components are two. The current produced by the supply voltage I_b, in this set up, has an opposite direction to the signal current produced by the PMT I_s. Therefore, the current flowing in the divider circuit is the difference by the two currents,

$$I_d = I_b - I_s. \tag{2.16}$$

The reduction of the divider current can be neglected if the anode output current is small. However, when the incident light level increases, the I_s current flow act to reduce I_b. This causes a loss of the interstage voltage of the latter dynodes and a consequent variation of the linearity.

A PMT may also be affected by cathode linearity characteristics, when it's operated at a low supply voltage and large current. This is due to the electrical resistance of the photocathode materials and to the area of the photocathode

2.3.5 Dark current

As all the devices, even the PMTs have sources of noise. These, produce small amount of currents flowing in the photomultiplier tube even when it operates in a completely dark state. The causes of the presence of the dark current in a PMT are divided in six categories. Their contribution to the total dark current depend on the value of the supply voltage as shown in Fig. 2.9 [34]. A brief description of the sources of noise in a PMT is given below.

Thermionic emission

Usually, the most significant source of random noise from a photomultiplier tube results from thermionic electrons spontaneously emitted by the photocathode. The main contri-
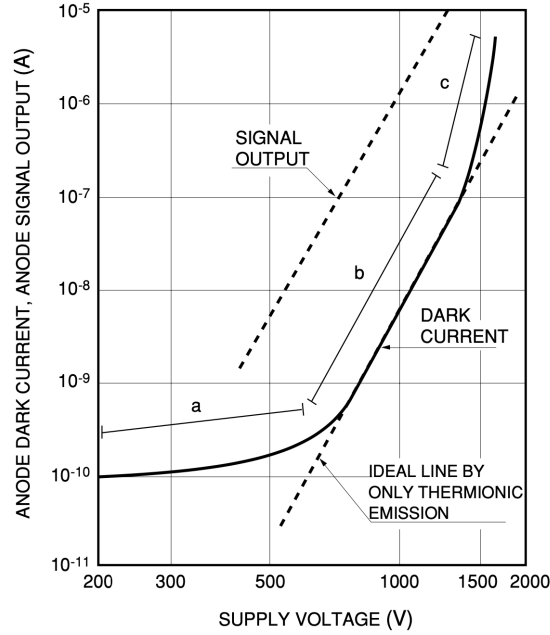
Figure 2.9: Graph of typical dark current vs supply voltage [34]. The graph is divided in three region: low voltage (a), medium voltage (b) and high voltage (c).

bution to the total dark current, from the thermionic emission, is given when the supply voltage is between 500 V and 1500 V. The current generated by this process is governed by [35]

$$I_{TE} = CT^{5/4}exp\left(-\frac{e\Psi}{KT}\right), \tag{2.17}$$

where Ψ is the work function, e is the electron charge, K is the Boltzmann constant, C is a constant and T is the temperature. The Eq. 2.17 indicates the thermal emission as a function of the photocathode work function and the temperature. Therefore I_{TE} will depend on the materials too.

The rate at which these pulses are observed is proportional to the area of the photocathode. Typical spontaneous emission rates at room temperature are in the range of 10^2-10^4 electrons/cm^2.

Leakage current

The PMT handle very low currents, in the range between several nA and 100 μA. Therefore, the choice of the insulating materials used in the devices is important in order to limit the leakage current. The contribution of the leakage current to the total dark current is larger at low values of supply voltage (< 500 V). A leakage current may be

36

generated between the anode and the last dynode inside a tube. It may also be caused by imperfect insulation of the glass cover of the PMT and base, and between the pins of the socket at the end of the PMT.

Scintillation from materials

Scintillation from the glass envelope or electrode support materials Sometimes can happen that some electrons emitted from the photocathode or dynodes follow wrong trajectories and miss the surfaces of the dynodes. If these stray electrons impinge on the glass envelope, scintillations may occur and result in dark pulses. Another possible process is the impinging on the glass envelope of stray electrons caused by metal case of the PMT.

Field emission

If a photomultiplier tube is operated at an excessive voltage, electrons can be emitted from the dynodes by the strong electric field. This phenomenon causes the dark current to increase abruptly. It occurs in region "c" in Fig 2.9 and shortens the life of the photomultiplier tube considerably.

Ionization of residual gases

The interior of a photomultiplier tube is kept at a vacuum around 10^{-5}-10^{-6} Pa. Even so, residual gases can be still present in the device. The molecules of these gases may be ionized by collisions with electrons and produce positive ions. Then, the ions may strike the front stage dynodes and the photocathode and produce many secondary electrons, resulting in a large noise pulse output, called an afterpulse [36].

Scintillation from cosmic rays

This contribution comes from the Cherenkov emitted light of muons, present in the cosmic rays, which interact with the glass envelope of the PMT. However, in the case of PLUME, which operates in a very dense environment and is installed underground, this contribution results insignificant.

Chapter 3

PMTs characterization

In this Chapter, the results of the characterization of the 29 R760 PMTs, performed in the optic laboratory of the University of Bolognaand INFN, are presented. Four characteristics are measured and studied: the gain, the transit-time drift, the charge linearity and the dark current. For each one of these, the experimental setup, the measurement procedure and the results are described in detail.

3.1 Characterization of the PMTs

The characterization of a PMT consists in measuring fundamental characteristics which define the behavior of the device. The main characteristics of a PMT are described in the Section 2.3. In particular, four of them have been measured in order to understand correctly the operation of the devices at LHCb

- the gain or current amplification;

- the transit time drift (t_{ttd});

- the charge linearity;

- the dark current.

The LHCb group of the INFN-Bologna has been in charge of characterizing 29 PMTs, from serial number EA3543 to EA3573 (EA3555 and EA3571 are missing), while the LHCb group of CNRS-Orsay additional 24. In this document are presented the results obtained in the Bologna's laboratory.

3.2 Gain

The gain or current amplification of a PMT is the ratio of the anode current and the current from the photocathode. As explained in Section 2.3.2, the gain G can be expressed as a function of the secondary emission ratio δ of the n dynodes composing the device, by

$$G = \delta^n = (A \cdot \Delta V^k)^n, \tag{3.1}$$

where A is a constant, ΔV is the interstage voltage of dynodes and k is determined by the structure and material composing the dynode. For the practical use of the PMTs in PLUME, it's useful to have the relation between the gain and the anode to cathode supply voltage V. The expression in 3.1 can be written as

$$G = \left\{ A \cdot \left(\frac{V}{n+1} \right)^k \right\}^n = \frac{A^n}{(n+1)^{kn}} \cdot V^{kn} = \alpha \cdot V^{kn} = \alpha V^{\beta}, \tag{3.2}$$

where the coefficient $A^n/(n+1)^{kn}$ and the exponent kn are redefined as α and β. The interstage voltage of dynodes E, in the expression above, is replaced with the high voltage applied at the cathode level and divided by $n+1$. This relation is obtained from the PMT divider circuit, shown in Fig. 1.4. The resistors between the dyodes decrease the voltage by the same quantity following the Ohm law ($V = IR$).

From Eq. 3.2, it is clear that the gain is proportional to an exponential power ($\beta = kn$) of the supply voltage. The PMT model R760, used in PLUME, has linear-focused dynodes structure composed by 10 dynodes with a constant $k = 0.8$ [34]. Therefore, the charge amplification goes as the $G \propto V^8$. This means that the photomultiplier tube is extremely sensitive to fluctuations in the power supply voltage.

3.2.1 Experimental setup

The PMT under study is fixed on a support inside a metal dark box, in order to avoid any light coming from the outside. The source of light is a Picosecond Diode Lasers with Driver of ALPHALAS [38], with a standard wavelength of 405 nm and a pulse width of 25 ps. The repetition rate of the laser is set to 500 Hz, in pulsed mode. The intensity of the light incident on the PMT was varied by placing different neutral density filters along the light path.

Two different devices are used for the measurements of the signal current. For the first nineteen PMTs, a $5^{1/2}$-digit Model 6485 Picoammeter, by Keithley, having a resolution of 1 pA in a current range of 200 nA [39] is used. For the last PMTs, a DAQ6510 Data Acquisition and Logging, Multimeter System [40], having a resolution of 10 pA for the 1 μA. To perform the first measurement of gain at 1250 V, the signal of the PMT is collected by a digitizer DRS4 Evaluation Board provided by the Paul Sherrer Institute (PSI) [41]. The DRS4 chip is a Switched Capacitor Array (SCA) capable of
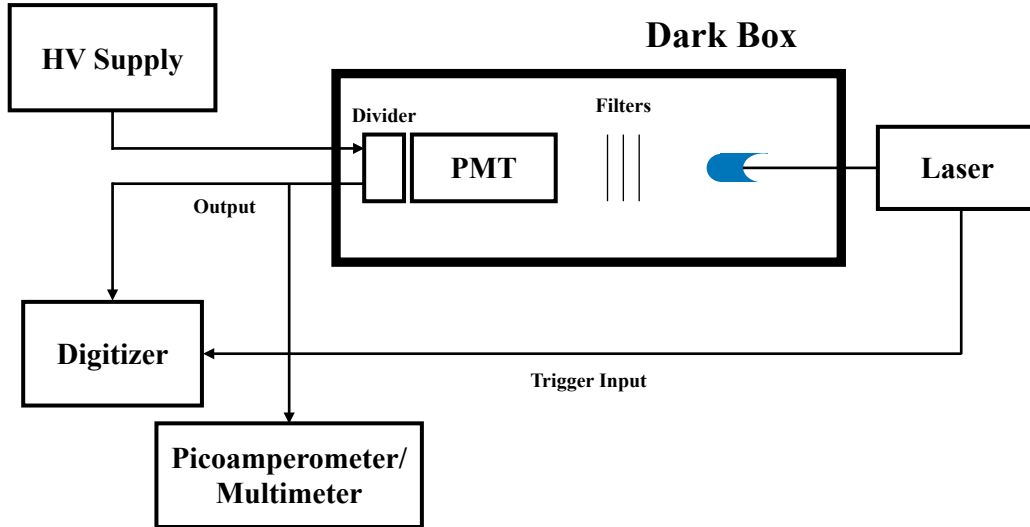
Figure 3.1: Scheme of the experimental setup used for the gain measurements.

digitizing eight channels at sampling speeds up to 5 GSPS and 1024 sampling points. The signal current is connected to the channel 1 of the digitizer by a SMA connector. The trigger from the laser, goes to the MCX connector of the Trigger IN (TTL input 50 Ohm terminated). The power supply is provided by the 40 Channel High Voltage System SY127 from CAEN [42]. The same high voltage system is used for all the measurements. The a scheme of the experimental setup is illustrated in Fig. 3.1

3.2.2 Single photoelectron

The logZero method needs a threshold value for the integrated charge signal. Therefore, the measure of the absolute gain is fundamental for correct functioning of the luminometer PLUME. The absolute gain is defined as the ratio between the anode current and the photocathode current, that in general is not accessible. The strategy to get the value of the absolute gain having only the information of the anode current is to work in the so-colled single photoelectron (S.P.E.) regime. This means that for each light pulse impinging the PMT window, only one photoelectron is ejected from the photocathod. In this way, the whole current amplified by the PMT comes from a single electron charge $(1.6 \times 10^{-19}\text{C})$, and the absolute gain can be computed by looking at the integrated charge returned by the PMT.

A pulsed flux of photons incident on the PMT photocathode produces photoelectrons via the photoelectric effect. The number of photons on the photocathode can be seen as a Poisson distributed variable [43]. Instead the conversion of photons into electrons and the collection by the dynode system is a random binary process. As a result, the probability

(a) *Pulse of Picosecond Diode Lasers trigger* (b) *Pulse of output signal of the PMT*
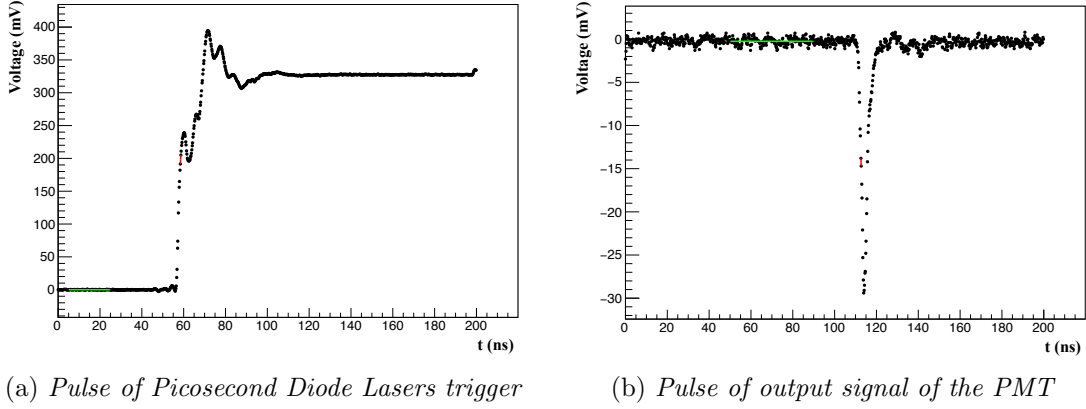
Figure 3.2: Example of a digitized trigger pulse (a) and EA3566 PMT digitized signal in S.P.E (b). The black points indicate the digitized waveform, with the green horizontal lines showing the estimated baseline. The red lines are the linear fit between the point immediately before and immediately after the 50% fraction of the two peaks, used to get the same timestamp for all the measurements.

of having a certain number of photoelectrons producing a signal can be expressed as a convolution of Poisson and binary processes which gives again a Poisson distribution. Thus, the number of detected events (N_k) produced by k photoelectrons follows

$$N_k = N_{tot} \frac{\nu^k}{k!} e^{-\nu}, \tag{3.3}$$

with N_{tot} corresponding to the total number of events collected by the PMT and ν is the most probable value of the Poisson distribution. In the S.P.E. condition the number of events N_k with $k > 1$ must be zero. This corresponds to have a value of ν such that the probability of the null events is $P(N_0) = N_0/N_{tot} \geq 0.95$. In this condition, most of the events will be null events and the remaining part will be only single photoelectron events. From Eq. 3.3 , setting $k = 0$, one gets

$$\nu = -\ln \frac{N_0}{N_{tot}} = 0.05. \tag{3.4}$$

Therefore, the value of ν can be estimated by counting N_0. This can be done by measuring the rate of events that exceed -5 mV threshold in the signal acquired by the digitizer. In Fig. 3.2, a single digitized PMT signal event and the laser trigger are shown. The expression for the estimate of ν becomes

$$\nu = -\ln(1 - R), \tag{3.5}$$

with R rate of events exceeding -5 mV. The value of ν, or R, depends on the mean number of photons hitting photocathode, n_{ph}, and the quantum efficiency QE. The

41
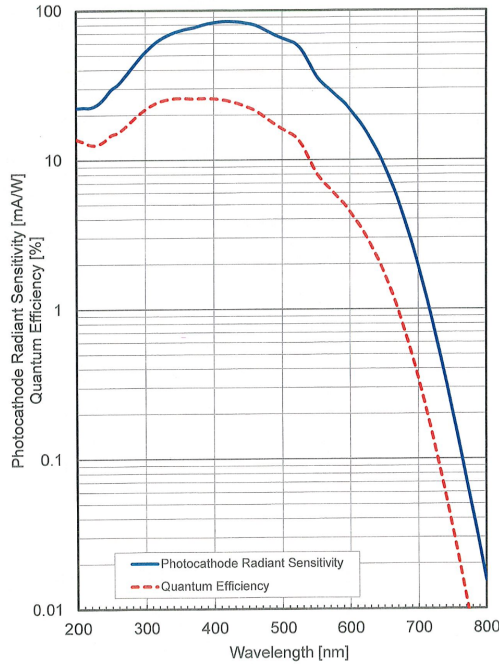
Figure 3.3: Quantum Efficiency (red dashed line) and Photocathode Radiant Sensitivity (blue continous line) of the PMT EA3513, model R760, measured by HAMAMATSU.

values of the QE, described in Section 2.3.1, for each PMT is already provided by HAMAMATSU. The maximum value of the QE is $\sim 27\%$ for a wavelength of 400 nm. The graph of the QE of one example PMT (EA3513) is shown in Fig. 3.3 [37]. Because QE, for a given value of light wavelenght, is fixed value, only the value of n_{ph} can be changed by changing the intensity of the light impinging on the PMT window. A set of attenuation lens is added in front of the window of the PMT until the right value of ν is found and the S.P.E. condition is obtained.

3.2.3   Measurements

Once the S.P.E. condition is achieved, the value of the absolute gain is measured for each PMT at the maximum supported voltage (1250 V). The gain is estimated from the fit to the integrated charge distribution of the PMT. The charge collected by the PMT anode is obtained from the integration of the PMT pulse signal. The integration time must be wide enough to contain all the signal from the PMT; in the present characterization, the integration window is chosen to be 40 ns. Since longer integration times increase the noise, the duration of the Laser pulse must be short. This is the reason why a width of 25 ps, is used. In order to subtract the baseline from the measurement, the data in the region of no signal (window of 50-90 ns for the output signal, and 5-25 ns for the trigger)
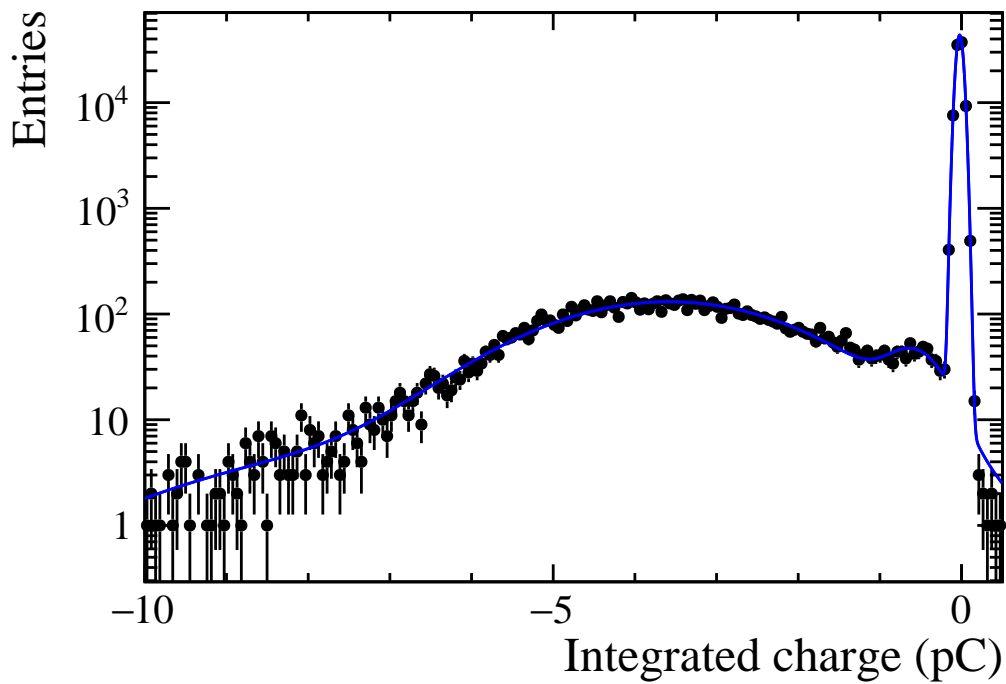
Figure 3.4: Distribution of 10000 events of signal from the PMT E3566. The maximum high voltage (1250 V) is applied to the PMT at S.P.E. The signal is shown by the black points and the blue line is the model of fit. The peak of zero photoelectron events is evident near to the 0. The wider peak at -3.569 pC is the gaussian of the single photoelectron events.

Parameter	Value	Error
ν	9.836×10^{-2}	1.104×10^{-3}
μ_p	-2.272×10^{-2} pC	1.432×10^{-4} pC
σ_p	4.332×10^{-2} pC	1.023×10^{-4} pC
μ_{c0}	-3.569 pC	1.800×10^{-2} pC
σ_{c0}	1.440 pC	1.802×10^{-2} pC
μ_{p2}	-5.688×10^{-1} pC	3.437×10^{-2} pC
σ_{p2}	3.135×10^{-1} pC	3.287×10^{-2} pC
f	9.947×10^{-1}	5.653×10^{-4}

Table 3.1: Parameters extracted by the fit of the Integrated charge signal of the PMT E3566 at 1250 V, in S.P.E condition.

are fitted with a straight line (green line in the Fig. 3.2). The constant value of voltage obtained by the fit is then subtracted from the signal.

An example of the distribution of the integrated signal of the serial number E3566 PMT is shown in Fig 3.4, where the highest peak near to the zero pC, ie the pedestal, is the distribution of the noise of the electronics for events without any observation of a photoelectron. The lower peak around -3.4 pC is the p.d.f. of the single photoelectron events. The reason why the gain is extracted at maximum value is because the two peaks are well separated. Since the PMT is in S.P.E. condition, the number of null events, N_0, is much higher then $N_{\geq 1}$.

To obtain the gain a model needs to be adapted to the data. Thus, the choice of the function used in the fit is crucial, and it must take into account both the Poisson distribution of the number of photoelectrons collected in the first dynode, and the distribution of the electron multiplication due to the dynode system. This last process can be approximated, in the absence of background, as a Gaussian distribution [44]. The model
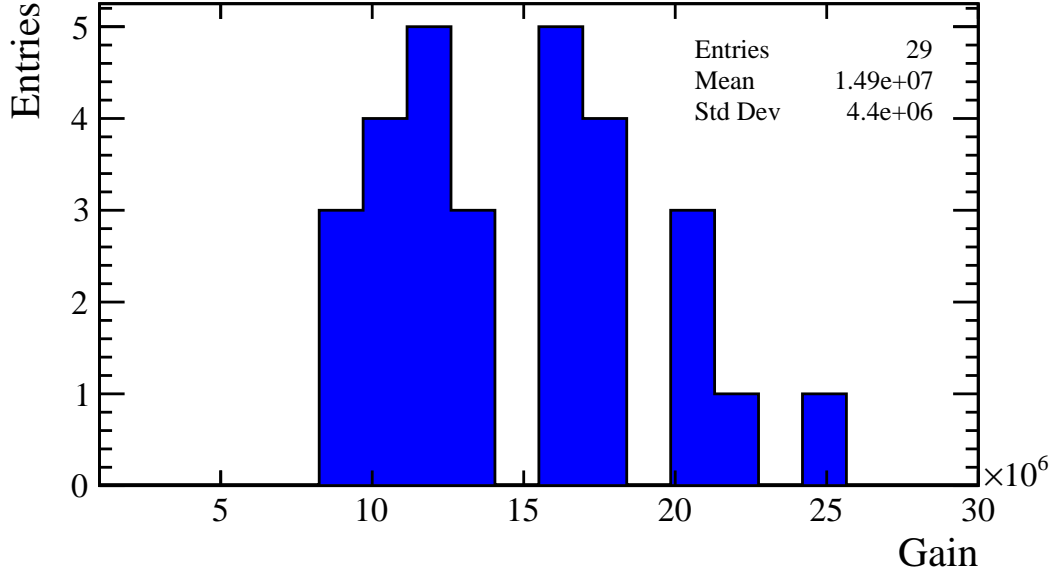
Figure 3.5: Histogram of the gain of the 29 PMTs powered with 1250 V.

describing the integrated charge emitted by a PMT, in S.P.E condition, is defined as

$$
M_{Charge}(x) = N \Bigg\{ f \left[\frac{\nu^0}{0!} e^{-\nu} \cdot \frac{1}{\sqrt{2\pi\sigma_p^2}} exp\left(-\frac{(x-\mu_p)^2}{2\sigma_p^2}\right) \right]
$$

$$
+ (1-f) \left[\frac{\nu^0}{0!} e^{-\nu} \cdot \frac{1}{\sqrt{2\pi\sigma_{p2}^2}} exp\left(-\frac{(x-\mu_{p2})^2}{2\sigma_{p2}^2}\right) \right] \tag{3.6}
$$

$$
+ \sum_{k=1}^{5} \frac{\nu^k}{k!} e^{-\nu} \cdot \frac{1}{\sqrt{2\pi k\sigma_{c0}^2}} exp\left(-\frac{(x-k\mu_{c0})^2}{2k\sigma_{c0}^2}\right) \Bigg\}.
$$

The first Gaussians describes the pedestal, centered around 0. The second one is due to a small contribution of the events of photoelectrons which have skipped the first dynode stage, so they perform a lower amplification. The last sum include the Gaussian of the events with $1 \leq k \leq 5$ photoelectrons. Even if the largest contribution, at S.P.E., comes from the $k = 1$ events, a small amount of events with $k > 1$ is still present. The mean of these Gaussian is parametrized as the mean of the single photoelectron gaussian times the number k, not accounting for any saturation of the electron multiplication. The parameters of the fit for the signal of PMT E3566 at 1250 V, taken as example, are presented in the Tab.3.1. The gain can be extracted by the parameters of the fit, with the relation

$$
G = -\frac{(\mu_{c0} - \mu_p)}{q_e} 10^{-12}, \tag{3.7}
$$

45

where the minus sign comes from the negative charge of the electron q_e. Therefore, because of the data are taken at S.P.E. regime, the absolute gain is directly deduced by the value of the peak of the distribution produced by a single photoelectron μ_{c0}. Since the pedestal is not exactly centered in zero, the offset μ_p is subtracted. From Eq. 3.7, the gain of the PMT E3566, at 1250 V, is $G(1250) = (2.24 \pm 0.01) \times 10^7$. The fit is performed for all the 29 PMTs. The histogram of the gains at 1250 V of power supply is shown in Fig. 3.5. The mean value of the gain is found to be $(1.493 \pm 0.003) \times 10^7$, where the error corresponds to the statistical fluctuations.

In order to measure the gain at different voltages, a different approach is employed. The laser is switched to continuous wave operation in order to have a constant light impinging on the PMT. Then the anodic current is measured by taking the average of 20 measurements performed in a 20 seconds time window. This measurement is performed for 13 different values of the supply voltage, from 1250 V to 650 V, with 50 V steps, for each PMT. The gain at a given voltage V can be related to the absolute gain measured at 1250V using the relation

$$G(V) = G(1250)\frac{I(V)}{I(1250)}, \tag{3.8}$$

where I(V) is the current measured. The gain vs voltage dependances are shown in the Figs. 3.6-3.9. The points are fitted with the function described by Eq. 3.2. The fitted exponentss β are shown in the Tab. 3.2. The mean value of β is found to be 7.736 ± 0.003, near to the expected value 8 [34]. In the last column of the Tab. 3.2, the values of the supply voltage for which the gain of each PMT is equal to 1.5×10^5 are reported. These values are critical for the PLUME operation, representing the value at which the minimum ionising particles traversing the luminometer will produce a charge of 3 pC.This value is considered as a reference for the running conditions. Therefore, the PMTs installed in the PLUME detector will work at that voltage, with small corrections from the calibration system.

PMT Serial Number	Gain at 1250 V	β	Voltage (V) for gain= 1.5×10^5
$EA3543$	$(1.801 \pm 0.009) \times 10^7$	7.635 ± 0.011	734
$EA3544$	$(1.358 \pm 0.009) \times 10^7$	7.693 ± 0.013	764
$EA3545$	$(1.162 \pm 0.006) \times 10^7$	7.816 ± 0.010	785
$EA3546$	$(8.826 \pm 0.005) \times 10^6$	7.790 ± 0.011	812
$EA3547$	$(2.076 \pm 0.012) \times 10^7$	7.626 ± 0.012	719
$EA3548$	$(1.063 \pm 0.010) \times 10^7$	7.720 ± 0.011	790
$EA3549$	$(2.096 \pm 0.009) \times 10^7$	7.695 ± 0.011	721
$EA3550$	$(1.627 \pm 0.010) \times 10^7$	7.607 ± 0.012	741
$EA3551$	$(1.665 \pm 0.007) \times 10^7$	7.719 ± 0.011	746
$EA3552$	$(1.731 \pm 0.007) \times 10^7$	7.577 ± 0.012	733
$EA3553$	$(1.254 \pm 0.012) \times 10^7$	7.821 ± 0.011	779
$EA3554$	$(1.225 \pm 0.014) \times 10^7$	7.821 ± 0.011	781
$EA3556$	$(2.023 \pm 0.009) \times 10^7$	7.913 ± 0.011	736
$EA3557$	$(2.562 \pm 0.010) \times 10^7$	7.824 ± 0.012	711
$EA3558$	$(1.616 \pm 0.013) \times 10^7$	7.573 ± 0.011	740
$EA3559$	$(1.686 \pm 0.006) \times 10^7$	7.604 ± 0.012	738
$EA3560$	$(1.615 \pm 0.010) \times 10^7$	7.828 ± 0.015	754
$EA3561$	$(1.046 \pm 0.007) \times 10^7$	7.894 ± 0.010	800
$EA3562$	$(1.834 \pm 0.012) \times 10^7$	7.524 ± 0.011	726
$EA3563$	$(1.193 \pm 0.005) \times 10^7$	7.633 ± 0.011	775
$EA3564$	$(1.119 \pm 0.011) \times 10^7$	7.936 ± 0.017	796
$EA3565$	$(8.871 \pm 0.010) \times 10^6$	7.784 ± 0.011	811
$EA3566$	$(2.213 \pm 0.007) \times 10^7$	7.703 ± 0.011	717
$EA3567$	$(1.771 \pm 0.007) \times 10^7$	7.631 ± 0.011	734
$EA3568$	$(1.319 \pm 0.027) \times 10^7$	7.599 ± 0.011	763
$EA3569$	$(1.036 \pm 0.006) \times 10^8$	7.868 ± 0.015	801
$EA3570$	$(8.781 \pm 0.009) \times 10^6$	7.838 ± 0.048	816
$EA3572$	$(1.349 \pm 0.011) \times 10^7$	7.862 ± 0.013	774
$EA3573$	$(9.816 \pm 0.010) \times 10^6$	7.813 ± 0.033	803

Table 3.2: Relevant parameters of the gain measurements. The values of the gain at 1250 V are extracted by the fit of the histogram of the integrated charge in S.P.E. regime with the model in Eq. 3.6. The β is the exponent of Eq. 3.2. The last column is the voltage at which the gain has a value of 1.5×10^5.
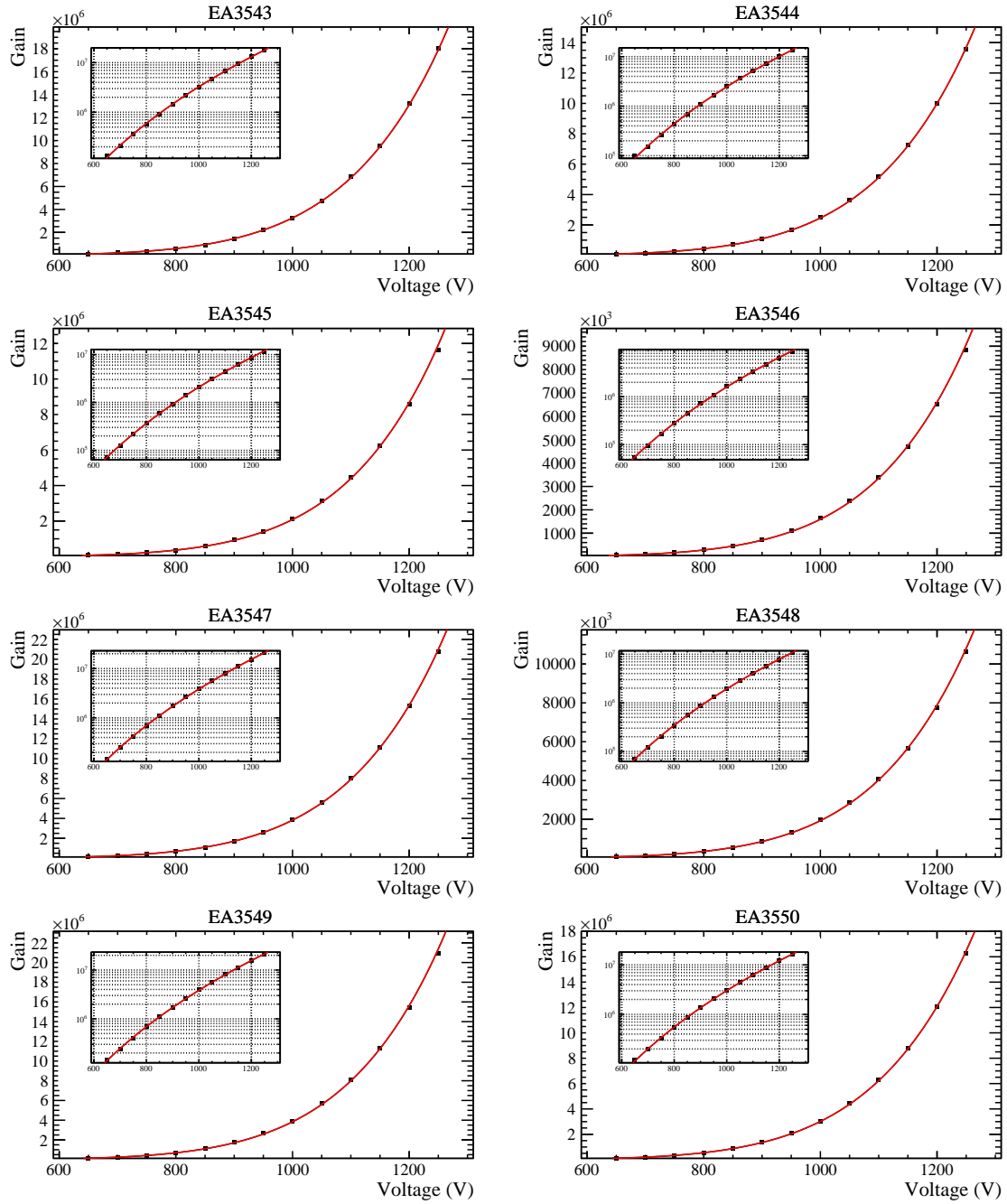
Figure 3.6: Gain vs voltage graphs of the PMTs from EA3543 to EA3550 characterized in Bologna. The black points are the gains extracted by the Eq. 3.8. The red line is the fit performed with Eq. 3.2. The vertical axis of the small window is in logarithmic scale.
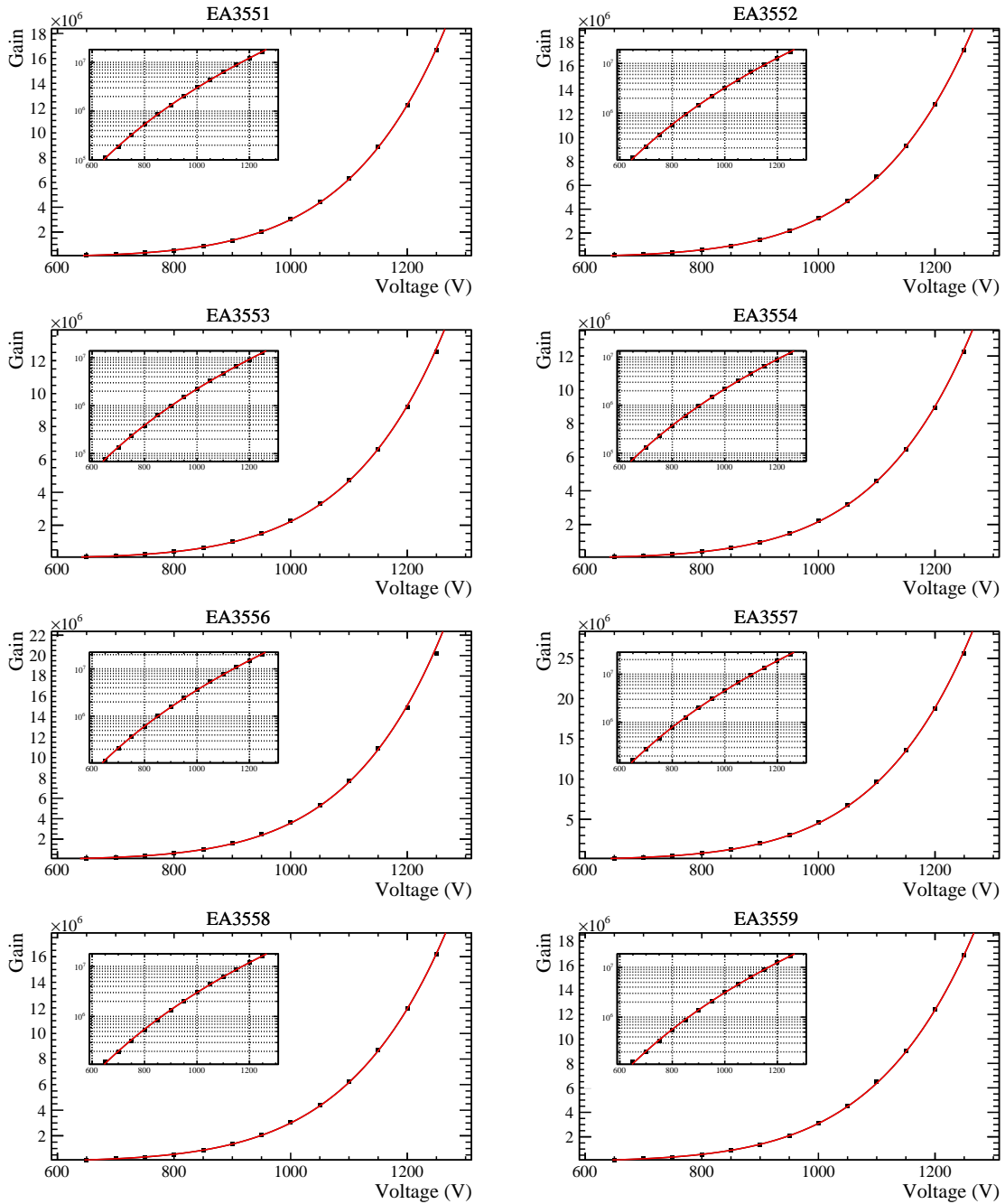
Figure 3.7: Gain vs voltage graphs of the PMTs from EA3551 to EA3559 (EA3555 is missing) characterized in Bologna. The black points are the gains extracted by the Eq. 3.8. The red line is the fit performed with Eq. 3.2. The vertical axis of the small window is in logarithmic scale.
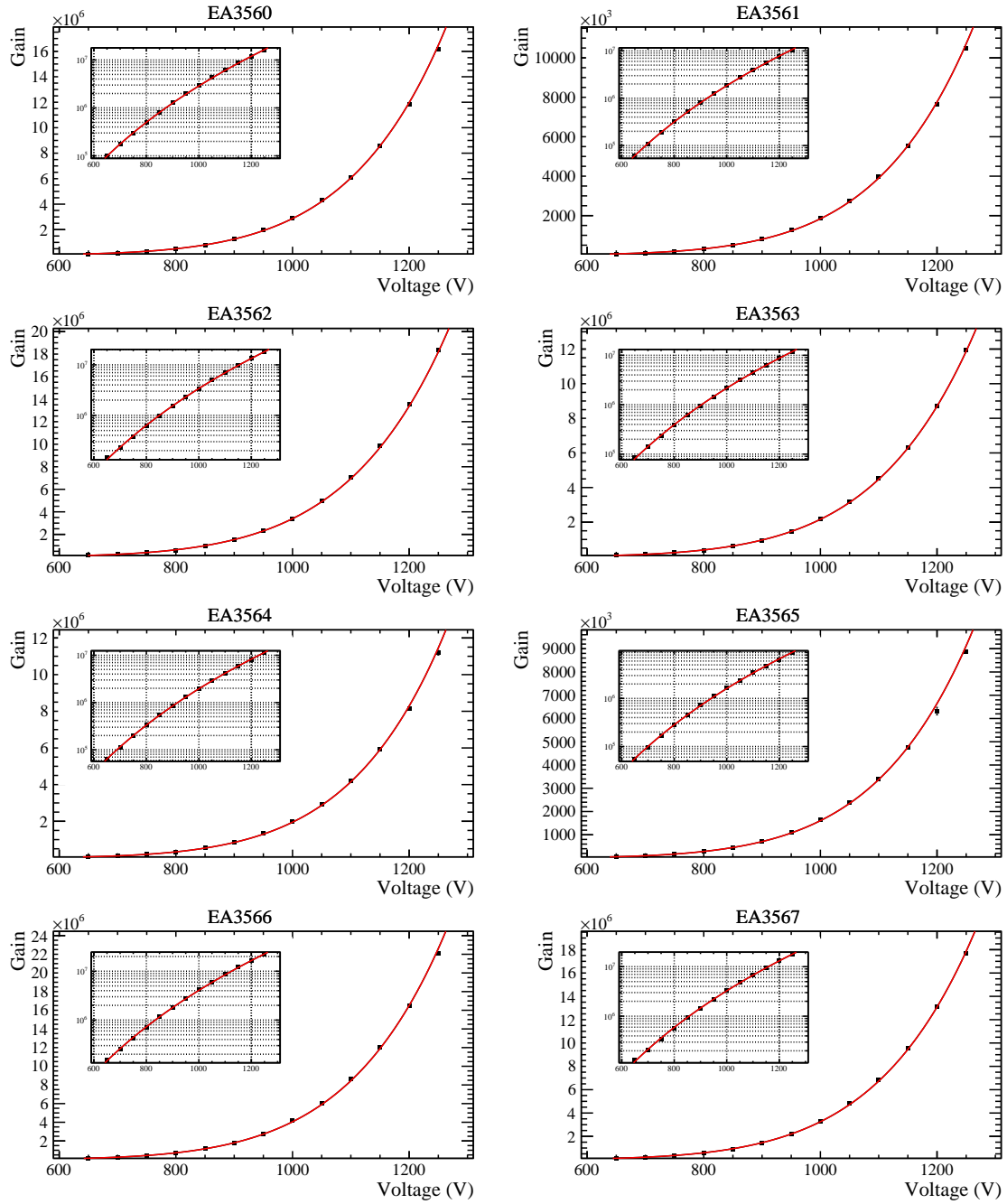
Figure 3.8: Gain vs voltage graphs of the PMTs from EA3560 to EA3567 characterized in Bologna. The black points are the gains extracted by the Eq. 3.8. The red line is the fit performed with Eq. 3.2. The vertical axis of the small window is in logarithmic scale.
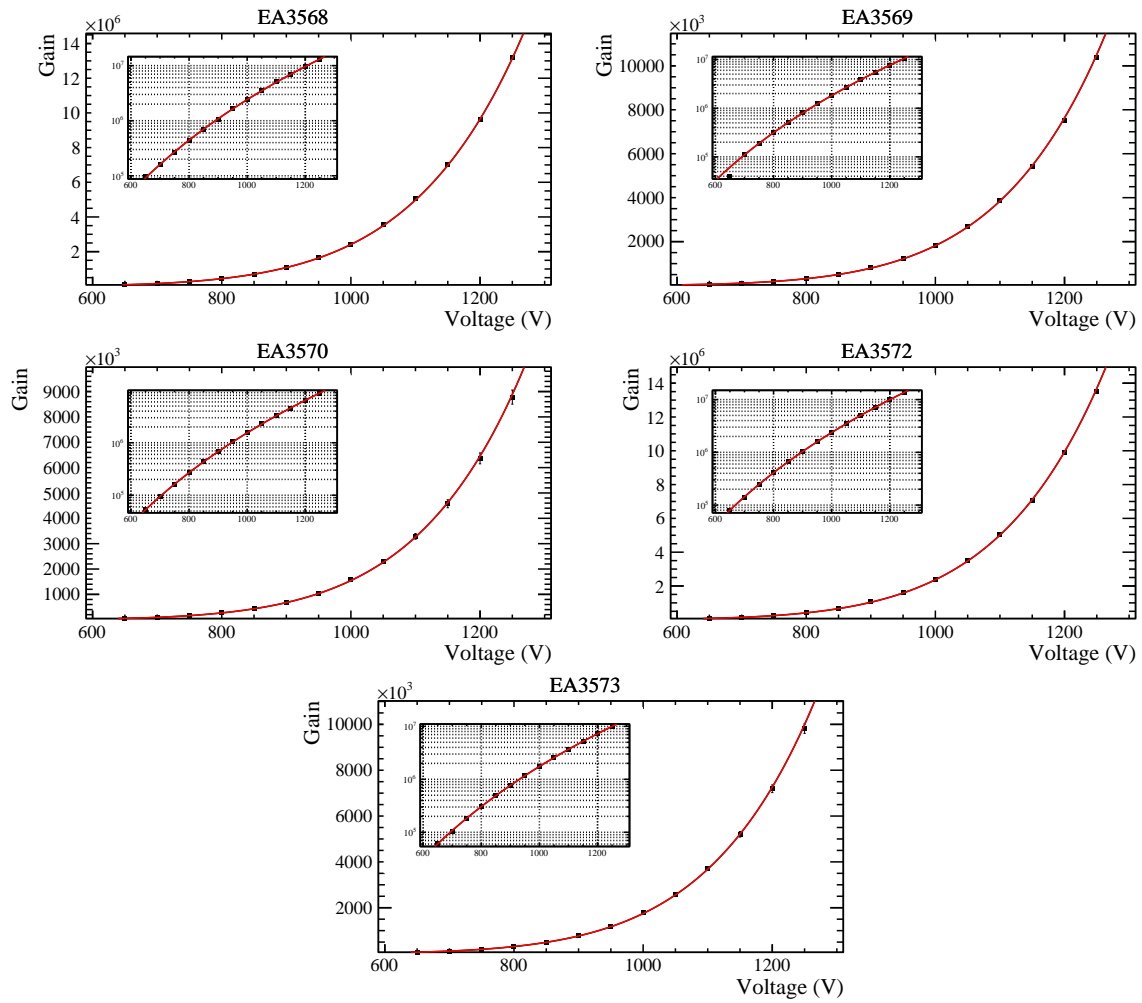
Figure 3.9: Gain vs voltage graphs of the PMTs from EA3568 to EA3573 (EA3571 is missing) characterized in Bologna. The black points are the gains extracted by the Eq. 3.8. The red line is the fit performed with Eq. 3.2. The vertical axis of the small window is in logarithmic scale.

3.3 Transit time drift

Knowing the time characteristics of the PMT is crucial for the synchronization of the PLUME electronics, during the data taking. The linear-focused dynodes type PMT, as the HAMAMATSU R760 model, can reach a time response between 50 and 60 ns. The velocity of a PMT signal is due to the contribution of different components, Section 2.3.3. The main contribution comes from the transit time of the electrons, which is the time it takes for the photoelectrons emitted in the photocathode to read the anode and release an electric signal. Because of all the others contributions are much more smaller than that one, the measure of the time response can be considered as the measure of the transit time. The electrons in the PMT are accelerated by the electric field present between the anode and the cathode. Therefore, increasing the electric field or equivalently the supply voltage, the electron transit speed improves and thus a shorter time response is obtained. The relation between the transit time and the voltage applied at the end points of the PMT comes from the conservation of energy. The electric energy acquired by the electrons in the path between two consecutive dynodes is equal to $W_{d_n-d_{n-1}} = q_e \Delta V_{d_n-d_{n-1}}$, where $\Delta V_{d_n-d_{n-1}}$ is the electric potential difference between the two dynodes. The total path of an electron travelling in the PMT is due to the sum of the distance between the 10 dynodes d plus the distance of the cathode from the first dynode d_{k-d_1} and anode from the last dynodes d_{10-a}. The velocity of the electrons in the PMT is non relativistic, so from a simple computation, the transit time becomes

$$
\begin{aligned}
t_{tt} = d_{k-d_1} \sqrt{\frac{m_e}{2 q_e \Delta V_{k-d_1}}} + d_{d_{10}-a} \sqrt{\frac{m_e}{2(K_{d_{10}-a} + q_e \Delta V_{d_{10}-a})}} \\
+ 9 \sum_{n=1}^{10} d \sqrt{\frac{m_e}{2(K_n + q_e \Delta V_{d_n-d_{n-1}})}}.
\end{aligned}
\tag{3.9}
$$

K_n and $K_{d_{10}}$ are the kinetic energies acquired by the electron, during the different steps of the path. The first line of the Eq. 3.9 contains the time spent by the electron to travel the first and the last section of its path; the second line is the time contribution due to the crossing of the dynodes system. In the circuit divider used for the PMT, see Fig. 1.4, the resistors between the cathode, anode and all the dynodes, have the same value, $R = 90$ kΩ. Thus, all the potential difference in Eq. 3.9 have the same value, equal to

$$
\Delta V = \frac{R}{R_{tot}} V,
\tag{3.10}
$$

related to the power supply. Combining the Eqs. 3.9 and 3.10, the dependence of t_{tt} to the power supply V results to be

$$
t_{tt} \propto \frac{1}{\sqrt{V}}.
\tag{3.11}
$$
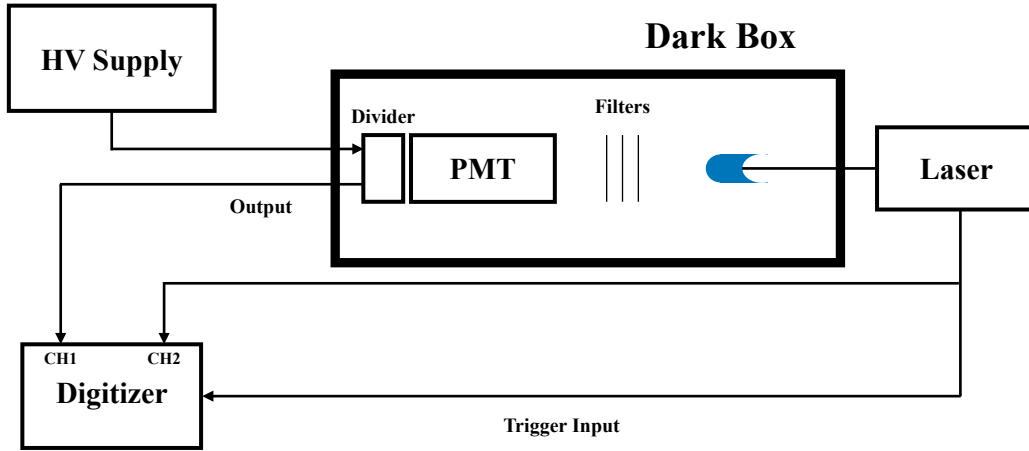
Figure 3.10: Scheme of the experimental setup used for the ttd measurements.

In order to study the variation of the t_{tt} in function of the supply voltage, the measurements of the transit time drift (t_{ttd}) are performed. The transit time drift is defined as the difference of two transit time at different value of supply voltage. It allows to measure the relative variation of the t_{tt} respect to the supply voltage.

3.3.1 Experimental setup

The experimental set up is similar to the set up used for the gain measurements. The PMTs are placed inside the dark box and the source of signal is the laser of ALPHALAS. The width pulse of the laser (25 ps) is sufficiently short compared to the light pulse width that can be detected by the photomultiplier tube R760. Thus, it can be regarded as a delta-function light source.

The configuration of the lens between the laser and the PMT window is changed for each voltage in order to have a value of the integrated charge close to 6 pC. This is done to have approximately the same charge density effects in the last steps of the PMT amplification system.

Data are acquired by the digitizer DRS4 Evaluation Board. The timestamps are then computed from the signal spectrum vs time.

The output signal of the tested PMT is connected to the channel 1 of the digitizer as before, while the laser trigger is split in two signals. The first one goes to the MCX connector of the Trigger IN and works as input trigger for the digitizer. The other trigger signal goes to the channel 2 of the digitizer, where it is acquired. The amplitude of the external trigger of lasers is equal to (5 ± 0.5) V [38], so the trigger signal passes through an attenuator before reaching the digitizer which has a maximum input voltage range of 500 mV. The scheme of the experimental set up is shown in Fig. 3.10.

(a) *Distribution of t_2*   (b) *Distribution of t_{tt}*
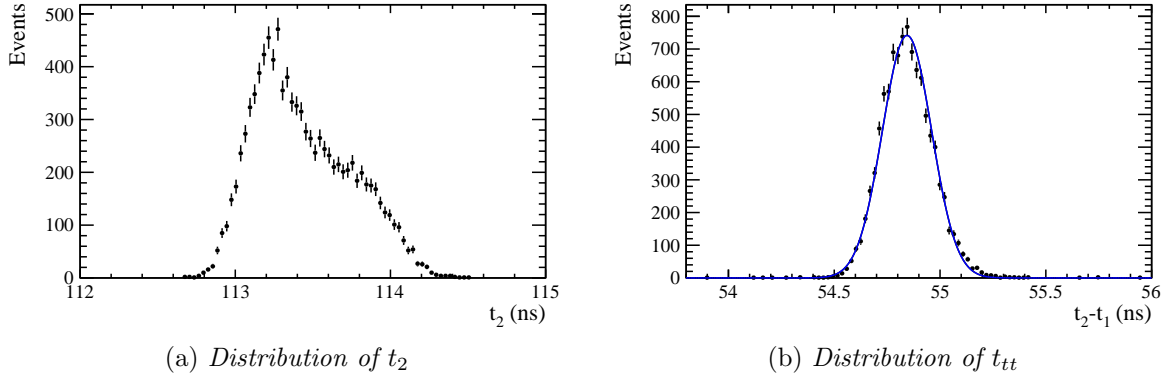
Figure 3.11: Histogram of 10000 measurements of the timestump t_2 (a) and the transit time $t_{tt} = t_2 - t_1$ (b) of the EA3566 PMT powered with 1000 V. The t_{tt} is fitted by a Gaussian distribution, blue line. The noise due to the jitter is present in the histogram of the t_2, while it is removed in the t_{tt}.

3.3.2   Estimation of the transit time

The transit time is measured as the time interval between the arrival of the laser pulse at the photocathode and the appearance of the output pulse of the PMT. The arrival time can be measured using a PIN photodiode placed at the same distance from the light source of the PMT or by looking at the light source trigger. The measurement of the time drift performed in this analysis follows the second method. The arrival time of light is thus directly provided by the trigger of the Picosecond Diode Lasers, assuming the instantaneous transmission of light from the output of the laser to the PMT.

To explain the procedure performed by the software to measure timestamps, the pulses of the laser trigger and the EA3566 PMT output in S.P.E. ,shown in Fig. 3.2, are taken as an example. The baseline is extract by the linear fit of the digitized waveform, in the time window 5-25 ns for the trigger, and 50-90 ns for the PMT signal. The fits are the green lines in the Fig. 3.2. This provide the zero level of the two pulses. The light arrival time t_1 and time of the output pulse of the PMT t_2 are extracted by looking at the constant fraction at 50% of the two signals. The same fraction is used for both trigger and the PMT signal. Using a constant fraction triggering instead of a simple threshold triggering avoids dependence of the trigger time on the signal's peak height. The timestumps t_1 and t_2 are estimated by a linear fit represented by red lines in Fig. 3.2, between the point detected immediately before and immediately after the 50% fraction of the two peaks. The transit-time can be expresses as the difference

$$t_{tt} = t_2 - t_1. \tag{3.12}$$

Because of the trigger of the laser is also used as the trigger of the digitizer, the two time measurements t_1 and t_2 are both affected to the the jitter of the Laser Pulse, considered
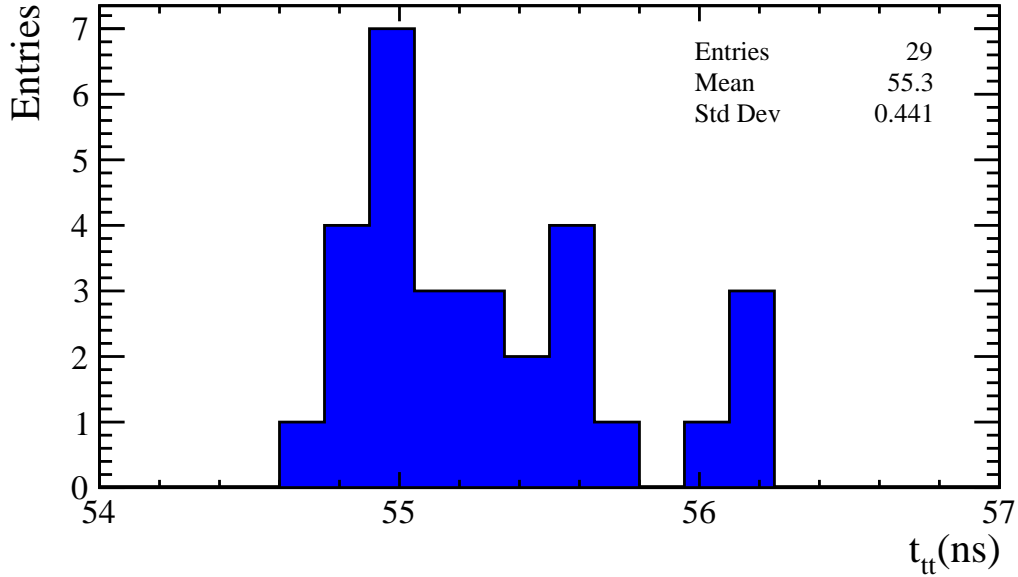
Figure 3.12: Histogram of the t_{tt} of the 29 PMTs powered with 1000 V.

as a delta, with the laser trigger. However by subtracting t_1 to the time of the output signal t_2 the jitter is removed.

Ten thousand measurements of the timestumps t_1 and t_2 are performed for each PMT and the differences $t_{tt} = t_2 - t_1$ are computed. The histograms of and t_{tt} for PMT EA3566 at 1000 V are shown in Fig. 3.11. Comparing the two histogram the removal of the noise due to the jitter is evident. The histogram of t_{tt} is fitted with a Gaussian model in order to get the mean of the transit time and the time resolution of the PMT. In the example case, the PMT EA3566 at 1000 V has a mean $t_{tt} = (54.841 \pm 0.001)$ ns and a time resolution $\sigma_{tt} = (0.116 \pm 0.001)$ ns.

3.3.3 Computation of the t_{ttd}

In order to study the dependence of the t_{tt} on the supply voltage, the measurement described before is performed for 13 voltages, between 650 and 1250 V. The histogram of the t_{tt} for all the PMTs at a voltage of 1000 V is presented in Fig. 3.12. The mean of the histogram is 55.300 ± 0.001 ns. The relative variation of the transit-time respect to the maximum possible voltage, in function of the supply voltage, is the transit-time drift, defined as difference

$$t_{ttd} = t_{tt}(V) - t_{tt}(1250), \tag{3.13}$$

where $t_{tt}(V)$ are the means of the distribution of the transit-time computed at different voltages. The value of the t_{ttd} as function of V are presented in Figs. 3.13-3.16 for each

PMT. The values of t_{ttd} show the trend of the Eq. 3.9, as expected. This function is drawn on each graph as a green line for comparison. The trend of the $t_{ttd}(V)$ follows the theoretical expectation. Looking at the graphs, the variation of the t_{ttd} in the studied voltage range does not exceed 6 ns.

3.4 Linearity

Linearity is defined as the linear relation between the intensity of the incident light and the output current (or equivalently the integrated charge) of the PMT. The photomultipliers installed in PLUME, will receive pulsed light signals from the particles produced in LHCb. Therefore, they operate in a pulsed mode. As explained in Section 2.3.4, the main contribution to the deviation of the PMT linearity, from the ideal linearity, is caused by the buildup of space charge in the region of the last dynodes and the anode. The electron density in the PMT will increase with the increasing of the intensity of the light pulse.

As said in the Section 3.2.3, the most probable value of the number of emitted photoelectrons ν is related to the level of the intensity of light imping the PMT, Eq. 3.3. If linearity is preserved, with increasing the intensity of light, the expected integrated charge of the PMT is extimated by the proportion

$$Q_{exp}(\nu) = Q_{low}\frac{\nu}{\nu_{low}}, \tag{3.14}$$

where Q_{low} is the measured integrated charge at low values ν_{low}. In the present analysis, in order to get the right value of ν, the power, or radiant quantity, of light is measured. The power of the light impinging on the PMT is expressed in units of watt (J/s) and defined as

$$W = N_{ph}E = \frac{N_{ph}hc}{\lambda}, \tag{3.15}$$

where N_{ph} is the mean number of photons per second, E is the energy of the photons, h is the Planck constant, c is the speed of light and λ is the wavelength of the laser. The ν is a linear function of the mean number of photon n_{ph}, thus relation 3.15 can be written in the form

$$W = \frac{n_{ph}fhc}{\lambda} = \frac{\nu fhc}{\lambda QE}. \tag{3.16}$$

f is the emission frequency of the laser mean number of photon per second N_{ph} is obtained from $n_{ph}f$. In the second passage the relation $\nu = n_{ph} \times QE$ is used. The wavelength and the frequency of the laser are kept constant during all the characterization. Therefore, the power will be directly proportional to the ν.
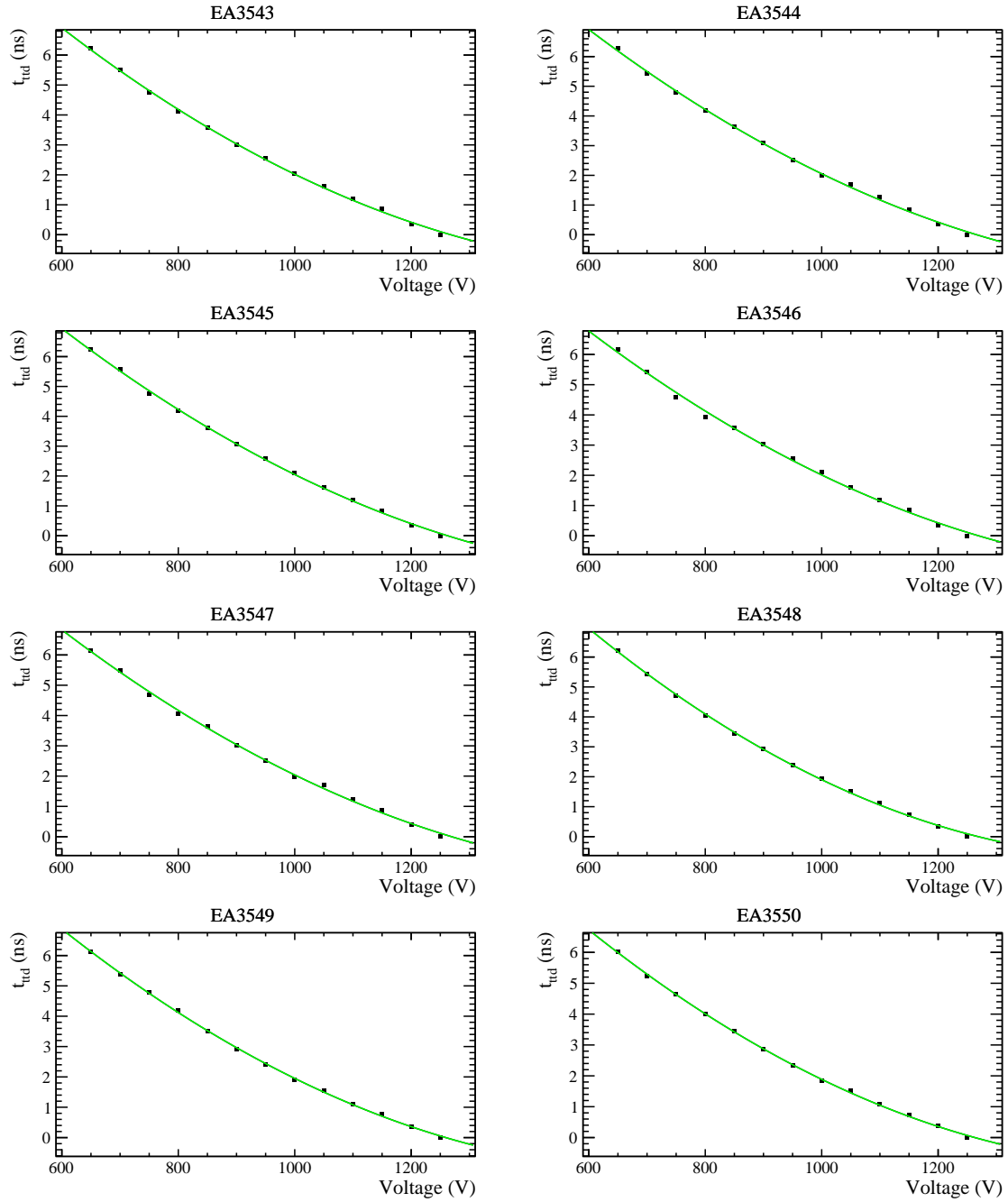
Figure 3.13: t_{ttd} vs voltage graphs of the PMTs from EA3543 to EA3550 characterized in Bologna. The black points are the t_{ttd} obtained from the Eq. 3.13. The green line is the theoretical expectation expressed in Eq. 3.9.

57
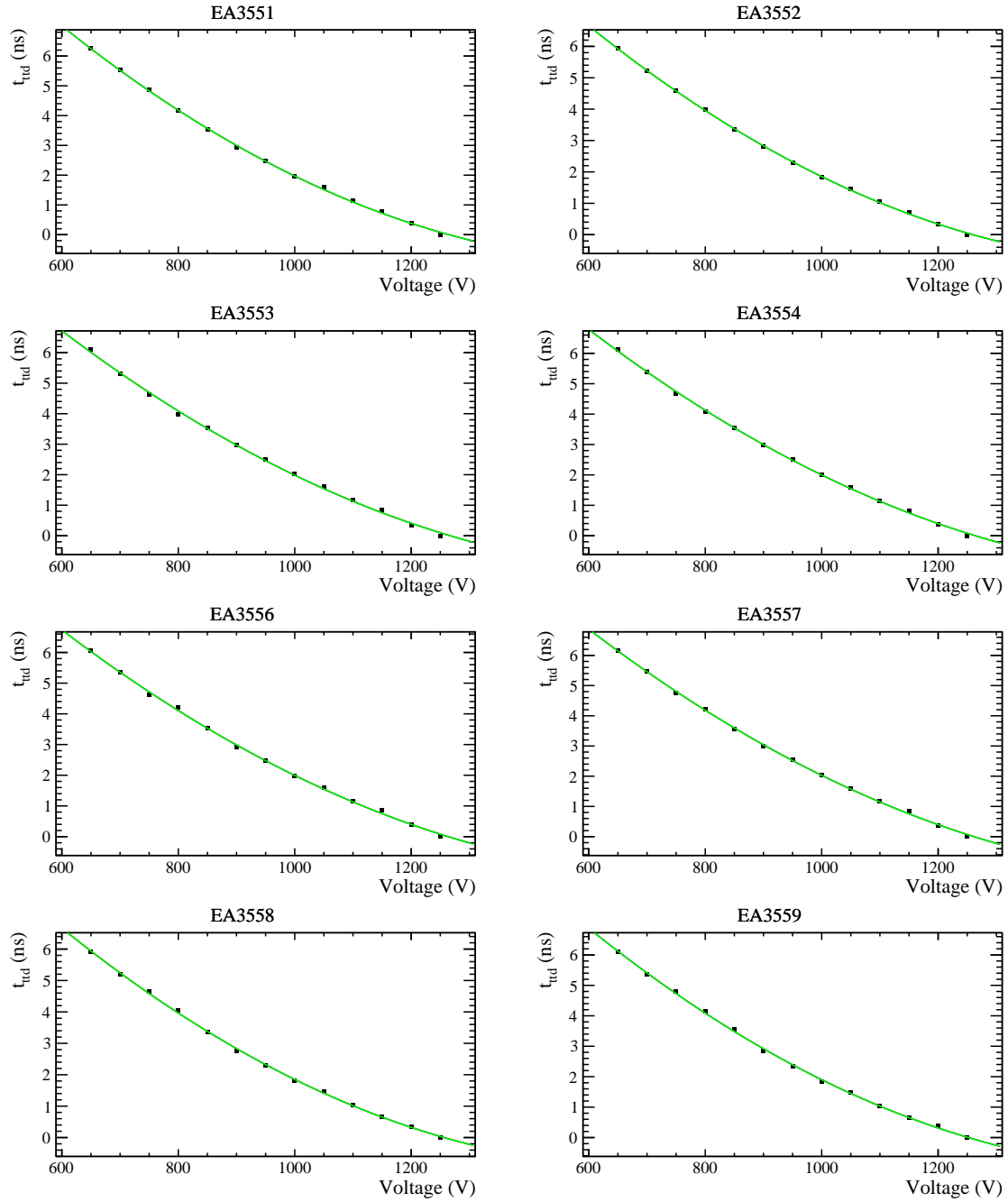
Figure 3.14: t_{ttd} vs voltage graphs of the PMTs from EA3551 to EA3559 (EA3555 is missing) characterized in Bologna. The black points are the t_{ttd} obtained from the Eq. 3.13. The green line is the theoretical expectation expressed in Eq. 3.9.

58
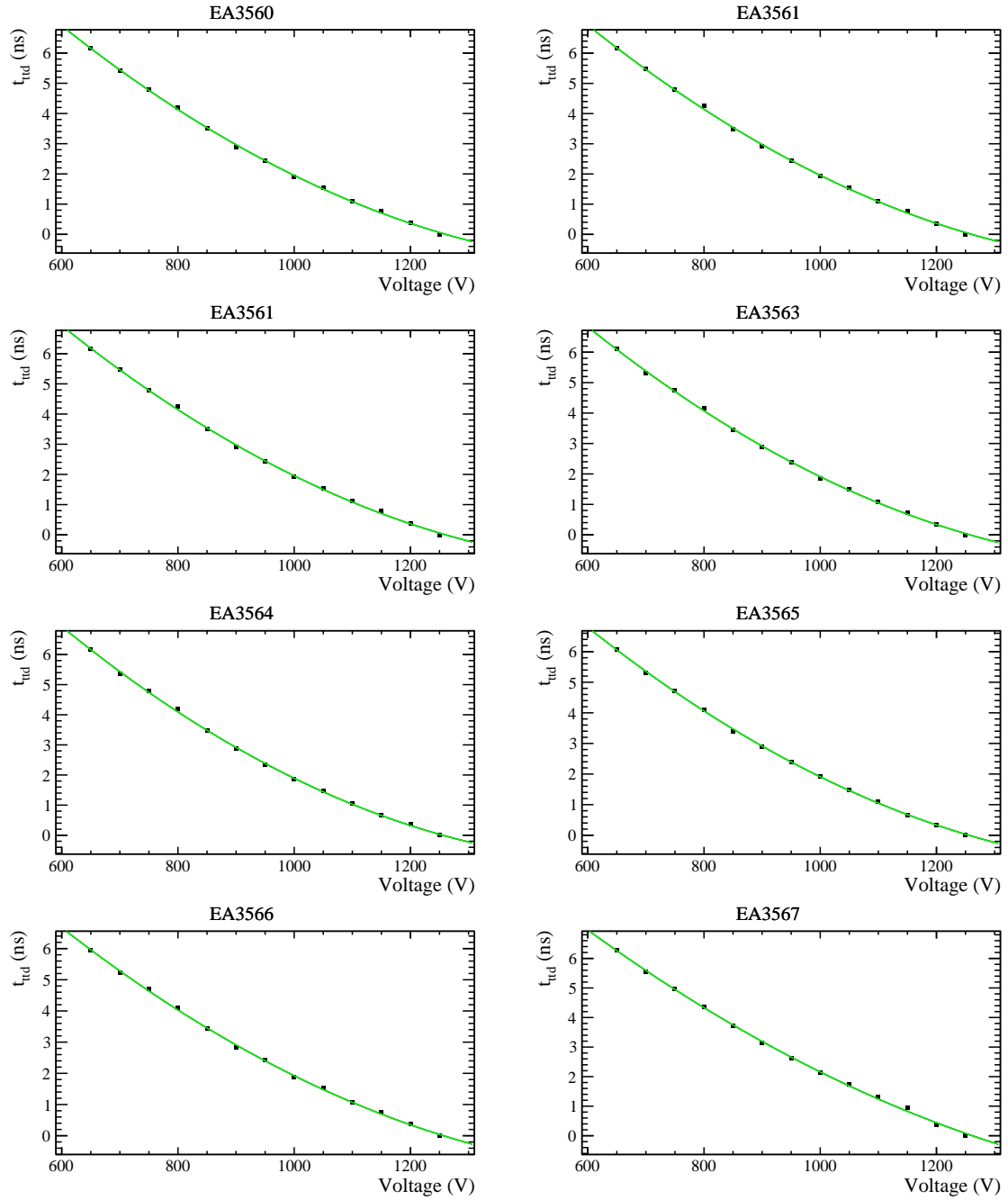
Figure 3.15: t_{ttd} vs voltage graphs of the PMTs from EA3560 to EA3567 characterized in Bologna. The black points are the t_{ttd} obtained from the Eq. 3.13. The green line is the theoretical expectation expressed in Eq. 3.9.
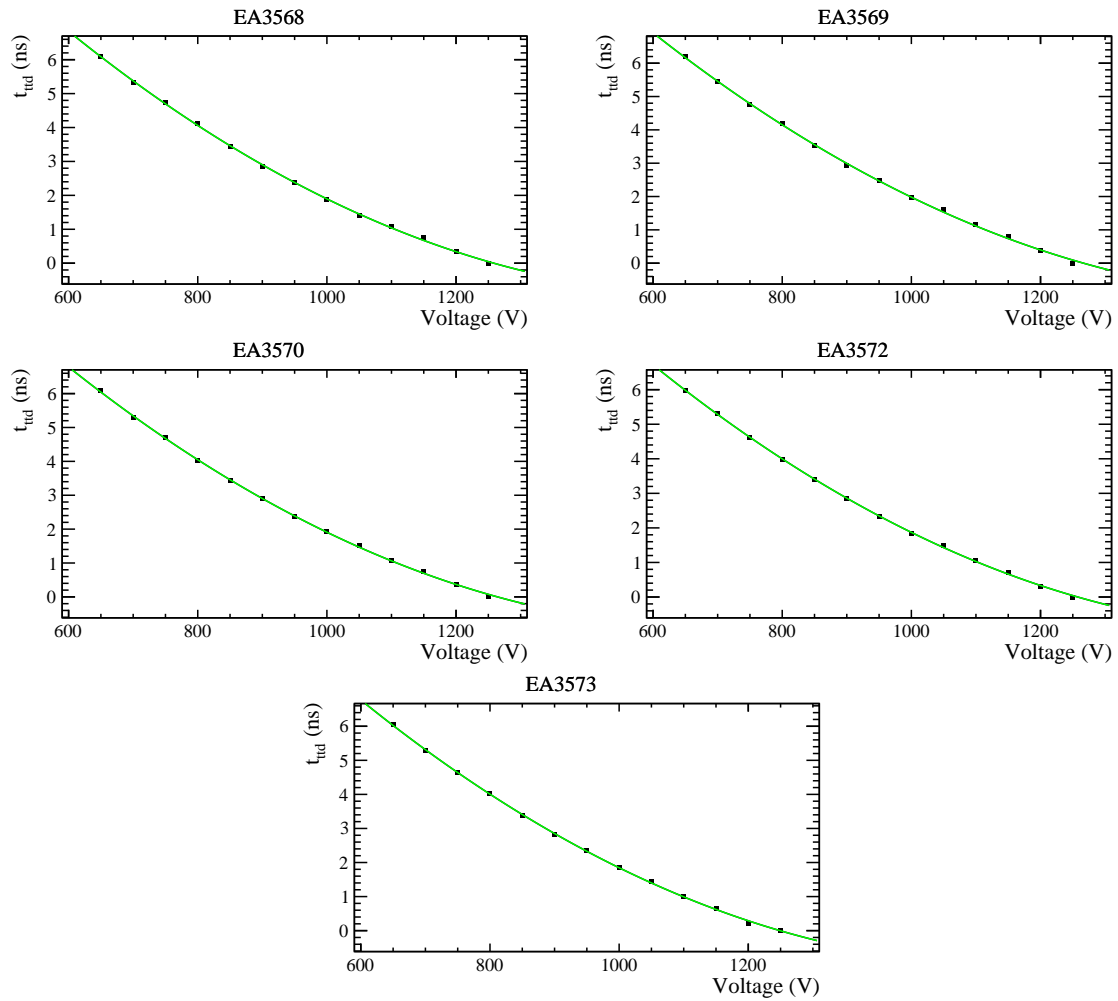
Figure 3.16: t_{ttd} vs voltage graphs of the PMTs from EA3568 to EA3573 (EA3571 is missing) characterized in Bologna. The black points are the t_{ttd} obtained from the Eq. 3.13. The green line is the theoretical expectation expressed in Eq. 3.9.

60
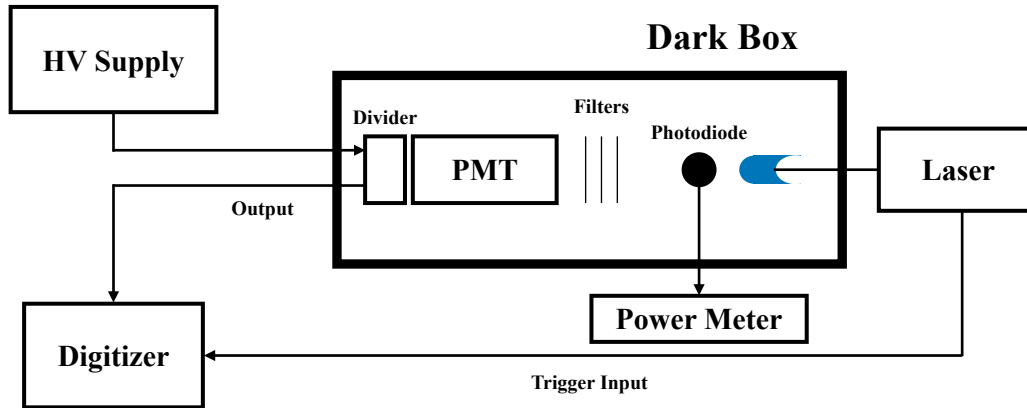
Figure 3.17: Scheme of the experimental setup used for the linearity measurements.

The saturation of the charge is due to the high electron density in the region of the last two dynodes. Hence, by increasing the voltage, and so the gain, the linearity would be worst. In order to explore this possible behaviour, the linearity will be investigated for two values of the power supply.

3.4.1 Experimental setup

The PMT is placed in the dark box and illuminated with the lasers. For the measurement of the integrated charge, the laser operates in pulsed mode with 500 Hz of repetition rate. Between the laser and the PMT window, two neutral density filters with attenuation factors x16 and x8 are placed. The PMT signal pulse is acquired by the DRS4 EvaluationBoard digitizer. The measurements of the power is performed by a calibrated photodiode by Thorlabs [45] connected to the Console for the Digital Optical Power Meter PM100 of ThorLabs. The photodiode is placed in front of the laser beam for the measurement of power, and removed for the measurements of the signal. The laser operates in continuous mode for the measurement of the power and the two filters are removed in order to measure higher values of the power and reduce the experimental uncertainty. Different configurations of the neutral density filters are added to the two fixed filters in order to decrease the light intensity and consequently the light power and the ν. A scheme of the experimental is shown in Fig. 3.17.

3.4.2 Measurements

The study of the linearity is performed at two different supply voltages: the voltage corresponding to a gain equal to 1.5×10^5 of each PMT and a voltage 400 V higher than that. In this way, a possible dependence of the linearity from the power supply of the

Voltage (V)	Power (nW)	ν	Charge (pC)	Exp. Charge (pC)
	325000 ± 16250	1114 ± 111	12.983 ± 0.649	21.969 ± 1.098
	152000 ± 7600	519 ± 52	7.729 ± 0.386	10.235 ± 0.512
653	73000 ± 3560	250 ± 24	4.299 ± 0.215	4.930 ± 0.246
	29800 ± 1490	102 ± 10	1.966 ± 0.098	2.012 ± 0.101
	13950 ± 698	48 ± 5	0.947 ± 0.047	0.947 ± 0.047
	13950 ± 698	48 ± 5	23.340 ± 1.167	50.036 ± 2.502
	4940 ± 247	17 ± 2	12.540 ± 0.627	17.721 ± 0.886
653+400	2275 ± 113	7.8 ± 0.8	7.024 ± 0.351	8.131 ± 0.407
	1085 ± 54	3.7 ± 0.3	3.696 ± 0.184	3.857 ± 0.192
	857 ± 42	2.9 ± 0.3	3.023 ± 0.151	3.023 ± 0.151

Table 3.3: Measurements of the power and the charge of the PMT EA3566. The values of ν and the expected charge are extracted from Eq. 3.5 and 3.14.

PMT can be studied. For each of the two voltages, five measurements of light power and collected integrated charge are performed, each one with different configurations of the neutral density filters. The attenuation of the light in each step is chosen in such a way as to produce a reduction in power of approximately half of the value of the previous state. The value of the ν is correlated to the value of the light power by Eq. 3.16. Therefore, the values of ν at each steps is extracted by the proportion

$$\nu = \frac{W}{W_0} \nu_0. \tag{3.17}$$

W_0 and ν_0 are the values of the light power and the most probable value taken at well defined condition of the PMT: supply voltage at 1250 V and the rate R close to 0.7. W_0 is measured with the Digital Optical Power Meter as the other powers while ν_0 is directly extracted from the rate, from Eq. 3.5. The value of rate is chosen because corresponds to the value of ν close to 1. Ten thousand measurements of the integrated charge are performed for each point and the mean is computed.

The measurements performed on the PMT EA3566 are presented as example. W_0 and ν_0 are equal to (366 ± 18) nW and 1.251 respectively, the measurements of the light power, ν and integrated charge are presented in Tab. 3.3. The expected charge (Q_{exp}), defined as the charge that one should have if the PMT would be perfectly linear, is reported in the lats column of Tab. 3.3. It is computed following Eq. 3.14, where the values of Q_{low} and ν_{low} are the lowest measured values in each set of five measurements.

The ratio of the measured charge over the expected charge Q/Q_{exp} is computed for all the points in order to see the deviation of the linearity. The graphs of the Q/Q_{exp} vs the measured charge Q of each PMT are presented in Figs. 3.18-3.21. The supply

voltage used for the yellow points is the voltage corresponding to a gain equal to 1.5×10^5 while the supply voltage for the purple points is 400 V higher. All the graphs show an evident decrease of the measured charge compared to the expected charge at high value of light power. As expected, by increasing the light power, or the ν, the collected charge increases and the signal of the PMT is saturated. The decrease of the charge signal is between 30% and 40% with respect to the expected one when an integrated charge of 30 pC is observed. Even a dependence on the power supply is observed. The non-linearity effects are greater when the voltage is higher. This is due to the increasing in the gain which produce an higher charge density at the last dynodes.

3.5 Dark current

The last important characteristic to know for the correct functioning of PLUME is the dark current. For dark current we mean the small amount of current flows in a photomultiplier tube even when it operates in a completely dark state. The main causes producing a dark current in a PMT are described in Section 2.3.5.

There is a dependence of the dark current to the supply voltage, but the rate of increase is not constant.This characteristic can be divided in three region of the supply voltage: low voltage up to 500 V, medium voltage between 500 and 1500 V and high voltage above 1500 V. Depending on the region, the dark current main contribution is different. The low voltage region is dominated by leakage current, medium voltage region by thermionic emission and high voltage region by field emission and electrode support scintillation. In the ideally case, the amount of this current should be kept as small as possible. In general, the medium region provide the best signal-to-noise ratio. The PMT of PLUME will operate near to the 1.5×10^5 gain voltages, measured in the Section 3.2.3. These values are all in the medium region therefore, only the dark current for medium voltages will be measured.

3.5.1 Experimental setup

The tested PMT is placed in the dark box and it is left connected to the power supply at least 1 hours. Storing the PMT in a dark state condition of 1 hours, allows the device to approach the average dark current level. The dark current is a very small quantity, therefore a very precise instruments is required for the acquisition. The measurements are performed with the $5^{1/2}$-digit Model 6485 Picoammeter, by Keithley, that reach a resolution of 10 fA. A scheme of the experimental set up is illustrated in Fig. 3.22.

63
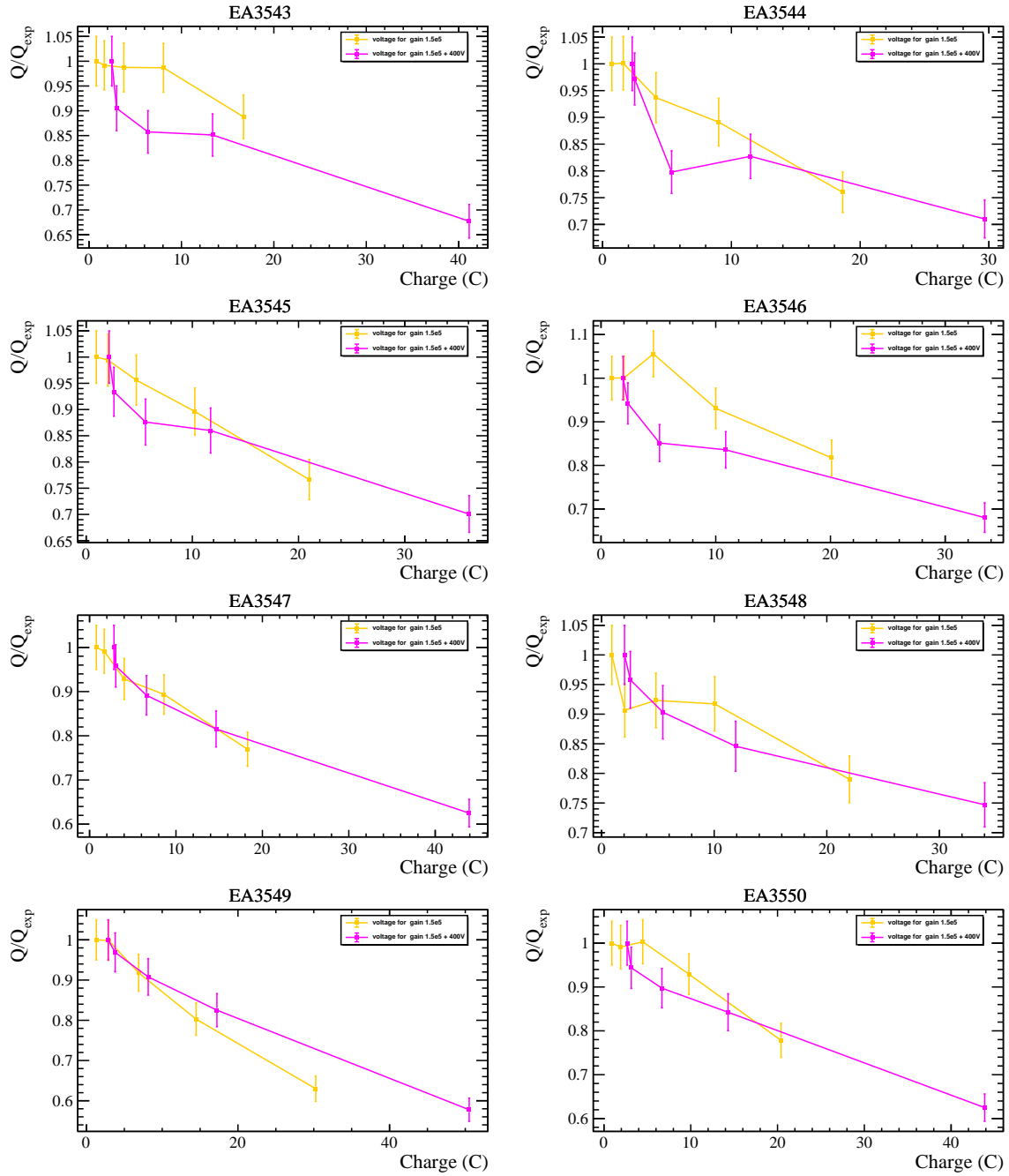
Figure 3.18: Graphs of the linearity of the PMTs from EA3543 to EA3550 characterized in Bologna computed at the voltage corresponding to a gain equal to 1.5×10^5 (yellow points) and a voltage 400 V higher than that (purple points).
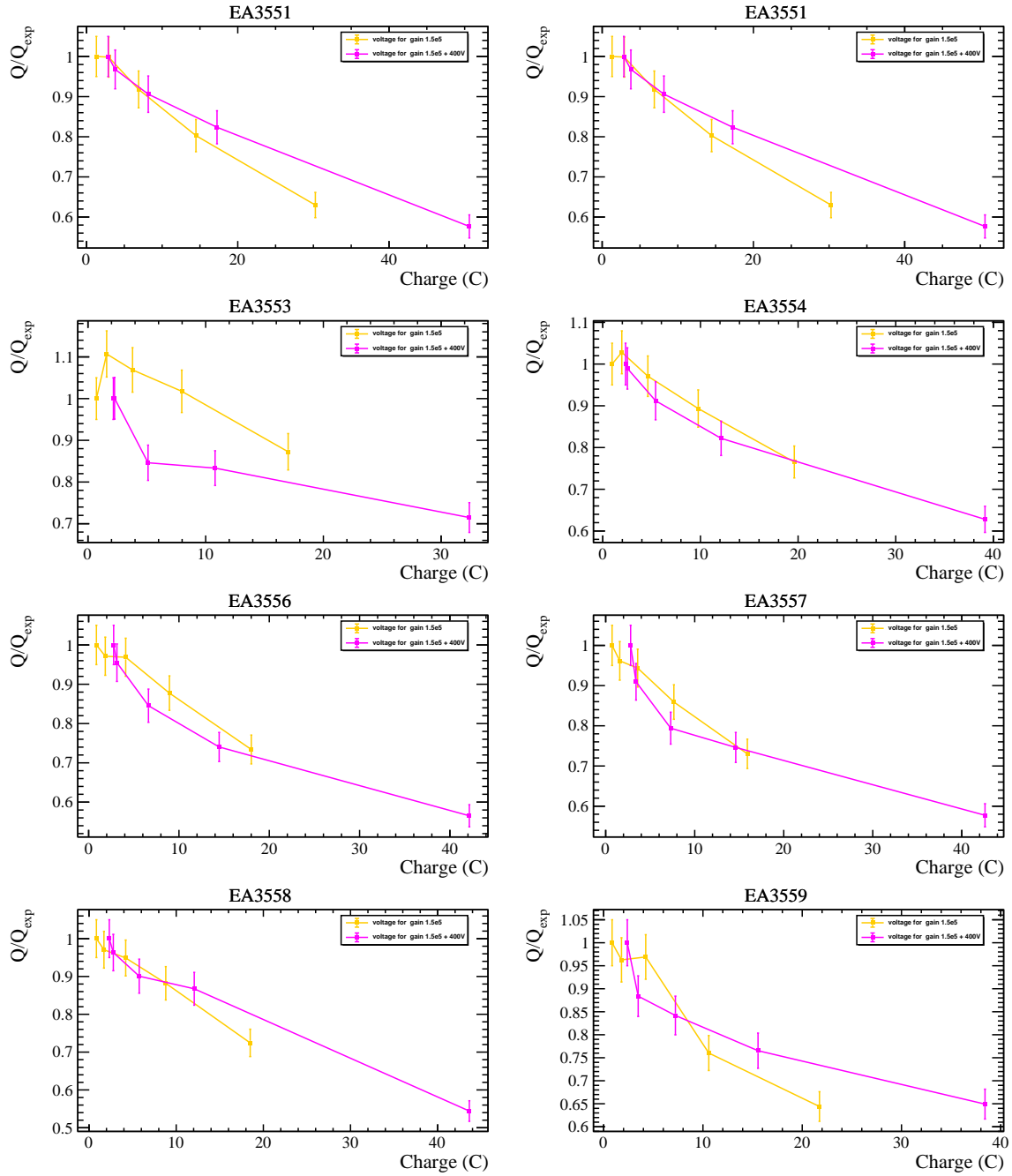
Figure 3.19: Graphs of the linearity of the PMTs from EA3553 to EA3559 (EA3555 is missing) characterized in Bologna computed at the voltage corresponding to a gain equal to 1.5×10^5 (yellow points) and a voltage 400 V higher than that (purple points).
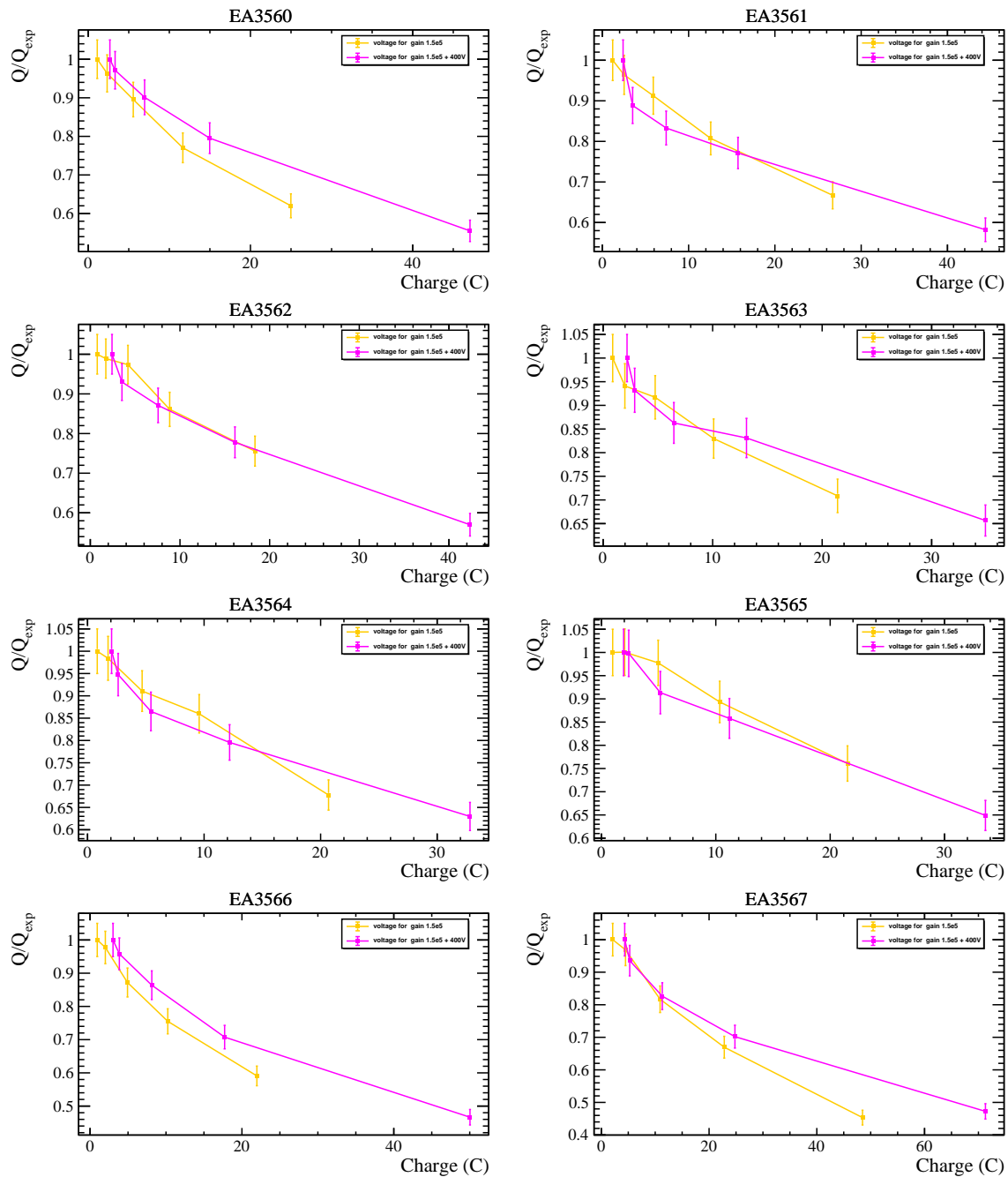
Figure 3.20: Graphs of the linearity of the PMTs from EA3562 to EA3567 characterized in Bologna computed at the voltage corresponding to a gain equal to 1.5×10^5 (yellow points) and a voltage 400 V higher than that (purple points).
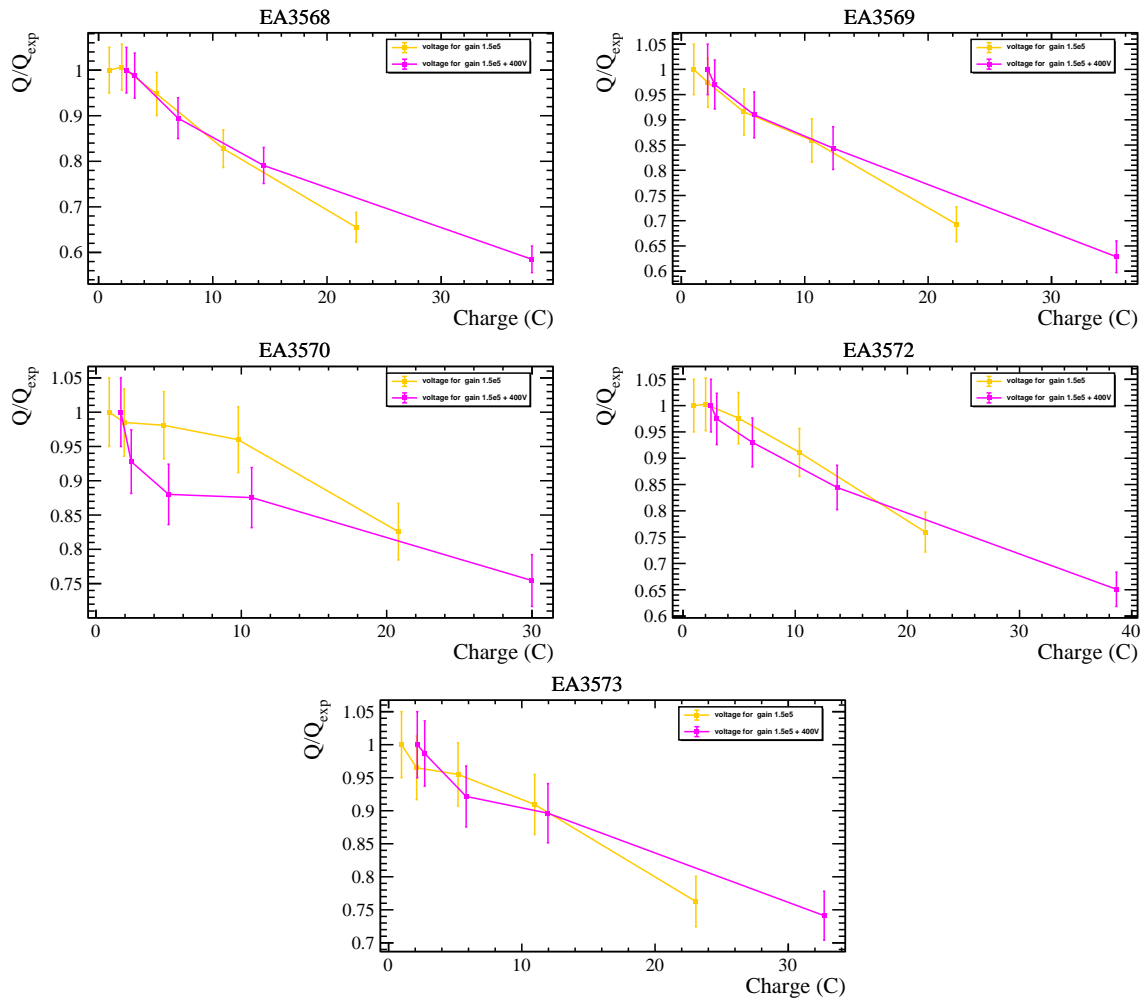
Figure 3.21: Graphs of the linearity of the PMTs from EA3568 to EA3573 (EA3571 is missing) characterized in Bologna computed at the voltage corresponding to a gain equal to 1.5×10^5 (yellow points) and a voltage 400 V higher than that (purple points).
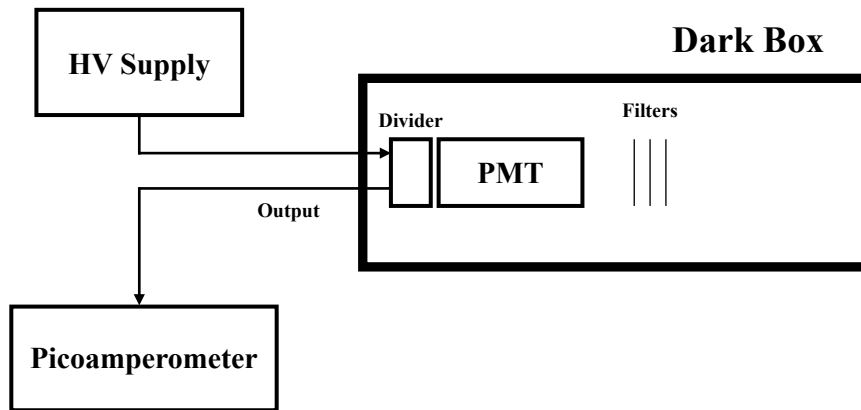
Figure 3.22: Scheme of the experimental setup used for the linearity measurements.

3.5.2 Measurements

The dark currents are measured for all the PMT at 13 fixed values of the supply voltage, in the range 650 - 1250 V. Twenty current measurement are acquired for each voltage step, one each second. The averages of the current measurements as a function of the voltage are shown in Figs. 3.23-3.26. The value of the dark current increases with increasing voltage as expected. The amount of dark current is lower than approximately 10 nA even at the highest value of supply voltage supported by PMT. Therefore, the dark current can be considered negligible respect to the signal current for all the 29 PMT.
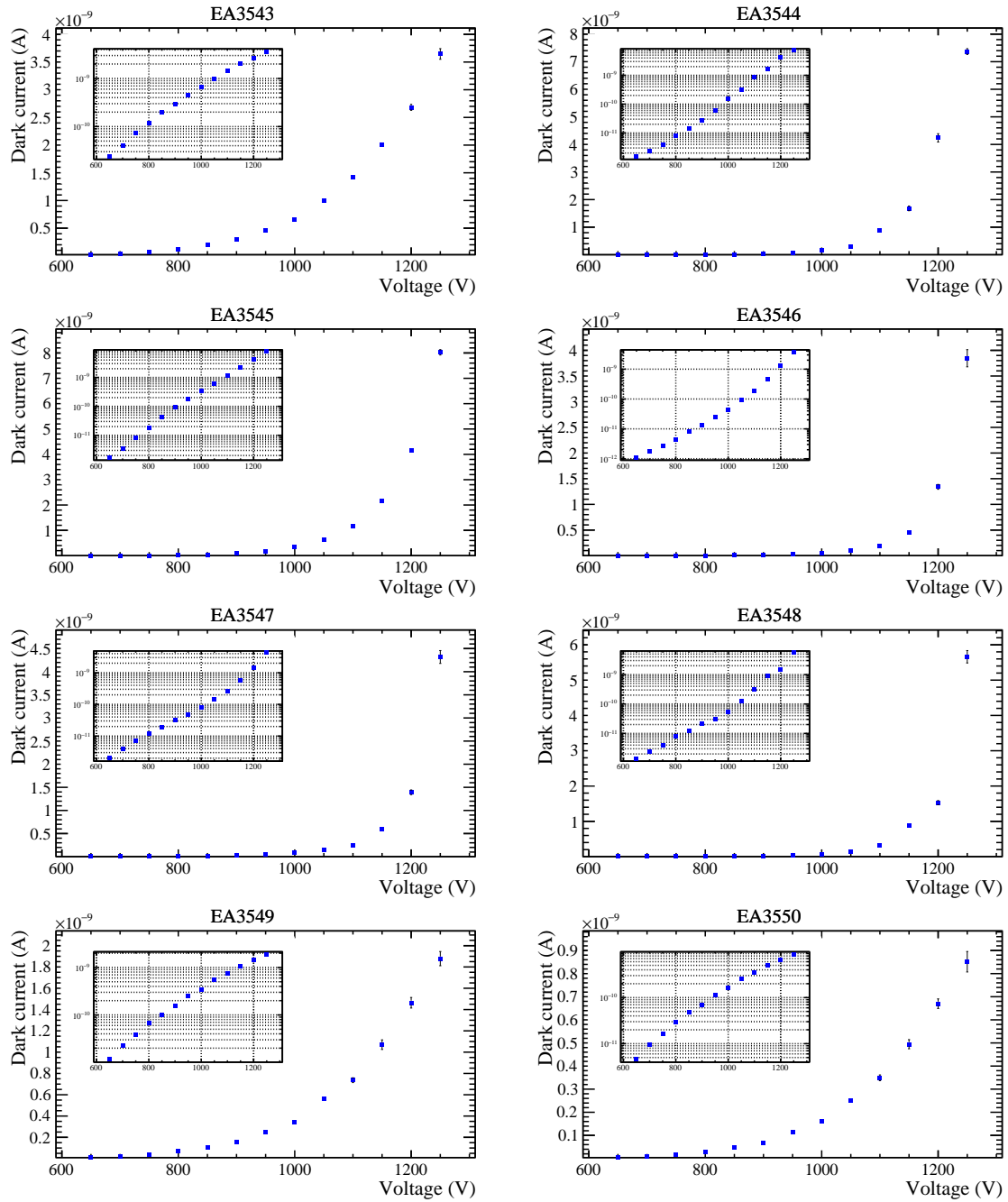
Figure 3.23: Dark current vs voltage graphs of the PMTs from EA3543 to EA3550 characterized in Bologna. The vertical axis of the small window is in logarithmic scale.

69
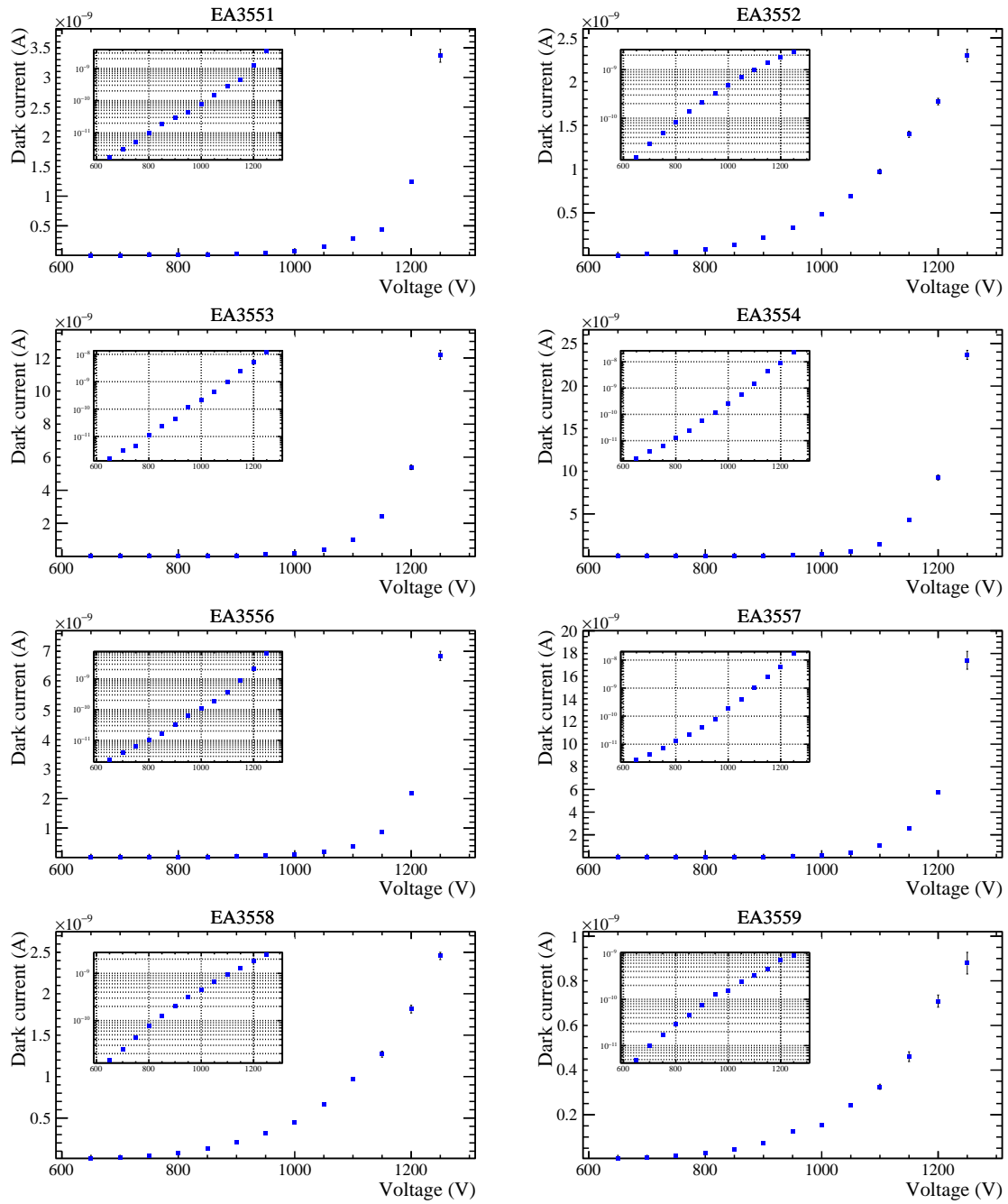
Figure 3.24: Dark current vs voltage graphs of the PMTs from EA3551 to EA3559 (EA3555 is missing) characterized in Bologna. The vertical axis of the small window is in logarithmic scale.

70
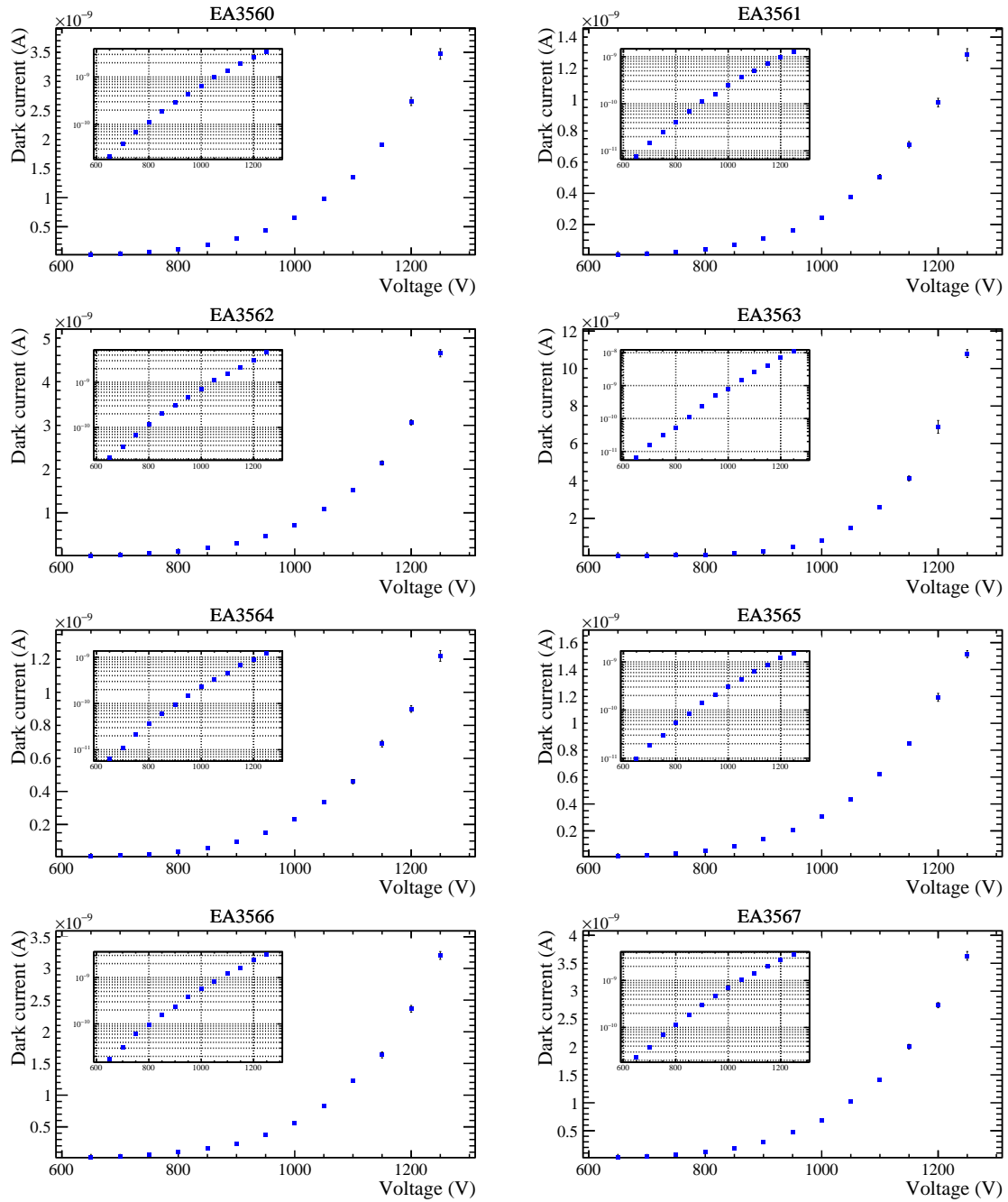
Figure 3.25: Dark current vs voltage graphs of the PMTs from EA3560 to EA3567 characterized in Bologna. The vertical axis of the small window is in logarithmic scale.

71
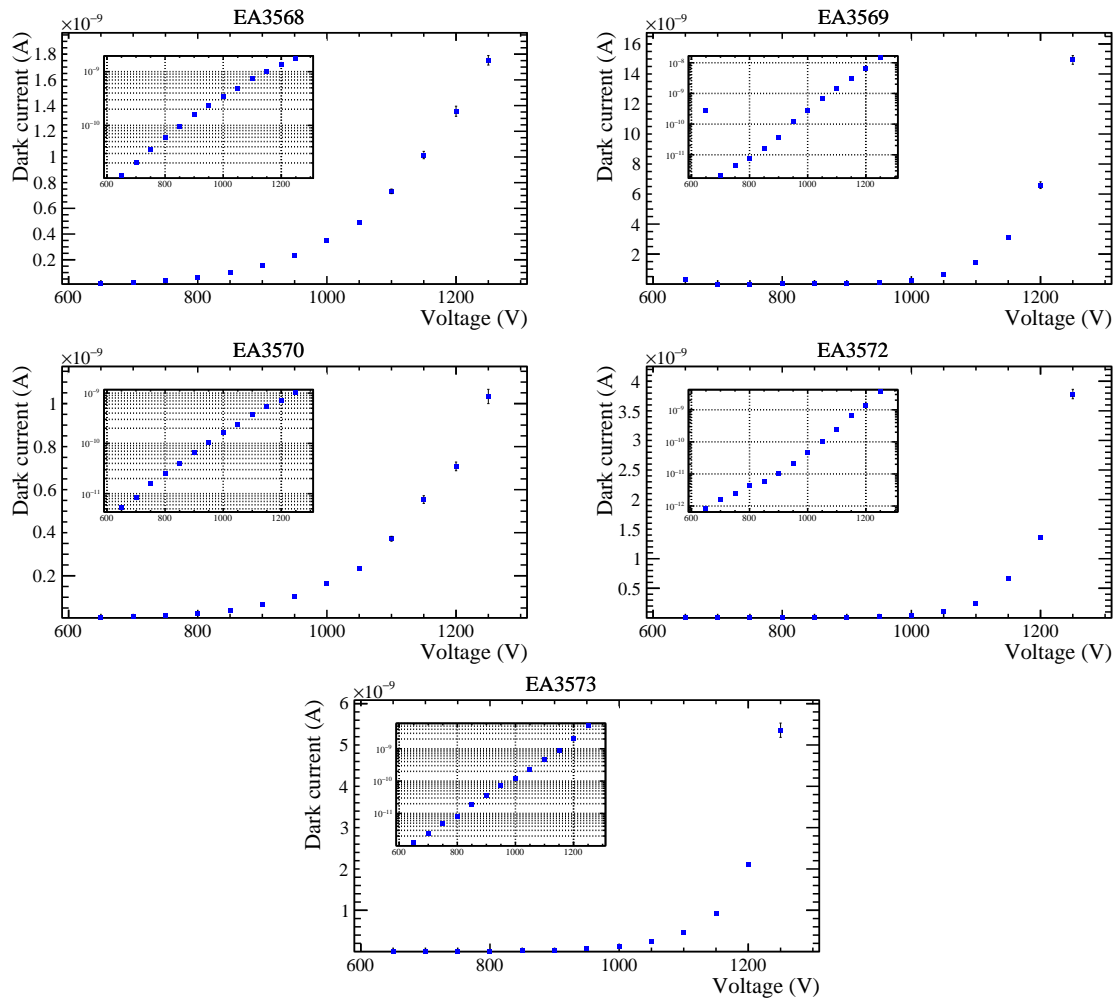
Figure 3.26: Dark current vs voltage graphs of the PMTs from EA3568 to EA3573 (EA3571 is missing) characterized in Bologna. The vertical axis of the small window is in logarithmic scale.

Chapter 4

Dark ring absorber and module testing

The work presented in this Chapter is done with the PLUME group at IJCLab at Orsay. The first part regards the realization of a new component of the elementary detection modules of PLUME, the so-called dark absorbing ring. The second part presents the results of the qualification tests of the 48 modules performed before the installation of PLUME in LHCb.

4.1 Dark absorbing ring

4.1.1 Objective

The LHCb detector has a high track density environment. Due to the extremely high number of produced particles per event, it can happen that some product particles of the primary vertex interact with the beam pipe and the material around the accelerator and create secondary particles. If the number of secondary particles is high enough, there is a probability that two of those create a coincidence in the two-layers of the hodoscope and produce spurious signals. In order to decrease the number of secondaries producing a signal in PLUME, a change had been made to the elementary modules. As it's explained in Section 1.3, the elementary detection module is composed by the PMT, the PMT divider circuit, the quartz tablet, the monitoring fiber and the magnetic shield, all fitted inside an aluminium cylindrical shield.

The SPECTROSIL 2000 tablet works as a radiator for Cherenkov radiation (see Sec. 1.3.3). Therefore, when a charge particle coming from the primary vertex goes through the quartz with a velocity $v > c/n$, n being the refractive index of the quartz, it emits photons with an angle given by $\cos\theta_c = v/(nc)$. Figure 4.1 shows how a particle from primary vertex or from secondary interactions creates Cherenkov light inside the quartz

(a) *Particle from primary vertex*   (b) *Secondary particle*
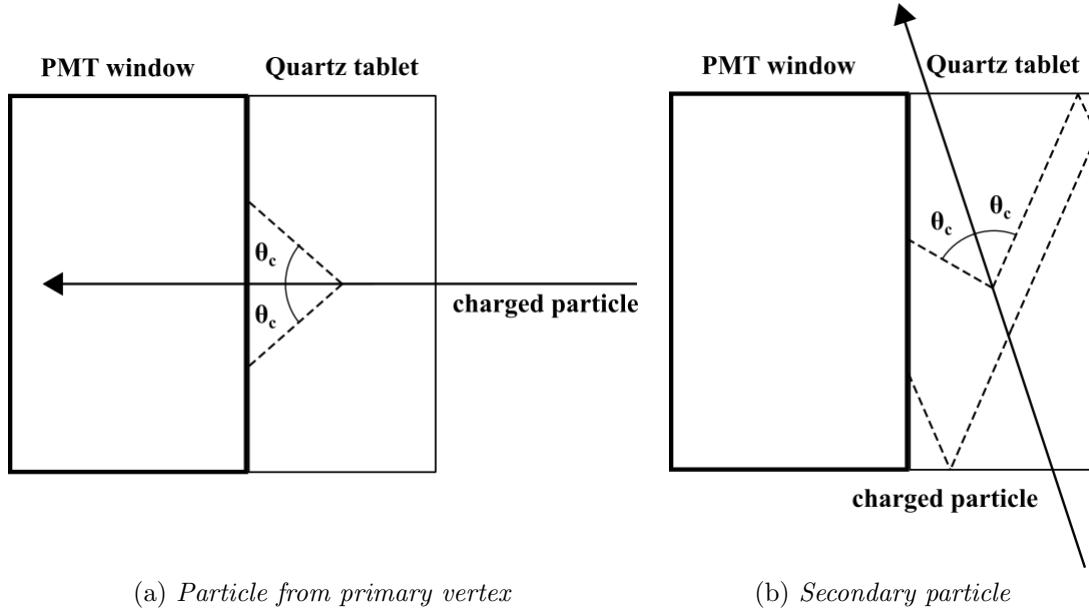
Figure 4.1: Scheme of the emitted Cherenkov light in the quartz tablet. Charged particle coming from the primary vertex (left) and secondary particle (right).

tablet. Once the photons are emitted, they are transmitted from the quartz to the PMT window. Both the PMT window, made with quartz, and the silicon grease TSF451-50M have a refractive index similar to the SPECTROSIL 2000 tablet radiator. Therefore, the photons have a high probability to be transmitted to the PMTs window without any reflection, due to the Snell law

$$n_1 \sin(\theta_1) = n_2 \sin(\theta_2), \tag{4.1}$$

where $n_{1,2}$ and $\theta_{1,2}$ are the refractive index and the angles with respect to the normal of the two medium. The formula to obtain the critical angle for the total internal reflection comes from the Eq. 4.1,

$$\theta_{critic} = \arcsin\left(\frac{n_2}{n_1}\sin(\theta_2)\right) = \arcsin\left(\frac{n_2}{n_1}\right). \tag{4.2}$$

The refracting index of the SPECTROSIL 2000 $n(\lambda)$ has a value between 1.455 and 1.575 [46] for wavelengths corresponding to visible and ultraviolet light, respectively. The refractive index of air n_{air} is equal to 1. Because of the large difference between these two refractive indices, the value of the critical angle computed with the Eq. 4.2. is in the range of 39.4°-43.4°. Therefore, a photon which hits the lateral surface of the quartz is reflected until it reach the window and is transmitted to the PMT. As the quartz crystal is a cylinder its surfaces are not flat. Because of this, the computation of the critical angle is quite more complicated and Geant4 [13] simulations are needed.
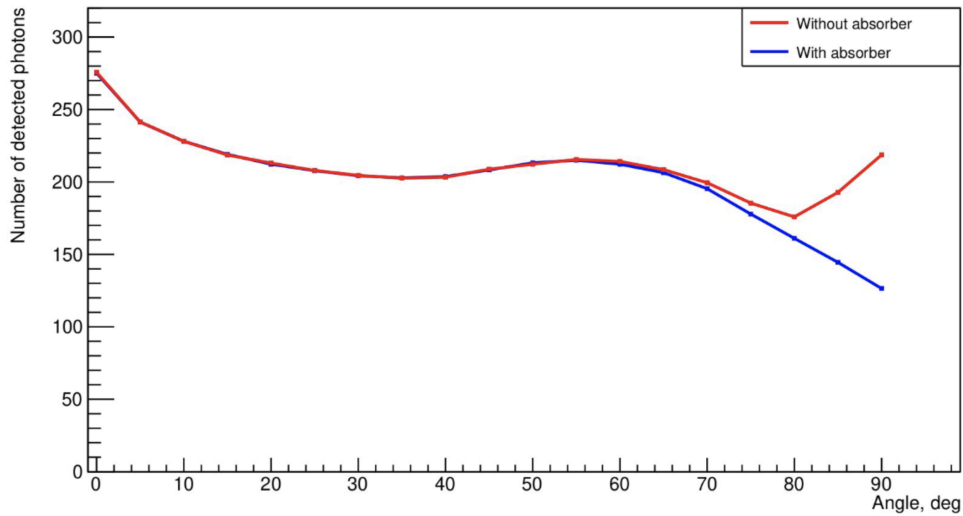
Figure 4.2: .
Geant4 simulation of the number of photons detected in function of the incident angle, in test conditions with a Gaussian beam ($\sigma = 7$ mm) [47]. The red points are simulated without the dark aluminium ring absorber; the blue points are simulated with the dark aluminium ring absorber.
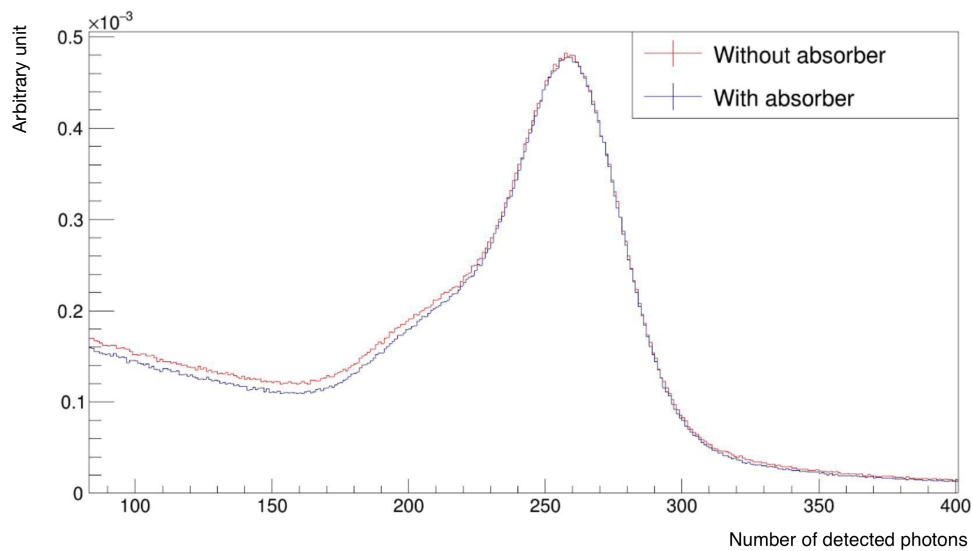
Figure 4.3: Geant4 simulation of the distribution number of photons collected [47]. The red histogram is simulated without the dark aluminium ring absorber; the blue histogram is simulated with the dark aluminium ring absorber.
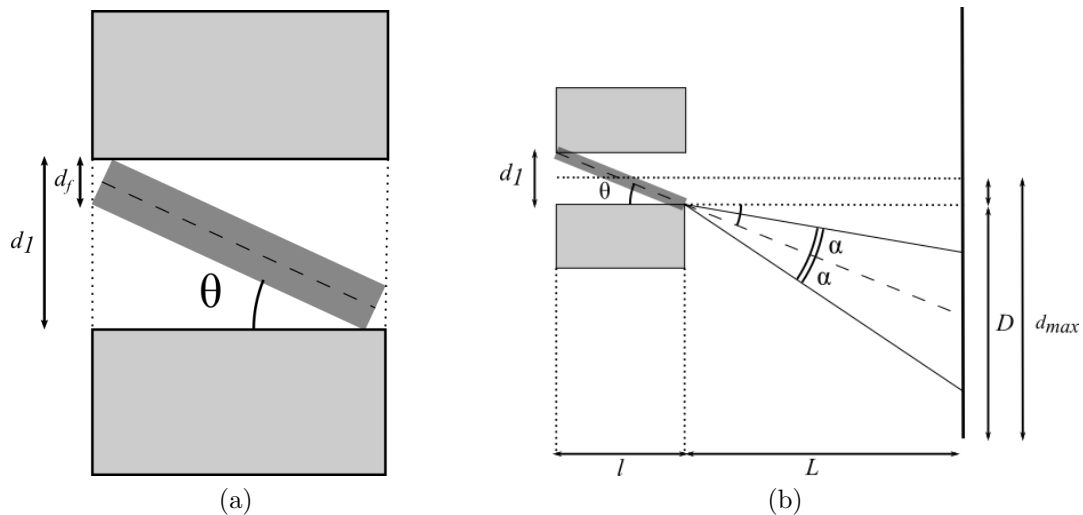
Figure 4.4: Geometry of the interface fiber-quartz. The dark grey bar is the optic fiber, passing inside the SMA connector, the light grey rectangles. The length L is the distance between the end of the fiber and the quartz surface.

Secondary particles, due to their origin point, cross the quartz tablet with a large angle with respect to the main surface and about half of the Cherenkov light cone is reflected over the quartz, as can be seen in the right part of Fig. 4.1. A possible solution to decrease the background coming from secondaries is to add a dark aluminium ring to the surface of the quartz opposite to the PMT which works as an absorber. In this way the right half of Cherenkov light is absorbed by the dark ring before it produces signal in the PMT. The remaining light, the left half, is not enough to exceed the charge threshold of the front-end readout electronics. Therefore secondary particles are not considered as event in the logZero computation.

According to simulation, the presence of the absorber does not affect the number of detected photons produced by primary particles. In Fig 4.2 [47] the number of detected photons for different angles of the the particle trajectory with respect to the normal to the quartz surface is shown. The difference between the number of photons detected without the absorber (red points), and with the absorber (blue points), is obvious only for large angles, $> 65°$, so only for the secondary particles. The histogram of the signal and background is presented in Fig 4.3 [47]. The background is reduced while the peak of the signal does not change with the dark ring absorber.

4.1.2 Realization and mounting

The ring was built with the same diameter of the quartz tablet, $d = 10\,mm$, in order to cover as much surface as possible. Because of the optic fiber of the monitoring system,

it is not possible to use a full disk, otherwise the light from the optic fiber would not reach the PMT window. Therefore, the diameter of the hole must be small to absorb as much reflected light as possible but large enough to allow the passage of most of the light coming from the monitoring system. The maximum dispersion of light on the surface of the quartz can be computed considering the geometry of the interface between the fiber and the quartz and the numerical aperture NA of the fiber. This last quantity is defined as the sine of the largest angle an incident ray can have for total internal reflectance in the core,

$$NA = \sin\alpha = \sqrt{n_1^2 - n_2^2}, \tag{4.3}$$

where n_1 and n_2 are the refractive index of the core of the fiber and the cladding respectively. The optic fiber FBP100 from Polymicro has $NA = 0.22$. The diameter of the fiber is $d_f = 0.14$ mm and the final cavity in which the fiber ends is $l = 1$ mm long and has a diameter of $d_1 = 0.4$ mm. Assuming the fiber as a rigid object, the maximum angle of deviation of the fiber respect to the main axis will be approximatively $\theta = \arctan\left(\frac{d_1 - d_f}{l}\right)$, Fig 4.4a. Considering the distance between the end of the fiber and the surface of the quartz, $L = 2$ mm, the maximum dispersion of light on the surface of the quartz will be

$$
\begin{aligned}
d_{max} &= 2\left(\frac{d_1}{2} + D\right) = 2\left(\frac{d_1}{2} + L\tan(\theta + \arcsin\alpha)\right) \\
&= 2\left(\frac{d_1}{2} + L\tan\left(\arctan\left(\frac{d_1 - d_f}{l}\right) + \arcsin\alpha\right)\right) = 2.46 \text{ mm.}
\end{aligned}
\tag{4.4}
$$

In order to make the computation easier to understand, the visual geometrical construction of the computation is reported in Fig 4.4b. From the previous calculation, the area covered by the light of the monitoring system should not exceed a circle with a diameter of 2.46 mm, assuming the light producing a cone out of the fiber. Therefore, the chosen dimension of the diameter of the hole at the middle of the aluminium dark ring is 3 mm.

Two options were considered for the type of material used for the ring: black painted aluminium and black paper scotch tape. Even for the gluing material there were two possibilities, using the TSF451-50M grease [14], the same used to fix the quartz to the PMT window, or a glue solution of KE-103 and CAT-103 (100:5) [48]. The best solution from the application tests was the aluminium with the grease. The ring of aluminium is flatter and easier to fix on the quartz with a good precision while the TSF451-50M grease produced less air bubbles between the two surfaces and is more homogeneous.

4.1.3 Measurements of signal decrease

In order to study the possible decrease of current signal of the PMT after the application of the dark aluminium ring, different tests were performed with the same optic fibers
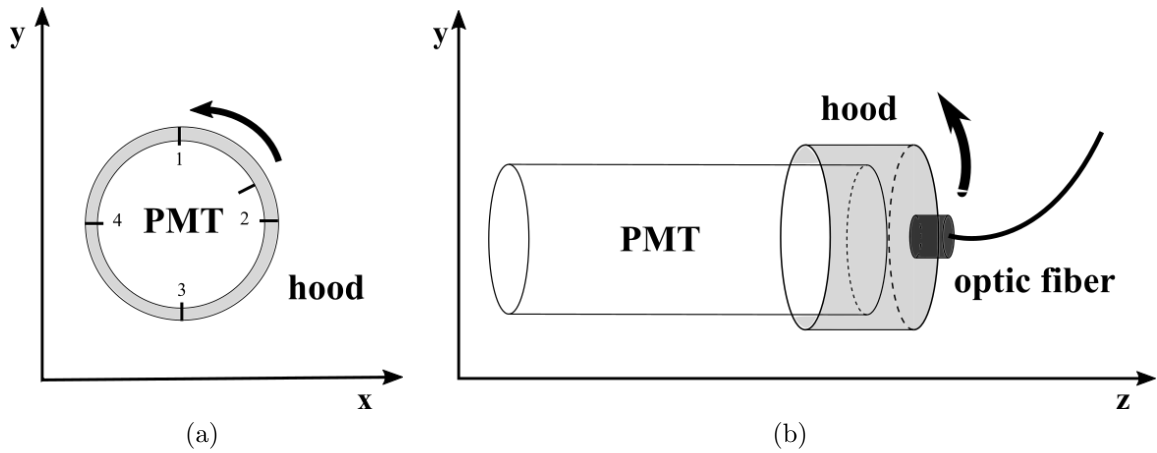
Figure 4.5: Scheme of the connection of the PMT with the plastic hood and the optic fiber in the plane x-y, Fig (a), and z-y, Fig (b).

used in the monitoring system (see Section 1.6). The source of light is a Picosecond Injection Laser (PiLas) with a wavelenght of 468 nm [49]. The frequency of the laser was set to 200 kHz in order to have a large amount of current in the output signal. The light was transmitted from the laser to the quartz in front of the PMT window by an optic fiber with a SMA connector connected to an light attenuator. The end of the fiber was connected to the hood of the PLUME module. The current was measured with a Keithley 2612 Dual-channel System SourceMeter Instrument (200V), with a programming resolution of 20 pA [50]. For each measurement the PMT with serial number EA3580 was used as control (1.5×10^5 gain at 796 V). The HV was set to the value of voltage at which the gain of the PMT is equal to 1.5×10^5. The dark current had been checked to be 0.1% of the output signal so negligible. Four measurements were performed for each tests, corresponding to four rotation positions of the hood fixed to the extremity of the fiber (Fig. 4.5). In this way, the average signal could be computed as well as the position dependence. From the position dependence, we were able to get information about how well the ring was centered with respect to the quartz tablet and the presence of impurities.

Test 1: 2 mm hole

In the first test, a ring with a 2 mm diameter hole was applied to the quartz of the EA3573 module. According to the characterization, the gain of the PMT reaches a value of 1.5×10^5 for an input voltage of 806 V. The fiber used for this test was an optical fiber prototype with SMA connector, like those used for the monitoring system of PLUME. Eight measurements of the output current were performed, four with the ring and four without. The values of the current are reported in Tab. 4.1. The variation between the

78

EA3573		EA3580
Without the Ring (nA)	**With the Ring (nA)**	**Control (nA)**
600.10 ± 0.24	461.00 ± 0.32	609.04 ± 0.13
598.43 ± 0.32	452.87 ± 1.41	608.12 ± 0.28
598.23 ± 0.86	474.51 ± 1.78	608.43 ± 0.21
597.45 ± 0.87	451.45 ± 1.03	608.42 ± 0.24
598.55 ± 0.32	459.95 ± 0.63	608.46 ± 0.44

Table 4.1: Measurements of the output current of the PMT EA3573 with and without the dark aluminium ring (2 mm), first and second columns. Control measurements, third column. In the last row, the means of the respective columns are computed.

highest and the lowest current values of the control column is smaller than the 0.15% of the mean of the control measurements. The difference of signal between the position with the highest current and the position with the lower registered current is only $\sim 2\%$. It's possible that some impurities are present on the hole. In the next tests, the surface of all the quartz were cleaned with alcohol before and after the application of the absorber. In this way both impurities and excess grease were removed. Comparing the two columns of the PMT EA3573 we clearly observe a decrease of the signal with the dark aluminium ring with a 2 mm hole is applied on the surface of the quartz. The mean of the signal with the ring is 23% smaller than the mean of the signal without the ring. According to the computations of Section 4.1.2, if the light is distributed homogeneously, the decrease should be 20%. Therefore a 2 mm diameter hole is not enough to allow the passage of the monitoring system light. In the next test the measurement was repeated with an aluminium ring with a diameter of 3 mm.

Test 1: 3 mm hole

The procedure was the same as in the previous test. The signal current decrease due to the aluminium ring with 3 mm hole is measured for two PMTs: EA3573 and EA3556, with 1.5×10^5 gain at a voltage of 740 V and 806 V. This test was done with different optical fibers, taken from those that would then be used in PLUME, in order to be sure that the signal decrease is not caused by a defective fiber. Because of all the PMTs work at the same gain (1.5×10^5), the current signals of the PMTs without the ring absorber are almost equal to the signal of the control PMT EA3580. Therefore, in order to speed up the process, the decrease of signal was compared directly with the signal of the control PMT. The values of the current for different combination of fibers and PMTs

Fiber number	EA3556		EA3580	
	Current (nA)	Mean (nA)	Current (nA)	Mean (nA)
01	528.17 ± 1.32 538.42 ± 1.53 517.55 ± 1.05 519.40 ± 1.26	525.89 ± 0.65	560.34 ± 0.17 561.56 ± 0.15 561.57 ± 0.18 559.96 ± 0.24	560.85 ± 0.09
03	557.03 ± 0.23 556.76 ± 0.65 553.23 ± 0.68 553.44 ± 0.30	555.12 ± 0.25	580.13 ± 0.13 580.56 ± 0.15 580.22 ± 0.15 580.42 ± 0.15	580.33 ± 0.07
06	550.31 ± 1.04 543.89 ± 1.84 532.53 ± 0.89 534.18 ± 1.36	540.23 ± 0.66	567.11 ± 0.13 568.80 ± 0.28 569.24 ± 0.21 570.04 ± 0.24	568.80 ± 0.11

Table 4.2: Measurements of the output current of the PMT EA3556 with the dark aluminium ring (3 mm) and Control measurements (PMT EA3580), taken with the optic fiber 01, 03 and 06.

are reported in Tabs. 4.2 and 4.3.

The variation of control current and the dependence on the position were obtained by computing the total range of the four values and normalized with the averages. The signal decrease is the deviation between the mean of the control current and the mean or the signal current normalized with the mean of the control current. The results of the test are reported in Tab. 4.4

The variation of the control current is stable in all the set of measurements. The signal decrease is in the range of (4-9)%. With the application of a 3 mm hole dark aluminium ring we obtained an improvement of the signal of (14-19)% with respect to the 2 mm hole. A small decrease of signal with respect to the control PMT was still present. A possible cause could be the residues of grease in the hole of the ring that remained after the application. The variation of the signal depending on the four position of the hood is in the range (0.5-4)%.

From this, test the use of a dark aluminium ring with a 3 mm hole in the center turned out to be the best choice. The correct application of the ring for each modules was checked in the qualification tests.

Fiber number	EA3573		EA3580	
	Current (nA)	Mean (nA)	Current (nA)	Mean (nA)
06	468.41 ± 1.03 472.69 ± 1.07 473.37 ± 1.09 476.78 ± 0.62	472.31 ± 0.49	518.60 ± 0.12 518.56 ± 0.14 519.46 ± 0.15 519.19 ± 0.11	518.95 ± 0.10
41	453.22 ± 1.11 455.15 ± 0.45 458.14 ± 0.97 455.96 ± 0.70	455.61 ± 0.42	498.06 ± 0.20 498.65 ± 0.13 498.71 ± 0.18 499.37 ± 0.21	498.70 ± 0.09

Table 4.3: Measurements of the output current of the PMT EA3573 with the dark aluminium ring (3 mm) and Control measurements (PMT EA3580), taken with the optic fiber 06 and 41.

PMT-Fiber	Control Var. %	Signal Dec. %	Position Var. %
EA3556-01	0.29	6.24	3.97
EA3556-03	0.07	4.35	0.68
EA3556-06	0.52	5.02	3.29
EA3573-06	0.17	8.99	0.44
EA3573-41	0.26	8.64	1.08

Table 4.4: Results of the tests performed on PMTs EA3556 and EA3573 with 3 mm hole absorber. From left to right, the columns are the serial number of the PMT and the number of optic fiber used, the variation of the control measurement with respect to its average, the decrease of the signal with respect to the control and the variation of the signal current with respect to the average. All the results are reported in percent.
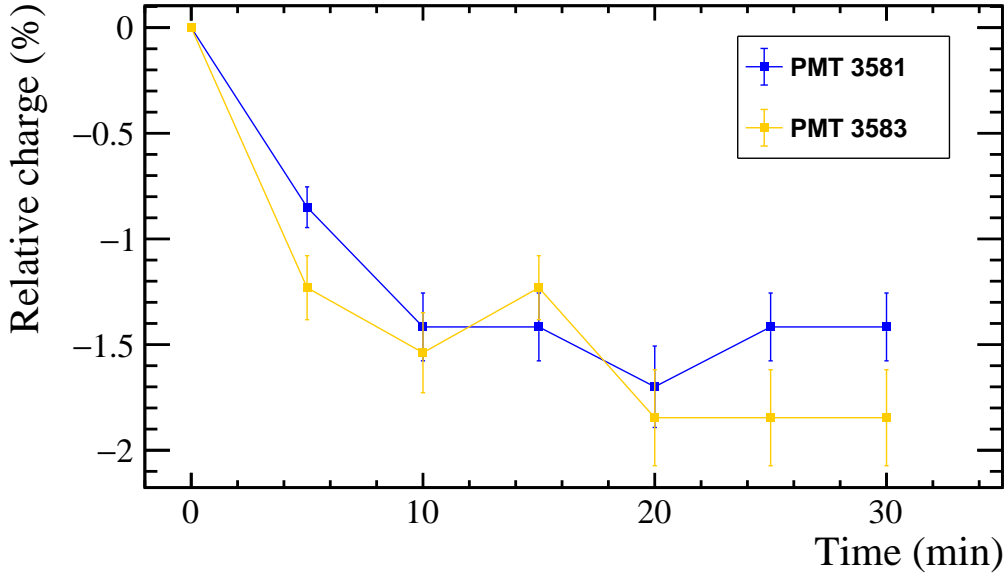
Figure 4.6: Relative variation of the integrated charge signal of PMTs 3581 (blue points) and 3583 (yellow points) with respect to time when the PMT was biased. The decrease is relative to the integrated charge registered at the starting time. A stable condition is achieved already after 10 minutes of operation.

4.2 Qualification tests

The 48 modules composing the hodoscope of PLUME were installed in the two cross-shaped aluminium structures at the end of November. The precise positioning of the modules in the mechanical supporting structure was performed at IJC lab. In order to test the correct operation of the assembled modules (PMT, quartz tablet, dark aluminium absorber ring and optic fiber) the integrated signal of each module was measured at a voltage corresponding to the gain 1.5×10^5. The tests were performed before and after the installation in the aluminium structures of PLUME (PLUME box).

Before the qualification tests, the heating time (time required for the PMT to stabilize) of the PMTs was measured. Seven measurements of the integrated charge of two control PMT (3581 and 3583), lighted by a LED source, were taken every 5 minutes for 30 minutes. The Fig 4.6 shows how the integrated charge changes in time, after the HV was powered on ($t = 0$). The charge variation is relative to the integrated charge registered at the starting time. In the first 10 minutes, the charged collected by the PMT decreases by $(1.4 \pm 0.2)\%$. This can be caused by a decreasing of the gain due to the warming of the dynodes and the resistors in the divider. Another cause can be the changing of the secondaries emission of the cathode with the temperature variation. In the following 20 minutes the signal decreases only by $(0.2 \pm 0.1)\%$. Therefore a stable
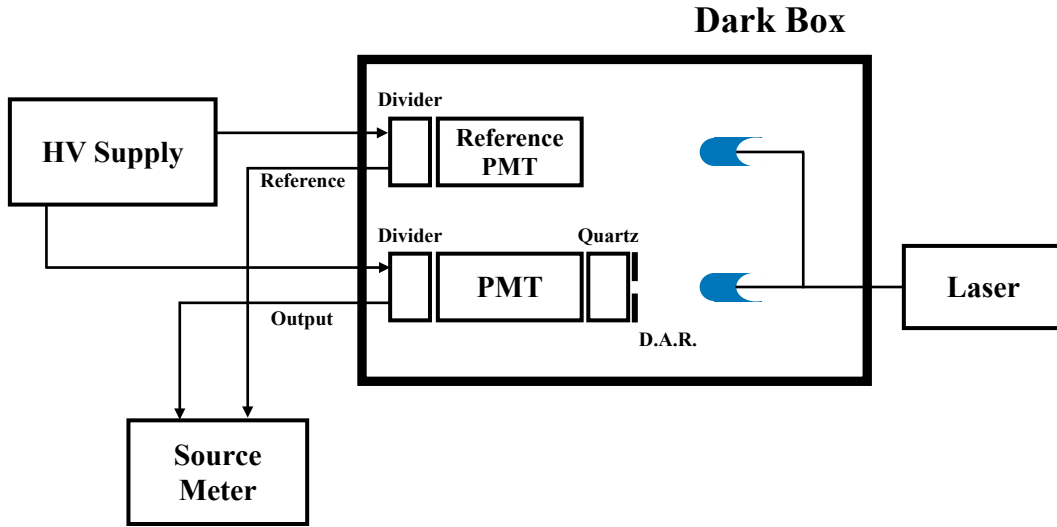
Figure 4.7: Scheme of the experimental setup used for the qualification test performed in the dark box, with directly impinging light. D.A.R is the dark absorbing ring fixed to quartz tablet.

operation of the PMT is achieved after 10 minutes. In order to obtain more precise results each measurement was taken at least 10 minutes after the power-up.

4.2.1 Qualification test in the dark box

The first tests were performed in the laboratory of optic of IJCLab. The source of light is the PiLas with a wavelenght of 468 nm, a repetition rate of 200 kHz and the signal current is measured with a Keithley 2612 Dual-channel System SourceMeter. For each module, 10 measurements of the current were taken in 5 seconds, with an acquisition window of 500 ns. The signal current was then extracted by the mean of the ten measurements. Knowing the repetition of the laser, the mean of the integrated charge can be computed with the relation

$$Q = \nu_{laser} \times I, \tag{4.5}$$

where the ν_{laser} is the repetition rate of laser and I is the mean of the measured currents. In order to check the effect on the signal of the transmission in the optic fiber, two measurements were performed, with and without the optic fiber.

Direct light

The module is positioned inside the black bench and the light of the laser is impinging directly on the quartz tablet. The laser is splitted in two perpendicular beams, one
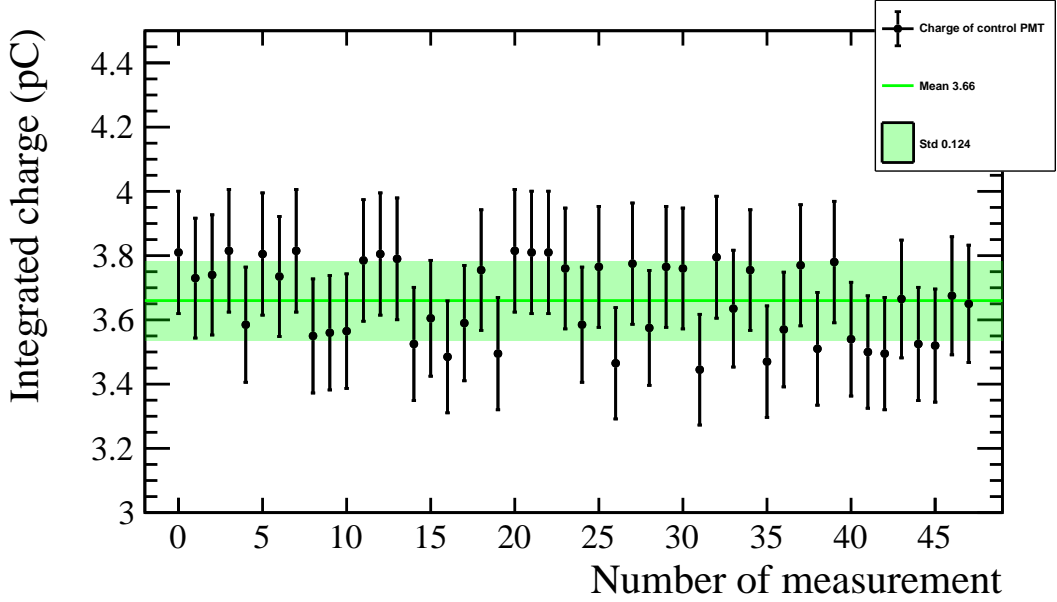
Figure 4.8: Values of the integrated charge of the reference PMT HAMAMATSU R9880U-20. The green line is the mean of the measurements and the red band is the 1σ interval.

directed to the module and the other directed to a reference PMT, R9880U-20 of Hamamatsu [51]. The HV of the reference is set to 440 V in order to have a signal close to 3 pC as for the PLUME modules. A schematic view of the setup used for this qualification test is illustrated in Fig. 4.7.

Using the measurement of the integrated charge of the reference PMT, the variation of the laser beam can be computed. The distribution of the integrated charge of the reference PMT is shown in Fig. 4.8. The standard deviation of the laser is $\sigma_{laser} = 0.124$ pC. In light of this result, the error associated to the measurements of the integrated charge, when PMT is directly impinged by the laser light, can be estimated by using the formula of the standard deviation for sum of normally distributed random variables. The standard deviation of each measurement results to be equal to

$$\sigma_{measure} = \sqrt{\sigma_{gain}^2 + \sigma_{laser}^2 + \sigma_{heating}^2 + \sigma_{bsi}^2} \approx 10\% \qquad (4.6)$$

of the value of the measurement. Therefore, the $\sigma_{measure}$ takes into account the σ_{gain}, error from the estimation of the gain value, the variation of the source of light σ_{laser}, the variation of signal due to the heating time of the PMT $\sigma_{heating}$, which is negligible, and the σ_{bsi}^2 coming from the blue sensitivity index of the PMTs. Blue sensitivity index is the photoelectric current generated from the photocathode when a blue filter (CS 5-58) is interposed in the same measurement system used to measure cathode luminous

Module Number	PMT Serial Number	Mean Integrated Charge (pC)	Std Dev (pC)
00	EA3573	3.89	0.39
01	EA3556	4.63	0.46
02	EA3540	4.96	0.50
03	EA3541	4.15	0.41
04	EA3542	4.44	0.44
05	EA3543	3.38	0.34
06	EA3534	4.66	0.47
07	EA3549	3.91	0.39
08	EA3535	4.37	0.44
09	EA3544	3.55	0.36
10	EA3539	3.97	0.40
11	EA3553	3.54	0.35
12	EA3572	3.59	0.36
13	EA3568	4.31	0.43
14	EA3570	3.94	0.39
15	EA3569	3.79	0.38
16	EA3562	3.11	0.31
17	EA3561	4.04	0.40
18	EA3567	3.37	0.34
19	EA3563	3.78	0.38
20	EA3552	3.40	0.34
21	EA3538	4.53	0.45
22	EA3566	3.25	0.33
23	EA3527	4.44	0.44

Table 4.5: Means and standards deviation of the integrated charge of the modules from 00 to 23 measured with the light of the laser directly impinging on the quartz tablet.

Module Number	PMT Serial Number	Mean Integrated Charge (pC)	Std Dev (pC)
24	EA3545	3.98	0.40
25	EA3526	4.22	0.42
26	EA3532	4.57	0.46
27	EA3536	4.36	0.44
28	EA3524	4.60	0.46
29	EA3528	4.74	0.47
30	EA3533	4.51	0.45
31	EA3564	3.10	0.31
32	EA3580	3.84	0.38
33	EA3574	4.17	0.42
34	EA3560	3.69	0.37
35	EA3565	3.83	0.38
36	EA3525	4.02	0.40
37	EA3537	3.79	0.38
38	EA3557	3.01	0.30
39	EA3547	3.17	0.32
40	EA3529	4.45	0.45
41	EA3548	3.34	0.33
42	EA3546	3.75	0.38
43	EA3551	3.57	0.36
44	EA3550	3.45	0.35
45	EA3554	3.69	0.37
46	EA3558	3.21	0.32
47	EA3559	3.06	0.31
Mean and Std :		3.90	0.52

Table 4.6: Means and standard deviations of the integrated charge of the modules from 23 to 47 measured with the light of the laser directly impinging on the quartz tablet.
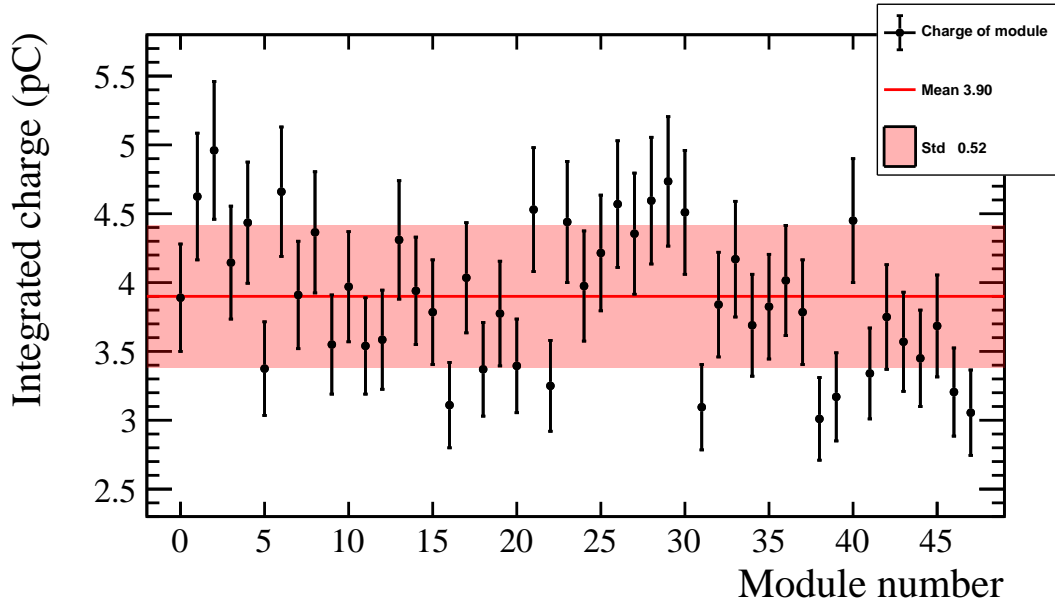
Figure 4.9: Values of the integrated charge of 48 PLUME modules measured with the light of the laser directly impinged on the quartz tablet. The red line is the mean of the measurements and the red band is the 1σ interval.

sensitivity. Blue sensitivity index is an essential parameter in scintillation counting because the NaI(Tl) scintillators frequently used in scintillation counting, produce blue light. The values of n_{cls} for each PMT is provided by Hamamatsu [52] and the σ_{bsi}^2 is around the 3%.

The mean and the standard deviation of the integrated charge of the 48 modules are presented in Tabs. 4.5 and 4.6.

A graphic representation of the measurements is shown in Fig. 4.9. The mean of the measurement is $\mu = 3.90$ pC and the standard deviation is $\sigma = 0.52$ pC. Almost all the signal charges are compatible with the mean, within a 1σ interval. Therefore, the modules have the same behavior when they are biased with a voltage producing the same charge amplification. This confirm that the results obtained during the characterization are right and that of the dark absorbing ring is well positioned in front of the quartz tablet.

Light transmitted in the optic fiber

In this measurement, all the modules were tested with their corresponding optic fiber. The instrumentation and the conditions of the light source were the same of the previous tests, but the module is positioned out of the dark box and the laser output was connected to the SMA connector at one end of the optical fiber. The other end was fixed to the
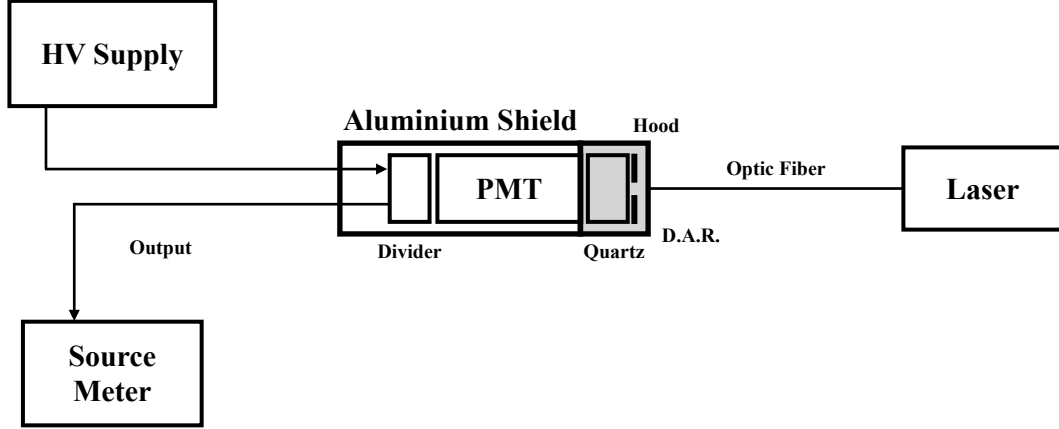
Figure 4.10: Scheme of the experimental setup used for the qualification test performed with laser light transmitted in the optic fiber. D.A.R is the dark absorbing ring fixed to quartz tablet.

hood which covers the aluminium cylindrical shield containing the PMT. Therefore the light emitted by the laser was transmitted inside the fiber before reaching the quartz tablet. In Fig. 4.10, a schematic view of the experimental setup is shown.

If the end of the optical fiber is not completely perpendicular to the window of the PMT, a small amount of the transmitted light can be lost. Therefore the connection between the optic fiber and the window of the PMT introduces a new component in the formula for the standard deviation, which becomes

$$\sigma_{measure} = \sqrt{\sigma_{gain}^2 + \sigma_{laser}^2 + \sigma_{heating}^2 + \sigma_{bsi}^2 + \sigma_{coulping}^2}. \tag{4.7}$$

In order to estimate the $\sigma_{coupling}$ contribution, the variation of signal depending on the rotation of the fiber connection (see Fig: 4.5) was measured for 9 different modules. The $\sigma_{coulping}$ turns out to be equal to 0.83%, that is negligible compared to the biggest contributions.

The mean and the standard deviation of the integrated charge of the 48 modules are presented in Tab.4.7 and Tab.4.8.

The mean of the measurements is $\mu = 3.18$ pC and the standard deviation is $\sigma = 0.49$ pC. As for the previous test, the signal integrated by the modules is the same within a 1σ interval. However, the mean of the integrated charge decreases by 18.5% with respect to the direct lighting of the PMT. The two tests were performed with the same conditions so the signal decrease was due to the attenuation of the light during the transmission in the optical fiber.

Module Number	PMT Serial Number	Mean Integrated Charge (pC)	Std Dev (pC)
00	EA3573	2.97	0.30
01	EA3556	3.02	0.30
02	EA3540	4.25	0.42
03	EA3541	3.28	0.33
04	EA3542	3.44	0.34
05	EA3543	2.67	0.27
06	EA3534	3.74	0.37
07	EA3549	3.19	0.32
08	EA3535	3.52	0.35
09	EA3544	2.83	0.28
10	EA3539	3.35	0.33
11	EA3553	3.06	0.31
12	EA3572	3.04	0.30
13	EA3568	3.48	0.35
14	EA3570	2.93	0.29
15	EA3569	2.95	0.29
16	EA3562	2.47	0.25
17	EA3561	3.37	0.34
18	EA3567	2.35	0.23
19	EA3563	2.80	0.28
20	EA3552	2.87	0.29
21	EA3538	3.80	0.38
22	EA3566	2.82	0.28
23	EA3527	3.95	0.40

Table 4.7: Mean and standard deviation of the integrated charge of the modules from 00 to 23 measured with the light of the laser directly impinging on the quartz tablet.

Module Number	PMT Serial Number	Mean Integrated Charge (pC)	Std Dev (pC)
24	EA3545	3.07	0.31
25	EA3526	3.74	0.37
26	EA3532	3.75	0.38
27	EA3536	3.65	0.36
28	EA3524	3.85	0.38
29	EA3528	4.08	0.41
30	EA3533	3.70	0.37
31	EA3564	2.86	0.29
32	EA3580	3.18	0.32
33	EA3574	3.72	0.37
34	EA3560	2.97	0.30
35	EA3565	2.89	0.29
36	EA3525	3.4	0.34
37	EA3537	3.35	0.34
38	EA3557	2.82	0.28
39	EA3547	2.54	0.25
40	EA3529	3.86	0.39
41	EA3548	2.39	0.24
42	EA3546	3.11	0.31
43	EA3551	3.00	0.30
44	EA3550	2.85	0.29
45	EA3554	3.08	0.31
46	EA3558	2.40	0.24
47	EA3559	2.18	0.22
Mean and Std :		3.18	0.49

Table 4.8: Means and standard deviations of the integrated charge of the modules from 24 to 47 measured with the light of the laser directly impinging on the quartz tablet.
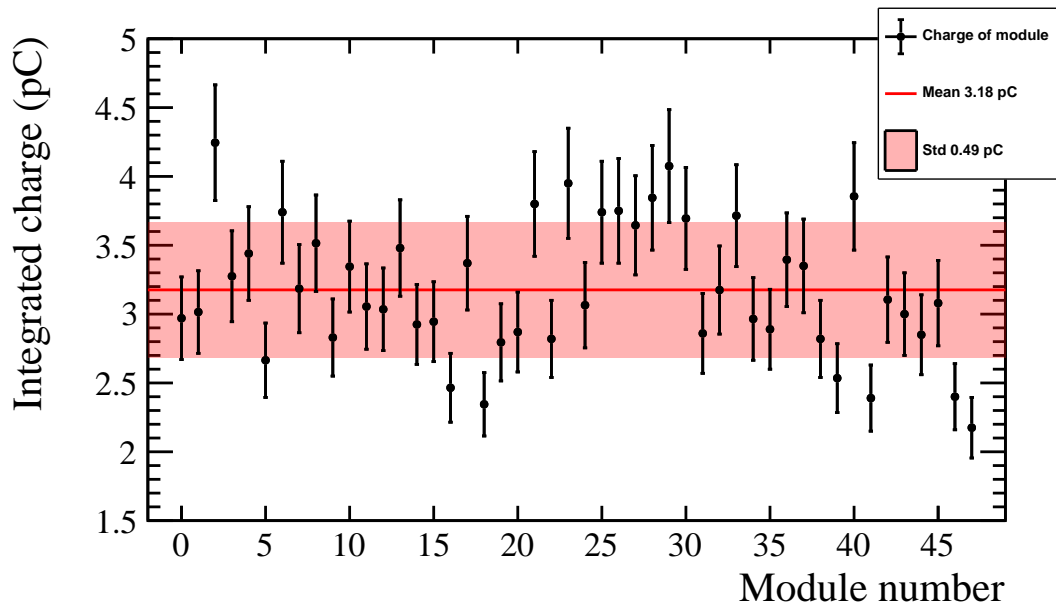
Figure 4.11: Values of the integrated charge of 48 PLUME modules measured with the light of the laser transmitted inside the optic fiber before impinging on the quartz tablet. The red line is the mean of the measurements and the red band is the 1σ interval.

4.2.2 Qualification test in the PLUME box

The 48 modules have been installed in the aluminium PLUME box to form the two levels hodoscope, Fig. 1.6. The signal and bias cables, and the optic fiber for the monitoring system were connected to the patch panel located below the detector. The detector box was divided into A and C side parts, containing respectively 14 and 34 modules. A second qualification test was performed in order to check all the connections done during the cabling and the installation.

The experimental setup is shown in Fig. 4.12. The source of light used in these tests was a 470 nm LED powered by a 5V amplitude pulse wave with a 6 ns width and a frequency of 10 kHz generated by a wave generator. The led was directly connected to the optical fiber of each module. Trigger signals are also sent to the instrument from the same wave generator in order to synchronize the measurement with the LED flash. A 100 mV amplitude pulse wave with 100 ns width and same frequency than the LED one is produced by the second channel of the wave generator. The trigger was connected to channel 1 of a 8 channels 12bits 3.2G S/s acquisition rate WaveCatcher [53], while the electric signal of the tested PMT was acquired on channel 0. The signal was integrated over time in order to get the integrated charge. Ten thousand events were acquired for each module. The mean and the RMS of the histogram of the integrated charge were directly computed by the acquisition system. The results of the measurements are
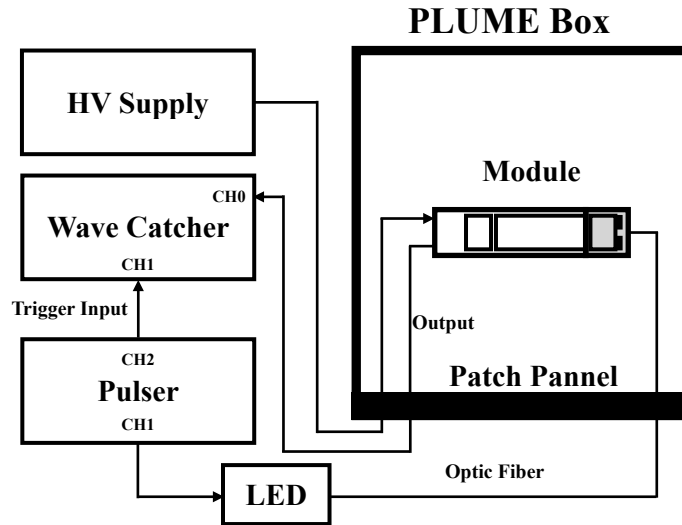
Figure 4.12: Scheme of the experimental setup used for the qualification test performed in the PLUME box.

reported in the Tabs. 4.9 and 4.10.

The mean of the integrated charge is 5.09 pC and the standard deviation is 0.81 pC. Fig 4.13 shows the measurements reported in Tabs.4.9 and 4.10. All the value are compatibile within 1σ.

The values measured are reported in Fig. 4.13. The graphical representation points out the compatibility of the measurements within the 1σ interval for the modules.

4.2.3 Comparison of the measurements

The response of the modules in all the tests confirms the results obtained during the characterization within the experimental errors. All the modules operated correctly before and after the positioning in the PLUME hodoscope. From the comparison between the two tests performed in the bench, the attenuation of the light due to the transition in the optical fiber of the monitoring system is estimated to be around the 18.5%.

In order to check the relative stability of the PMTs in time, the results of the three test were compared. Because of the different sources of light and configuration used in the tests, it was not possible to compare the absolute values of the signals. Therefore, the response stability of each module was checked by measuring the normalized ratio of the three tests. The results of the three ratios are shown in Fig 4.14, where test1, test2 and test3 are respectively the qualification tests in the bench, with the direct impinging light and with the light transmitted in the optical fiber, and the qualification test performed in the PLUME box. All the three ratios are distributed around 1, with standard deviations

Module Number	PMT Serial Number	Mean Integrated Charge (pC)	Std Dev (pC)
00	EA3573	4.47	0.40
01	EA3556	4.55	0.40
02	EA3540	5.85	0.50
03	EA3541	5.37	0.44
04	EA3542	4.47	0.42
05	EA3543	4.33	0.35
06	EA3534	6.16	0.50
07	EA3549	5.22	0.41
08	EA3535	6.21	0.47
09	EA3544	4.56	0.38
10	EA3539	5.58	0.44
11	EA3553	4.93	0.42
12	EA3572	4.93	0.40
13	EA3568	5.16	0.41
14	EA3570	4.60	0.40
15	EA3569	5.09	0.41
16	EA3562	3.85	0.35
17	EA3561	5.40	0.43
18	EA3567	3.92	0.36
19	EA3563	4.43	0.37
20	EA3552	4.67	0.39
21	EA3538	6.34	0.49
22	EA3566	4.24	0.35
23	EA3527	5.94	0.48

Table 4.9: Means and standard deviations of the integrated charge of the modules from 00 to 23 measured with the light of the laser directly impinging on the quartz tablet.

Module Number	PMT Serial Number	Mean Integrated Charge (pC)	Std Dev (pC)
24	EA3545	5.04	0.42
25	EA3526	6.02	0.48
26	EA3532	5.70	0.49
27	EA3536	5.81	0.49
28	EA3524	6.63	0.51
29	EA3528	6.82	0.53
30	EA3533	6.22	0.49
31	EA3564	4.71	0.90
32	EA3580	5.22	0.44
33	EA3574	6.01	0.49
34	EA3560	4.63	0.40
35	EA3565	4.49	0.41
36	EA3525	5.70	0.46
37	EA3537	4.84	0.47
38	EA3557	4.48	0.36
39	EA3547	4.17	0.37
40	EA3529	6.47	0.49
41	EA3548	4.35	0.37
42	EA3546	4.89	0.42
43	EA3551	4.89	0.38
44	EA3550	4.38	0.37
45	EA3554	5.04	0.42
46	EA3558	3.83	0.34
47	EA3559	3.51	0.33
Mean and Std :		5.09	0.81

Table 4.10: Means and standard deviations of the integrated charge of the modules from 24 to 47 measured with the light of the laser directly impinging on the quartz tablet.
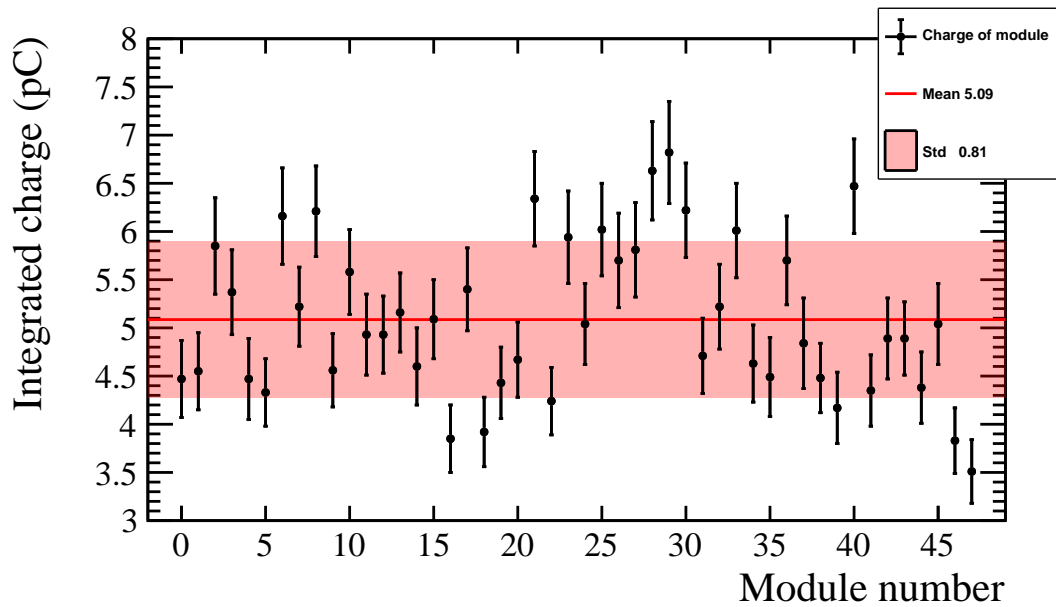
Figure 4.13: Values of the integrated charge of 48 PLUME modules measured in the PLUME box, with a LED. The red line is the mean of the measurements and the red band is the 1σ interval.

between 0.06 and 0.085. All the modules except the second and the fifth have a signal variation smaller then 10%. Therefore, the signal response of PLUME is stable within 10% and compatible with the experimental errors. Once PLUME will be in operation in the LHCb site, the modules will be monitored and calibrated continuously in order to have the best and most stable measure of the luminosity.

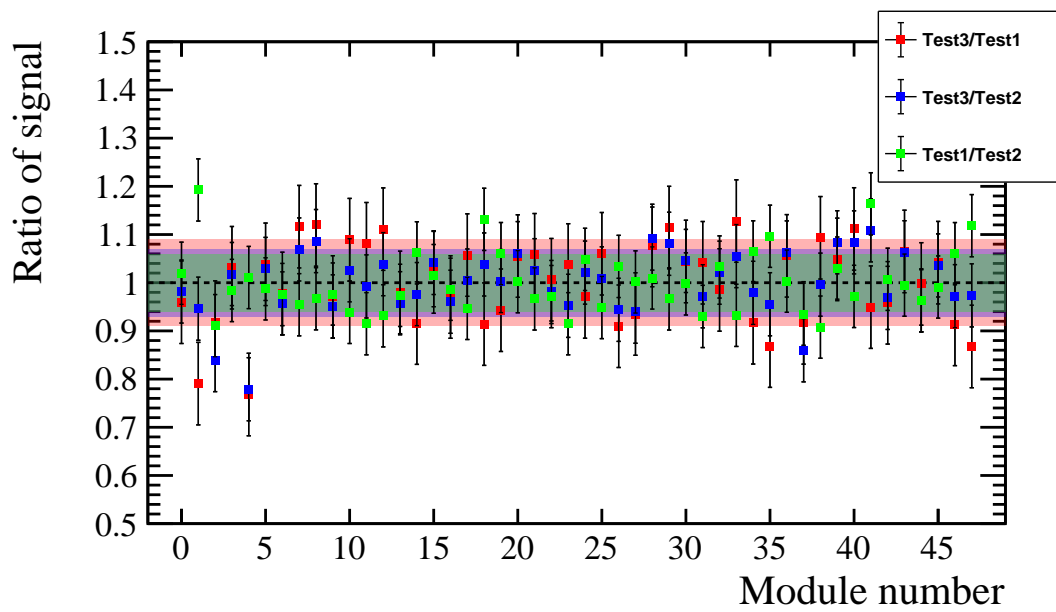Figure 4.14: Normalized ratio of the module signal measured in the three qualification tests: the red points are the ratio test3/test1; the blue points are the ratio test3/test2; the green points are the ratio test1/test2. The mean value of the three ratios is 1. The three coloured bands are the 1σ intervals.

Conclusions

The new luminometer PLUME, has been installed at LHCb in December 2021. During the whole three years of the Run 3, it will provide the measurements of the instantaneous luminosity at LHCb.

The 48 R760 HAMAMATSU PMTs composing the PLUME hodoscope have been characterized and tested by the LHCb groups of INFN of Bologna and CNRS of Orsay. For the characterization of each PMT, the gain, the transit time drift, the linearity and the dark current have been measured and studied. The data and results reported in this thesis for the characterization, regard the 29 PMTs characterized in Bologna. The mean value of the absolute gains at the maximum supply voltage applicable (1250 V) is found to be $(1.493 \pm 0.003) \times 10^7$. The values of the supply voltage at which the gains of the PMTs are equal to 1.5×10^5 are also measured. These values are crucial for the counting of the number of interactions per bunch-crossing μ, determined with the logZero method at the start of 2022 data taking.

The variation of the transit time depending on the supply voltage is quantified by looking at the transit time drift. The largest values of the t_{ttd}, between the minimum and maximum supply voltage, does not exceed the 6 ns. Hence, the PMTs are able to operate in a large range of voltage without losing more than 11% of precision, respect to the average values of t_{tt}.

The linearity of the output signal was tested for two values of the supply voltage. For voltages at which the gain is 1.5×10^5, the measured integrated charge can suffer a reduction of $10 - 40\%$ respect to its expected value. Instead, for a voltage 400 V higher than the previous one, the measured integrated charge is reduced by up to 50% of its expected value. However, PLUME is not expected to work at this regime.

The dark current of all the PMTs is lower than 10 nA even at the highest value of supply voltage supported by PMT and can be considered negligible compared to the signal current.

The new component of the elementary detection module, the dark absorbin ring, has been mounted on all the quartz radiators. The signal decrease after the application of the ring was tested for six configurations of two PMTs and three optic fibers. It results to be between 4% and 9%, acceptable for the running condition.

The qualification tests of the 48 modules of PLUME (a module includes the PMT,

the divider circuit, the quartz tablet, the dark absorbing ring and the optic fiber), were performed at IJCLab of Orsay. The modules were tested in the dark box of the laboratory with two configurations and in the PLUME structure, after the installation. The two tests in the dark box were performed with the light impinging directly the surface of the quartz in front of the PMT and with the light transmitted in the optic fiber, to simulate signal produced by the calibration system of PLUME. The modules were tested under the same light and gain condition and the signal integrated charges were computed. All the modules operated correctly before and after the positioning in the PLUME hodoscope. The signals of the 48 modules are compatible within 1σ around the value of the mean of the measures. The attenuation of the light due to the transition in the optical fiber of the monitoring system is estimated to be around the 18.5%.

Then, the stability of each module response is checked by computing the normalized ratios of its three signals. All the modules have a signal variation smaller then 10%, compatible with the expected performance of the detector. The calibration and monitoring of the modules will be constantly performed by the calibration system of PLUME.

Bibliography

[1] G. Papotti *et al.*, *LHC operation at 6.5 TeV: Status and Beam Physics Issues*, NAPAC2016, Chicago, IL, USA, 2016.

[2] B. Salvachua *et al.*, *LHC operational scenarios during 2017 run*, IPAC2018, Vancouver, Canada, 2018.

[3] S. Fartoukh *et.al*, *LHC Configuration and Operational Scenario for Run 3*, CERN-ACC-2021-0007, CERN, Geneva, 2021.

[4] LHCb collaboration,*LHCb PLUME: Probe for LUminosity MEasurement*, CERN-LHCC-2021-002. LHCb-TDR-022. May. 4, 2021.

[5] G. Avoni *et al.*, *The new LUCID-2 detector for luminosity measurement and monitoring in ATLAS*, JINST 13 (2018) P07017.

[6] V. Balagura *et al.*, *Probe for LUminosity MEasurement in LHCb*, LHCb-PUB-2020-008. CERN-LHCb-PUB-2020-008, CERN, Geneva, 2020.

[7] R. Aaij *et al.*, *LHCb Detector Performance*. Int. J. Mod. Phys. A30.07 (2015), p. 1530022. arXiv: 1412.6352 [hep-ex].

[8] R. Aaij *et al.*, *Precision luminosity measurements at LHCb*, JINST 9.12 (2014), P12005. arXiv: 1410.0149 [hep-ex].

[9] I. Bediaga *et al.*,*Framework TDR for the LHCb Upgrade: Technical Design Report.*, Tech. rep. CERN-LHCC-2012-007. LHCb-TDR-12. Apr. 2012. url: https://cds.cern.ch/record/1443882.

[10] T. Szumlak *et al.*, *LHCb Vertex Locator: Performance and radiation damage in LHC Run 1 and preparation for Run 2*,Nucl. Instrum. Methods Phys. Res., A 824 (2016) 59-61, CERN, Geneva, 2015.

[11] HAMAMATSU photonics K.K.,*Photomultiplier tubes R760*, 2016, https://www.hamamatsu.com

[12] V. Cicero, *Neutron radiation resistance of photomultipliers for the LU-CID detector in the ATLAS experiment at LHC*, PhD thesis, 2015, https://amslaurea.unibo.it/9410/1/cicero valentina tesi.pdf.

[13] J. Allison *et al.*, *Geant4 Developments and Applications*, IEEE Trans. Nucl. Sci., vol. 53, no. 1, pp. 270-278, 2006.

[14] Momentive Performance Materials Japan LLC, *Dimethyl Silicone Fluids As Antifoam Agents TSF451 Series*, 2006.

[15] V. Puill and others, *PLUME ECR*, EDMS 2432538, 2021.

[16] Y. S. Amhis *et al.*, *The Front-End board of the upgraded LHCb Calorimeter*, LHCb-INT-2019-004. CERN-LHCb-INT-2019-004, CERN, Geneva, 2019.

[17] Y. S. Amhis *et al.*, *3CU Calorimeter Control Card Unit*, LHCb-INT-2019-003. CERN- LHCb-INT-2019-003, CERN, Geneva, 2019.

[18] J. P. Cachemiche *et al.*, *The PCIe-based readout system for the LHCb experiment*, JINST 11 (2016) P02013.

[19] F. Alessio, P. Durante, and G. Vouters, *The readout supervisor firmware for controlling the upgraded LHCb detector and readout system*, arXiv:1806.08626.

[20] S. Cap, S. Tjampens and G. Vouters, *LHCb upgrade calorimeter TELL40 data processing*, EDMS 1889215, 2020.

[21] J. Barbosa *et al.*, *Front-end electronics control and monitoring for the LHCb upgrade*, EPJ Web of Conferences 214 (2019) 01002.

[22] I. Guz *et al.*, *Upgrade of the monitoring system of LHCb ECAL*, LHCb-PUB-2016-018. CERN-LHCb-PUB-2016-018, CERN, Geneva, 2016.

[23] M. I. Aizatskyi *et al.*, *State and Prospects of the LINAC of Nuclear-Physics Complex with Energy of Electrons up to 100 MeV*, Problems of Atomic Science and Technology, Series: Nuclear Physics Investigations 91 (2014) 60.

[24] HAMAMATSU photonics K.K.,*Si PIN photodiodes, S1223 series*,2014, https://www.hamamatsu.com.

[25] A. Konoplyannikov, *Electronics of LHCb calorimeter monitoring system*, in Proceedings of the Topical Workshop on Electronics for Particle Physics (TWEPP-08), Naxos, Greece, 15-19 Sep 2008, 397–401, 2008.

[26] R. Martin Lesma *et al.*, *The Versatile Link Demo Board (VLDB)*, JINST 12 (2017) C02020.

[27] S. White. *Determination of the absolute luminosity at the LHC* High Energy Physics - Experiment [hep-ex]. Université Paris Sud - Paris XI, 2010.

[28] M. Schmelling, *Luminosity calibration for the leading bunch nobias-triggered data from the 2015 early measurement runs*, LHCb-INT-2017-015. CERN-LHCb-INT-2017-015, CERN, Geneva, 2017.

[29] S. van der Meer, *Calibration of the Effective Beam Height in the ISR*, CERN-ISR-PO-68-31, 1968, https://cds.cern.ch/record/296752

[30] W.R. Leo, *Techniques for Nuclear and Pharticle Physics Experiments*, Springer-Verlag, Germany, 1987

[31] J.H. Hubbell *et al.*, *Tables of X-Ray Mass Attenuation Coefficients and Mass Energy-Absorption Coefficients*. National Institute of Standards and Technology (NIST), Retrieved 2 Nov 2007.

[32] A. Einstein, *Über einen dir Erzeugung und Versandlung des Lichtes betreffenden heuristischen Gesichtspunkt*, Annalen der Physik, 17, 132-148, Translated into English in A. Einstein 1905.

[33] P. Marmier & E. Sheldon, *Physics of Nuclei and Particles*, Vol. 1, Academic Press, New York, 1969.

[34] HAMAMATSU photonics K.K.,*Photomultipliers tubes, Basic and Applications*, Fourth edition, 2017

[35] R.L. Bell, *Negative Electron Affinity Devices*, Calredon Press. Oxford, 1973.

[36] G.A. Morton *et al.*: IEEE Trans. Nucl. Sci. NS-14 No. 1, 443, 1967.

[37] HAMAMATSU photonics K.K., *Final test sheet EA3510, EA3513*, October 12,2020, https://www.hamamatsu.com

[38] Alphalas*Picosecond Diode Lasers with Driver: PICOPOWER$^{TM}-LD$ Series*, 210929, www.alphalas.com.

[39] Keithley, *Picoammeter 6485*, www.tek.com, 2007

[40] Keithley, *DAQ6510 Data Acquisition and Logging, Multimeter System, Datasheet*, www.tek.com, 2007

[41] Paul Scherrer Institut (PSI), *DRS4 Evaluation Board*, www.psi.ch.

[42] Costruzioni Apparecchiature Elettroniche Nucleari spa. *SY127 40 Channel High Voltage System, Power Supply*, www.caen.it.

[43] S. Tokàr *et al.*, *Single Photoelectron Spectra Analysis for the Metal Dynode Photo-multiplier*, tilecal-99-005, CERN, Geneva, 1999.

[44] M. Takahashi, *A technique for estimating the absolute gain of a photomultiplier tube*, ScienceDirect, Nuclear Inst. and Methods in Physics Research, A 894 2018.

[45] Thorlab, *Compact Photodiode Power Head with Silicon Detector S120C*, 18356-S01, Rev C, www.thorlabs.com, 2016.

[46] UQG Optic, *SPECTROSIL 2000 Data sheet*, Cambridge, England, www.uqgoptics.com.

[47] V. Yeroshenko, *PLUME Simulation*, Kyiv University, 2021

[48] Shin-Etsu Chemical Co., *RTV Silicone Rubber*, shinetsusilicone-global.com

[49] Advanced Laser Diode System A.L.S. Gmbh, *PicosecondInjection Laser (PiLas), Owner's Manual*, Rev. 3.0, 2004.

[50] Keithley, *System SourceMeter Multi-Channel I-V Test Solutions*, www.tek.com, 2007.

[51] HAMAMATSU photonics K.K., *Metal Package Photomultiplier tube R9880U Series*, www.hamamatsu.com

[52] HAMAMATSU photonics K.K., *Final test sheet EA35XX*, 2020, https://www.hamamatsu.com

[53] D. Breton *et al.*, *The WaveCatcher family of SCA-based 12-bit 3.2-GS/s fast dig-itizers*, Laboratoire de L'accélérateur Linéaire from CNRS/IN2P3, Orsay, France, 2014.